

# Important Notice

This copy may be used only for the purposes of research and private study, and any use of the copy for a purpose other than research or private study may require the authorization of the copyright owner of the work in question. Responsibility regarding questions of copyright that may arise in the use of this copy is assumed by the recipient.

THE UNIVERSITY OF CALGARY

**AN INTERPRETIVE STUDY OF MULTICOMPONENT  
SEISMIC DATA FROM THE CARROT CREEK AREA  
OF WEST-CENTRAL ALBERTA**

by

Brad Nazar

A THESIS

SUBMITTED TO THE FACULTY OF GRADUATE STUDIES  
IN PARTIAL FULFILLMENT OF THE REQUIREMENTS FOR THE  
DEGREE OF MASTER OF SCIENCE

DEPARTMENT OF GEOLOGY AND GEOPHYSICS

CALGARY, ALBERTA

NOVEMBER, 1991

© Brad Nazar 1991

THE UNIVERSITY OF CALGARY

FACULTY OF GRADUATE STUDIES

The undersigned certify that they have read, and recommend to the Faculty of Graduate Studies for acceptance, a thesis entitled "AN INTERPRETIVE STUDY OF MULTICOMPONENT SEISMIC DATA FROM THE CARROT CREEK AREA OF WEST-CENTRAL ALBERTA" submitted by Bradley Dennis Nazar in partial fulfillment of the requirements for the degree of Master of Science.



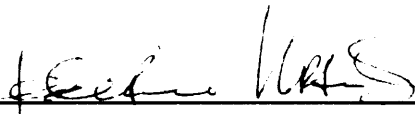
---

Supervisor, Dr. D. C. Lawton,  
Department of Geology and Geophysics



---

Dr. R. J. Brown,  
Department of Geology and Geophysics



---

Dr. F. F. Krause,  
Department of Geology and Geophysics



---

Dr. H. J. Laue  
Department of Physics and Astronomy

Date: November 22, 1991.

## ABSTRACT

In 1987, two multicomponent seismic lines were acquired in the Carrot Creek area of west-central Alberta. Analyses of the final processed seismic sections (P-P and P-SV) showed that the interpretation of P-SV (radial-component) data can assist greatly in delineating geologic units, particularly the Cardium conglomerates of the Carrot Creek area. At the location of the conglomerate deposits, for instance, strong amplitude anomalies can be observed with the P-SV data, whereas only subtle amplitude variations can be observed with the P-P (vertical-component) data at the same locations.

The difference in Cardium responses of the P-P and P-SV stacks was found to be a result of their respective amplitude-versus-offset (AVO) responses. Forward modeling showed that, for the Cardium event, a polarity reversal occurs with offset with the P-P, but not the P-SV, data. It is this polarity reversal which causes the poor amplitude response of the P-P data at the location of the Cardium conglomerate. This arises from the destructive interference of the near- and far-offsets of the P-P data upon stacking, whereas the radial-component offsets add constructively, producing a higher amplitude P-SV Cardium event. The P-P and P-SV data were also found to be most sensitive to variation in conglomerate thickness over the 0-1000 m and 500-2000 m offset ranges respectively. These results indicate that better imaging of the Cardium conglomerate could therefore be achieved by either limiting the offset range during acquisition or by generating offset-range stacks. The generation of a P-P 0-1000 m offset-range stack, in fact, showed a significant increase in the relative amplitude of the Cardium event at the location of the conglomerate deposits. A conventional seismic data set (far-offsets of 1200 m), also acquired in the Carrot Creek area but in a different location than the multicomponent data, showed no indication of thick conglomerate deposits.

It was also found that Poisson's ratio for specific seismic intervals could be derived from the P-P and P-SV traveltimes. Since the Cardium conglomerate possesses a low

Poisson's ratio (0.18-0.22) relative to the surrounding shales (0.31), this interval analysis was capable of identifying variations in conglomerate thickness by the presence of lows in the calculated Poisson's ratio. Two such lows were determined using the multicomponent data, which in turn correlate well with the location of known conglomerate deposits.

## **Acknowledgements**

This thesis would not have been possible without the assistance of several individuals and companies. I am especially grateful to Dr. Don Lawton (thesis supervisor) for the significant amount of time spent examining and discussing my results. His constructive criticism concerning scientific writing were very useful and will not be forgotten. I would also like to thank Dr. Ed Krebs (The University of Calgary) for generating the phase and amplitude spectra used in this thesis. Discussions with my fellow graduate students, especially Mr. Mark Harrison, regarding seismic data processing also benefited me greatly. Thanks also go to Tina Howell for helping solve the mystery of the computer systems and software.

I would finally like to thank Boyd Exploration Ltd. and Suncor Oil and Gas for their donations of the multicomponent and conventional data sets, and the sponsors of the CREWES Project for their support.

## Table of Contents

Approval Page .....	ii
Abstract .....	iii
Acknowledgements .....	v
Table of Contents .....	vi
List of Tables .....	ix
List of Figures .....	x
<b>Chapter 1 - INTRODUCTION</b>	
1.1 Background .....	1
1.2 Acquisition of S-wave Data .....	3
1.3 P-SV versus SH-SH Data Acquisition.....	5
1.4 Amplitude-versus-offset .....	6
1.5 Thesis Objectives .....	7
1.6 Structure of Thesis .....	7
1.7 Seismic Data Sets Used in Thesis .....	8
1.7.1 Conventional data set .....	8
1.7.2 Multicomponent data set .....	8
1.8 Hardware and Software Used .....	8
<b>Chapter 2 - GEOLOGY</b>	
2.1 Study Area .....	12
2.2 Stratigraphy .....	13
<b>Chapter 3 - DATA PROCESSING (Conventional)</b>	
3.1 Introduction .....	21
3.2 Preprocessing .....	21
3.2.1 Demultiplexing .....	21

3.2.2	Geometry and Editing .....	21
3.2.3	Correction for Spherical Divergence .....	21
3.3	Spiking Deconvolution .....	24
3.4	CMP Sort .....	24
3.5	Elevation and Refraction Statics .....	25
3.6	Velocity Analysis and NMO Correction .....	26
3.7	Surface Consistent Residual Statics .....	29
3.8	Front-end Mute .....	30
3.9	Trim Statics .....	31
3.10	CMP Stack .....	31
3.11	Bandpass Filtering .....	31
3.12	Finite-difference Migration .....	32
3.13	<i>f-k</i> Filtering .....	38
 <b>Chapter 4 - DATA PROCESSING (Multicomponent)</b>		
4.1	Introduction .....	39
4.2	Reverse Polarity of Trailing Spread .....	41
4.3	P-SV Weathering Statics .....	44
4.4	NMO Correction .....	45
4.5	Common Conversion-point Sort .....	50
4.5.1	Asymptotic Sort and Stack .....	50
4.5.2	Depth-variant (CCP) Mapping .....	53
4.6	Discussion .....	58
 <b>Chapter 5 - INTERPRETATION</b>		
5.1	Introduction .....	60
5.2	Geologic Model .....	60

5.3 AVO Modeling .....	72
5.3.1 Tuning Effect .....	76
5.3.2 Thickness Dependency .....	76
5.3.3 Poisson's Ratio Dependency .....	79
5.4 AVO Analysis of Carrot Creek Data .....	83
5.5 Lateral Changes in $V_p/V_s$ .....	86
5.6 Discussion .....	87
5.6.1 Event Amplitude .....	87
5.6.2 Offset-range Stacking .....	89
5.6.3 Limiting the Far-offset .....	96
Chapter 6 - CONCLUSIONS .....	97
References .....	99
Appendix A .....	104
Appendix B .....	105

## List of Tables

Table 1.1. Acquisition and recording parameters for the conventional seismic data set ..	10
Table 1.2. Acquisition and recording parameters for the multicomponent seismic data set. ....	10
Table 5.1. Carrot Creek model parameters. ....	61
Table 5.2. $V_p/V_s$ for specific seismic intervals based upon P-P and P-SV interval times. ....	72

## List of Figures

FIG. 1.1. Mode-conversion from an incident P-wave. ....	3
FIG. 1.2. Schematic diagram illustrating P-wave and SV-wave particle motion. ....	4
FIG. 1.3. Carrot Creek seismic data. ....	9
FIG. 2.1. Carrot Creek location map. ....	12
FIG. 2.2. Stratigraphic correlation chart for the Alberta Central Plains. ....	14
FIG. 2.3. Characteristic well log response of the Cardium Formation taken from well 10-35-52-13W5. ....	15
FIG. 2.4. Isopach resistivity map. ....	17
FIG. 2.5. Cross-section A-A' of the Wapiabi - Blackstone interval. ....	18
FIG. 2.6. Orientation of the cross-section (A-A') and the two multicomponent seismic lines. ....	19
FIG. 2.7. Structure map of the top of conglomerate interval (i.e. top of the Pembina River member), relative to sea-level. ....	20
FIG. 3.1. Seismic data processing flow (conventional data). ....	22
FIG. 3.2. Shot records from line CR851 showing varying data quality. ....	23
FIG. 3.3. Geometry of a typical CMP gather. ....	25
FIG. 3.4. Refractor model for line CR851. ....	27
FIG. 3.5. Velocity spectrum for CMP 222 of line CR851. ....	28
FIG. 3.6. Frequency panels of CMP gather 200 from line CR851. ....	33
FIG. 3.7. Stack of line CR852 with final statics and 10-70 Hz bandpass filter applied. ..	34
FIG. 3.8. Final migrated stack of line CR851. ....	35
FIG. 3.9. Final migrated stack of line CR852. ....	36
FIG 3.10. Final migrated stack of line CR853. ....	37

FIG. 4.1. Data recorded in the vertical, radial and transverse direction from shot 27 (source at station 138) of line CCSW02.....	40
FIG. 4.2. Vertical-component processing flow. ....	42
FIG. 4.3. Radial-component processing flow. ....	43
FIG. 4.4. Particle motion and receiver orientation for a P-SV survey. ....	44
FIG. 4.5. Common-source and common-receiver stacks of the P-SV (radial component) data of line CCSW02.....	46
FIG. 4.6. Synthetic P-SV common-offset gathers. ....	48
FIG. 4.7. Vertical and radial common-offset gathers from station 320 of line CCSW02.	49
FIG. 4.8. Velocity spectra of P-P and P-SV data of station 320 of line CCSW02. ....	51
FIG. 4.9. Raypath geometry for P-SV data. ....	52
FIG. 4.10. Final vertical-component migrated section from line CCSW01. ....	54
FIG. 4.11. Final radial-component migrated section from line CCSW01. ....	55
FIG. 4.12. Final vertical-component migrated section from line CCSW02. ....	56
FIG. 4.13. Final radial-component migrated section from line CCSW02. ....	57
FIG. 5.1. Geometry of the Carrot Creek geologic model . ....	61
FIG. 5.2. Identification of events on the vertical component of line CCSW01. ....	62
FIG. 5.3. Final migrated and interpreted stacks of line CR851. ....	63
FIG. 5.4. Final migrated and interpreted stacks of line CR852. ....	64
FIG. 5.5 Final migrated and interpreted stacks of line CR853. ....	65
FIG. 5.6. Final migrated and interpreted stacks of the vertical-component of line CCSW01.....	66
FIG. 5.7. Final migrated and interpreted stacks of the vertical component of line CCSW02.....	67
FIG. 5.8. Correlation between the vertical and radial components of line CCSW01. ....	68

FIG. 5.9. Final migrated and interpreted stacks of the radial component of line CCSW01..	70
FIG. 5.10. Final migrated and interpreted stacks of the radial component of line CCSW02..	71
FIG. 5.11. Amplitude and phase for the P-P and P-SV events from the top of the conglomerate. ....	74
FIG. 5.12. Amplitude and phase for the P-P and P-SV events from the bottom of the conglomerate. ....	75
FIG. 5.13. Cardium AVO response for P-P and P-SV case of a 15 m thick conglomerate with a Poisson's ratio of 0.22. ....	77
FIG. 5.14. The effect of variation in conglomerate thickness on the P-P seismic response and the amplitude of the Cardium peak. ....	78
FIG. 5.15. The effect of variation in conglomerate thickness on the P-SV seismic response and the amplitude of the Cardium trough. ....	80
FIG. 5.16. The effect of variation in the conglomerate's Poisson's ratio on the P-P seismic response and the amplitude of the Cardium peak. ....	81
FIG. 5.17. The effect of variation in the conglomerate's Poisson's ratio on the P-SV seismic response and the amplitude of the Cardium trough. ....	82
FIG. 5.18. Offset-stacks of the P-P (vertical component) data of line CCSW02 and the amplitudes of the corresponding Cardium peaks. ....	84
FIG. 5.19. Offset-stacks of the P-SV (radial component) data of line CCSW02 and the amplitudes of the corresponding Cardium troughs. ....	85
FIG. 5.20. Interval Poisson's ratios calculated from line CCSW01 using various isochrons. ....	88
FIG. 5.21. P-SV tuning of the Viking, Joli Fou and Mannville events.....	90
FIG. 5.22. Cardium event of the vertical and radial components of line CCSW01.....	91
FIG. 5.23. Comparison between the P-SV Cardium amplitude anomaly, the conglomerate interval isopach and the Poisson's ratio for the Lea Park - Blackstone interval of line	

CCSW01. ....	92
FIG. 5.24. Comparison of the Cardium event from a 0-1000 m P-P offset-range stack and the final radial-component stack of line CCSW01.....	94
FIG. 5.25. The Cardium event from a portion of lines CR851, CR852 and CR853.....	95

## Chapter 1- INTRODUCTION

### 1.1 Background

Seismic exploration techniques, and in particular reflection seismology, have long been used to aid in locating hydrocarbon deposits by mapping subsurface geologic structure and stratigraphic features. Seismic exploration consists of artificially generating body-waves [compressional (P)-waves and/or shear (S)-waves] at or near the ground surface and recording the wavefield reflected from acoustic impedance contrasts in the subsurface using geophones. The recorded data are then processed into a cross-sectional view of the Earth.

Although most seismic data in the past have been acquired and processed to enhance P-waves, there are several advantages in also acquiring S-waves. The most promising use of S-wave data is that, in conjunction with P-wave data, information concerning rock lithology can be obtained. Pickett (1963) and Tatham (1982), for example, showed that an association exists between the ratio of P- to S-wave velocities (i.e.  $V_p/V_s$ ) and various rock lithologies. Compressional- and shear-waves are in fact affected differently by the physical properties of rock. For instance, the P-wave velocity and therefore reflection amplitudes are affected by rock incompressibility, rigidity and bulk density (Domenico and Danbom, 1986). The velocity of S-waves, on the other hand, is affected only by rock rigidity and bulk density. These relationships are shown by the following equations:

$$V_p = \sqrt{\frac{\kappa + \frac{4}{3}\mu}{\rho}} \quad (1.1)$$

$$V_s = \sqrt{\frac{\mu}{\rho}} \quad (1.2)$$

where  $V_p$  is the P-wave velocity,  $V_s$  is the S-wave velocity,  $\kappa$  is the bulk modulus (incompressibility),  $\mu$  is the shear modulus (rigidity) and  $\rho$  is the bulk density.

Since rock incompressibility ( $\kappa$ ) varies with fluid type and rigidity ( $\mu$ ) is constant at zero, P-wave and not S-wave velocity will exhibit the greatest variation between similar

rocks containing different pore-fluids (i.e. water, oil, gas). This behavior was shown by Tatham and Stoffa (1976), Gregory (1976) and Domenico (1976), using laboratory data. They observed that  $V_p/V_s$  is lower for gas-saturated sands than for liquid-saturated sands. Because of this insensitivity of S-waves to pore-fluid type, it should be possible to verify P-wave reflection amplitude variations, due to pore-fluid change, by the absence of variation in amplitude of the corresponding S-wave reflection (Domenico and Danbom, 1986). This technique has been used successfully by Ensley (1984), Robertson and Pritchett (1985) and Frasier and Winterstein (1990) in identifying gas-saturated sands.

The acquisition of S-wave data in conjunction with P-wave data also allows for the determination of interval  $V_p/V_s$  and therefore values of Poisson's ratio. Poisson's ratio ( $\sigma$ ) can be calculated, using  $V_p/V_s$ , according to:

$$\sigma = \frac{\frac{1}{2} \left[ \frac{V_p}{V_s} \right]^2 - 1}{\left[ \frac{V_p}{V_s} \right]^2 - 1} \quad (1.3)$$

Baltenberger and Bay (1990) used such an analysis to determine the sand-shale ratio within fluvial-deltaic channel-fill and transgressive beach deposits. Pardus et al. (1990) also used  $V_p/V_s$ , determined from multicomponent seismic data, to distinguish between reservoir dolomites and non-reservoir limestones.

Crampin (1985) proposed that the acquisition of S-waves may also allow one to identify and characterize vertical fracture systems through the analysis of shear-wave splitting. This, in turn, could be used in estimating the orientation of cracks which would be important to production and reservoir engineering (Crampin, 1985).

Shear-wave data may also have a higher resolving power than P-wave data (Helbig, 1986). For instance, S-wave data containing the same frequencies as P-wave data would contain considerably shorter wavelengths, due to the lower velocities of the S-waves. This would therefore result in greater resolution for S-wave data. Shear-wave data, however,

rarely show any increase in resolution compared to P-wave data, due to greater absorption in the near-surface weathering layer (Helbig, 1986).

## 1.2 Acquisition of S-wave Data

Figure 1.1 shows that when a P-wave strikes an acoustic impedance contrast at a non-zero angle of incidence, both reflected and transmitted shear (S)-waves will be generated through mode-conversion. The P- and S-wave velocities and densities of the upper and lower media shown in Figure 1.1 are represented by  $\alpha_1, \beta_1, \rho_1$  and  $\alpha_2, \beta_2, \rho_2$  respectively. All angles of reflection and transmission for the P- and S-waves obey Snell's Law, as shown in Figure 1.1. Mode-converted S-waves are referred to as SV-waves due to their polarization in a vertical plane relative to an assumed flat, reflecting surface. Aki and Richards (1980) show that the amount of conversion that occurs is dependent upon the velocity, density and Poisson's ratio contrasts across the interface, as well as the angle of incidence ( $\theta$  or  $\lambda$ ) of the energy impinging on the reflector.

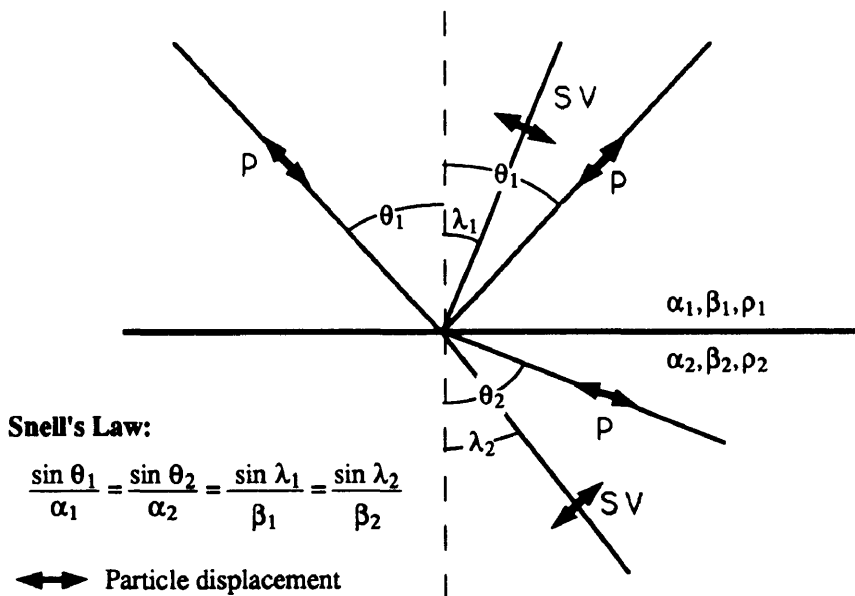


FIG. 1.1. Mode-conversion from an incident P-wave.

Since source-receiver offsets are generally smaller than the depth to a reflector, P- and S-waves will emerge at the surface as nearly vertical and in-line horizontal oscillations respectively, as shown in Figure 1.2. These orientations are also enhanced by the presence of a low-velocity weathering layer which causes the raypaths to refract towards the vertical.

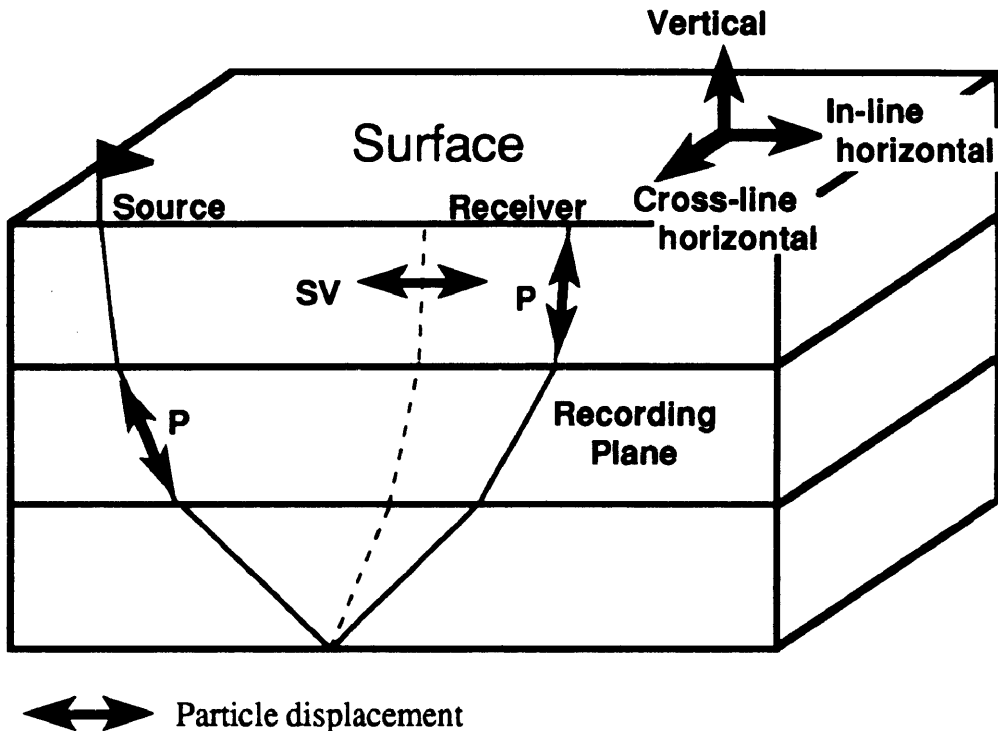


FIG. 1.2. Schematic diagram illustrating P-wave and SV-wave particle motion.

To record, both P and SV reflections, three-component geophones are used. These geophones record particle motion (i.e. particle velocity) along three orthogonal axes; one vertical and two horizontal. The two horizontal axes are orientated in the in-line (radial) and the cross-line (transverse) directions (Figure 1.2). With this orientation, the vertical and radial components record P-wave and SV-wave particle velocities respectively, along with source-generated surface waves (i.e. Rayleigh waves). For a flat-layered earth, the transverse component should record only SH-waves (i.e. S-waves with particle motion in the cross-line

direction) and Love waves (i.e. surface waves) that are generated by the source. Other coherent signal observed on the transverse component could be due to out-of-line effects (i.e. sideswipe) or velocity anisotropy.

### **1.3 P-SV versus SH-SH Data Acquisition**

Although the use of S-waves in seismic exploration is still in its infancy, many S-wave surveys have been acquired (e.g. Ensley, 1984; McCormack et al., 1984; Robertson and Pritchett, 1985; Frasier and Winterstein, 1990). Historically, multicomponent surveys have used, in addition to a conventional P-wave source (i.e. dynamite or vibrators), sources that generate SH-waves and sometimes SV-waves. The advantage of using an SH-wave source is that only one displacement component (i.e. cross-line) is present and therefore P- and SV-waves would not be generated through mode-conversion. The result would then be an S-wave dominated section.

One of the major disadvantages in acquiring a full multicomponent survey, however, is the cost due to the use of multiple sources. The recording of converted-wave data, on the other hand, can cut the acquisition costs in half through the use of only one source. Converted S-waves are also advantageous because the S-wave pathlength through the weathering layer is cut in half. This is important since this layer is often a strong attenuator for S-waves. It can also contribute very large, short wavelength S-wave statics to the data (McCormack and Tatham, 1986). The term "statics" refers to the bulk shifts applied to seismic traces to compensate for the effects of variation in surface elevation, weathering thickness and weathering velocity (Sheriff, 1991).

Even though, economically, the recording of converted-wave data is desirable, many unique problems arise in the processing of these data (Eaton and Stewart, 1989; Frasier and Winterstein, 1990). For instance, in addition to the large S-wave statics, several problems arise from the non-symmetrical P-SV raypath (Figure 1.1). These problems arise during

NMO correction and the sorting of the data. Chapter 4 describes these difficulties in more detail and describes the processing techniques used to remove them.

#### **1.4 Amplitude-versus-offset**

When dealing with a large range of incidence angles, as is usually the case with multicomponent data sets, it is important to look at the incidence-angle dependence of the reflected and converted-wave energy (i.e. P-P and P-SV reflection coefficients). This incidence-angle dependence was initially discussed by Muskat and Meres (1940) and then studied further by Koefoed (1955, 1962). Koefoed found that the change in P-wave reflection coefficient with angle of incidence is dependent upon the Poisson's ratio contrast across an elastic boundary. Koefoed (1955) proposed that by studying the variation of the reflection coefficient with angle of incidence (i.e. source-receiver offset) rock lithology may be determined.

The first practical application of amplitude-versus-offset (AVO) analysis was introduced by Ostrander (1984). He proposed AVO analysis as a technique for validating P-wave seismic amplitude anomalies associated with gas-sands. Ostrander's findings were based upon a simple three-layer model consisting of two shale layers encasing a sandstone layer. Using published values of Poisson's ratio for shales and brine- and gas-saturated sands, Ostrander observed that gas-sands possessing a low Poisson's ratio, relative to encasing shales, produce an increase in event amplitude with increasing source-receiver offset .

Examples showing P-P AVO analysis being used successfully in identifying gas-sands are shown by Rutherford and Williams (1989) and Chacko (1989). The use of P-SV AVO analysis, on the other hand, is still being developed, and therefore little has been published about it. However, one example of such an analysis was undertaken using vertical-seismic-profile (VSP) data by Coulombe and Stewart (1990).

## 1.5 Thesis Objectives

The objective of this thesis was to undertake the interpretation of a multicomponent seismic data set acquired in the Carrot Creek area of west-central Alberta. The specific topics that are addressed in this thesis are as follows:

- i) Explain differences in responses of the vertical and radial component of the multicomponent data set in terms of both lithology and formation thickness.
- ii) Study amplitude-versus-offset (AVO) effects on both the P-P (vertical-component) and P-SV (radial-component) data.
- iii) Investigate whether variations in lithology can be determined by coupling the P-P and the P-SV interpretation.
- iv) Make a comparison between conventional P-P data, acquired using arrays consisting of nine geophones, and the vertical-component of a multicomponent data set, acquired using single-geophone arrays.
- v) Determine what source-receiver offsets are the most appropriate for imaging specific events on the multicomponent data set in the study area.

In general, this thesis looks at the feasibility of using multicomponent data, acquired using conventional P-wave vibrators, as an exploration tool in the Carrot Creek oilfield. The emphasis of this study being the effects of variation of thickness and lithology, of geologic units, on the P-P and P-SV seismic responses.

## 1.6 Structure of Thesis

The geology found within the Carrot Creek field is discussed in detail in Chapter 2. The processing flows for the Carrot Creek conventional and multicomponent data sets used in this thesis are discussed in Chapters 3 and 4, respectively. The interpretation and analysis of the data sets, including  $V_p/V_s$  and AVO analysis, are undertaken in Chapter 5. Chapter 6 discusses the conclusions made from the results and states the usefulness in acquiring

multicomponent seismic data in the Carrot Creek field.

## **1.7 Seismic Data Sets Used in the Thesis**

Two surface-seismic data sets were utilized in this thesis: a conventional data set consisting of three, vertical-component seismic lines (CR851, CR852 and CR853) and a multicomponent data set consisting of two, 3-component lines (CCSW01 and CCSW02). The locations of all of these lines are shown in Figure 1.3.

### **1.7.1 Conventional data set**

The conventional surface seismic data set was acquired by Suncor in January of 1986. The acquisition and recording parameters utilized for this data set are listed in Table 1.1. The data were acquired using a split-spread geometry with near- and far-offsets of 20 m and 1200 m respectively, and subsurface fold of 2000%.

### **1.7.2 Multicomponent data set**

The multicomponent surface seismic data set was acquired in February of 1987 by Boyd Exploration. The acquisition and recording parameters are listed in Table 1.2. These data were acquired in the northeast to southwest direction using an end-on geometry with a near- and far-offset of 120 m and 2550 m respectively. As the spread reached the south west end of the lines, the source rolled into the spread until an end-on geometry was again obtained with the source at the southwest end of the spread.

## **1.8 Hardware and Software Used**

All seismic processing undertaken in this thesis, with the exception of a common conversion point (CCP) mapping program written by Dave Eaton (The University of Calgary), was performed using Western Geophysical processing software running on a 4381

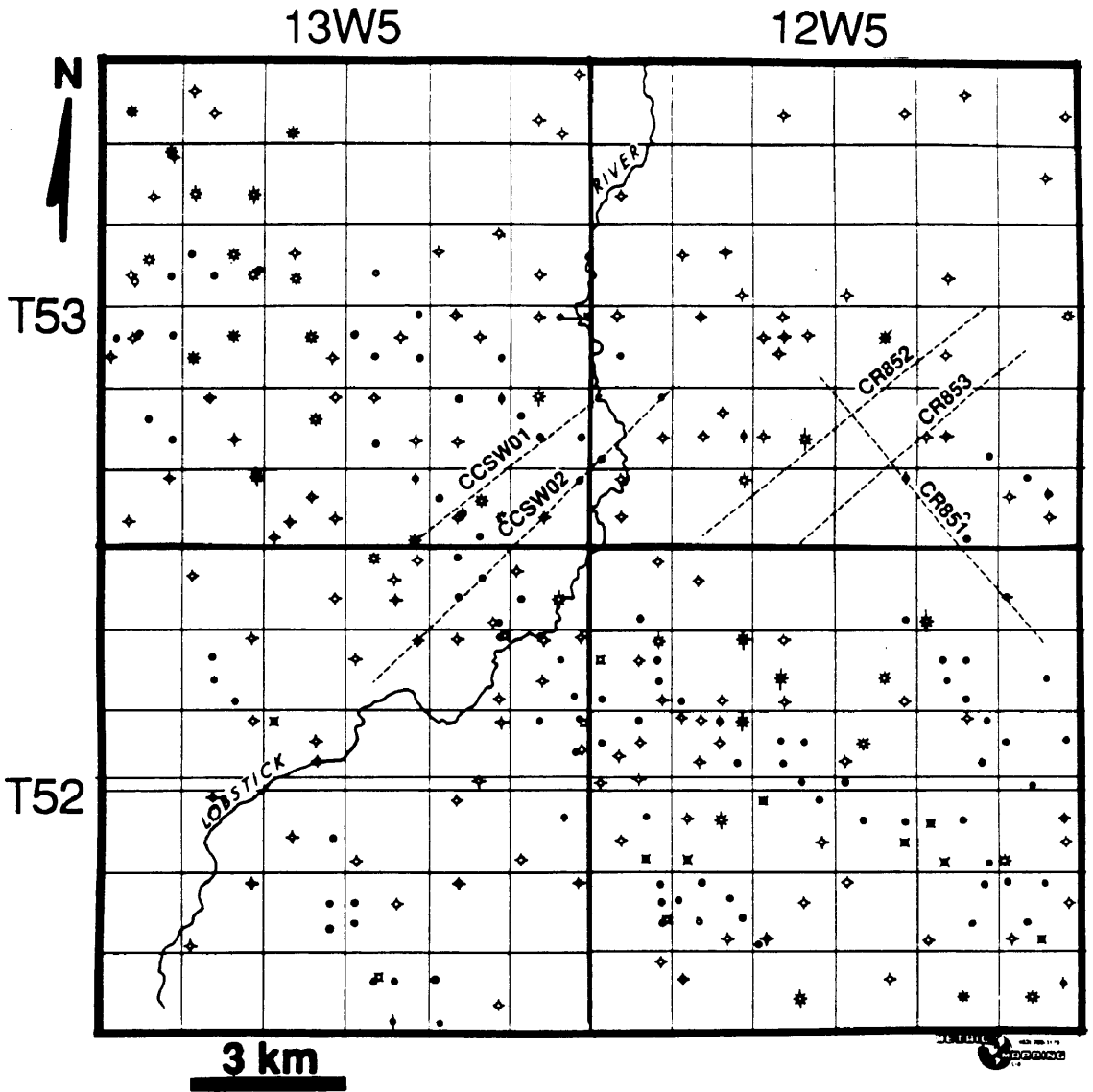


FIG. 1.3. Carrot Creek seismic data.

Table 1.1. Acquisition and recording parameters for the conventional seismic data set.

Source	Dynamite
Depth	15 m
Charge size	1 kg
Amplifier	DFS V
Number of channels	120
Sample rate	2 ms
Geophones / group	9 (2.5 m spacing)
Number of shots:	
CR851	77
CR852	77
CR853	66
Group interval	20 m
Source interval	100 m

Table 1.2. Acquisition and recording parameters for the multicomponent seismic data set.

Source	Vibroseis
Number of vibrators	4
Number of sweeps	10
Sweep frequency	10 - 94 hz
Sweep length	6 s (linear)
Amplifier	Sercel SN348
Number of channels	240
Sample rate	2 ms
Geophones / group	1
Number of shots:	
CCSW01	80
CCSW02	124
Group interval	30 m
Source interval	60 m

IBM mainframe computer operated by the CREWES Project at The University of Calgary.

All seismic modeling was undertaken using software developed by Dr. Don Lawton (The University of Calgary) based upon the solution of the Zoeppritz equations. This was run on a Perkin-Elmer computer of the Department of Geology and Geophysics at The University of Calgary.

Seismic plots presented in this thesis were generated using Versatec plotters driven by a Perkin-Elmer super mini and IBM mainframe computer. The text, tables and figures were created on a Macintosh computer using Microsoft Word, Cricket Graph and MacDraw software packages.

## Chapter 2 - GEOLOGY

### 2.1 Study Area

This study is located in the Carrot Creek area of west-central Alberta, approximately 150 km west of Edmonton (Figure 2.1). The study area encompasses townships 52-53, ranges 12-13 west of the fifth meridian, and is located just northwest of the Pembina oilfield. Initially discovered in 1963, the Carrot Creek field produces primarily from conglomerates, but also some sandstone units of the Cardium Formation (Section 2.2). An estimates of reserves for the field was placed at approximately 7 million barrels of initially recoverable oil and a further 2 million barrels of oil recoverable through waterflood (Bergman and Walker, 1987).



FIG. 2.1. Carrot Creek location map.

## 2.2 Stratigraphy

Due to its location in the Central Plains of Alberta, the Carrot Creek field contains primarily flat-lying stratigraphy. A stratigraphic correlation chart for this area, to the base of the Cretaceous, is shown in Figure 2.2. The primary zone of interest for this field is the Upper Cretaceous Cardium Formation which contains oil reservoirs in stratigraphic traps. It produces from conglomerates and fine-grained sandstones that are believed to have been deposited in a shallow marine environment.

The Cardium Formation in the Carrot Creek area occurs at a depth of approximately 1600 m below surface. It is overlain and underlain by marine shales of the Wapiabi and Blackstone Formations respectively (Williams and Burk, 1964). Krause and Nelson (1984) recognized two distinct lithostratigraphic units within the Cardium Formation itself; the Cardium Zone Member and the Pembina River Member (Figure 2.2). Although this stratigraphy was based upon lithologies found in the Pembina field, it is consistent with those found in the Carrot Creek field (Krause and Nelson, 1984). The Cardium Zone Member, in the Carrot Creek field, consists primarily of marine shales with infrequent pebbly stringers (Krause and Nelson, 1984). The top of this member is marked by a chert pebble and nodular siderite layer. It is characterized on well logs by having low SP (self potential) and sonic velocity but high resistivity and gamma-ray response. Typical log responses are shown in Figure 2.3.

The Pembina River Member underlies the Cardium Member and is made up of a coarsening-upward sequence of sediments (Krause and Nelson, 1984). It is variably thick throughout the Carrot Creek area, reaching a maximum thickness of 30 m (Joiner, 1989). The sediments grade from silty mudstone at the base of the member through to sandstone and, in some cases, into thick conglomerates (Krause and Nelson, 1984). It is the presence of these thick conglomerates which distinguish the Carrot Creek field from the Pembina field. These conglomerates are found in bodies of up to 20 m thick (Plint et al., 1986) and are the primary

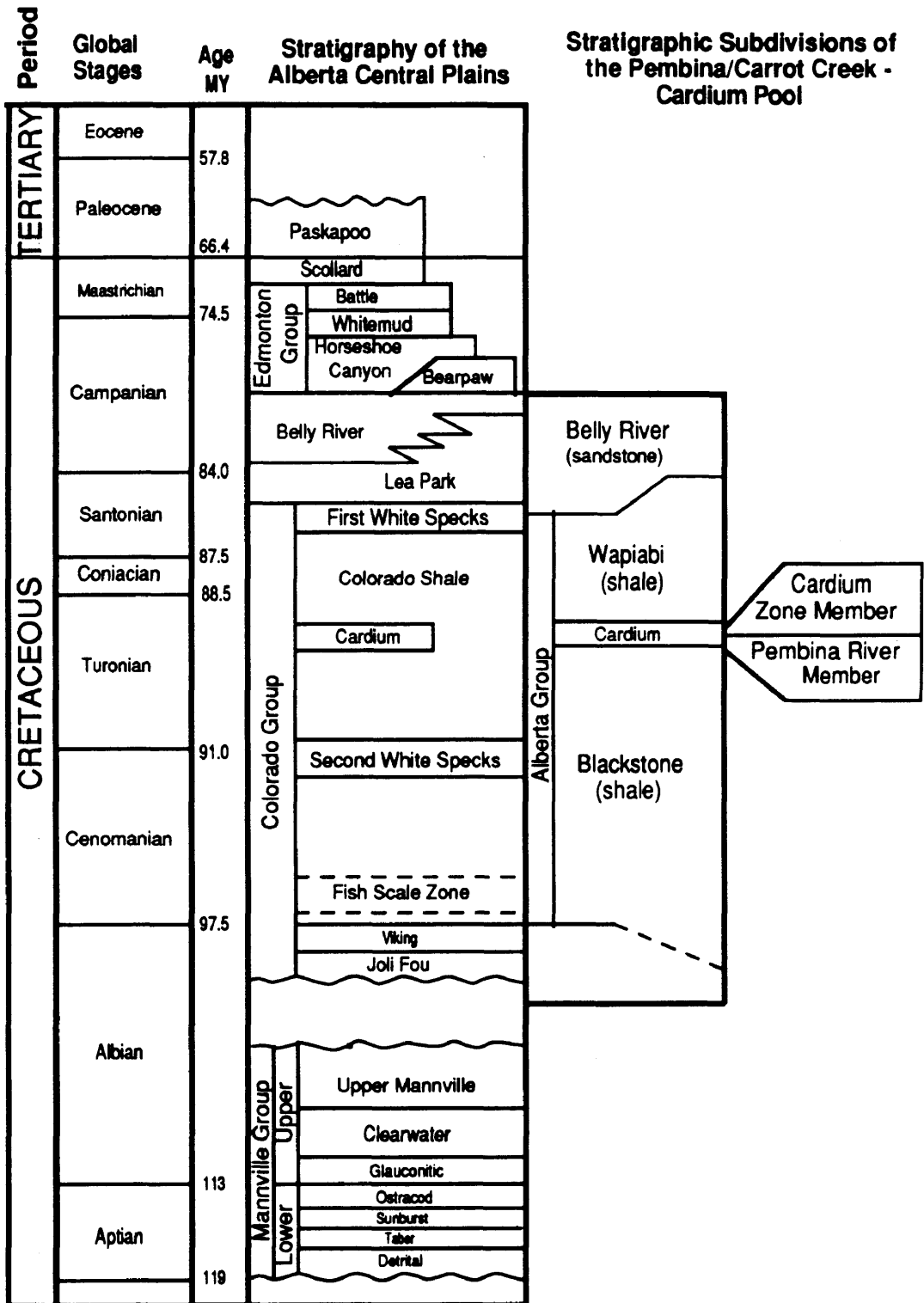


FIG. 2.2. Stratigraphic correlation chart for the Alberta Central Plains (AGAT Laboratories, 1987) and the stratigraphic subdivisions of the Pembina/Carrot Creek Cardium Pool (Williams and Burk, 1964; Krause and Nelson, 1984).

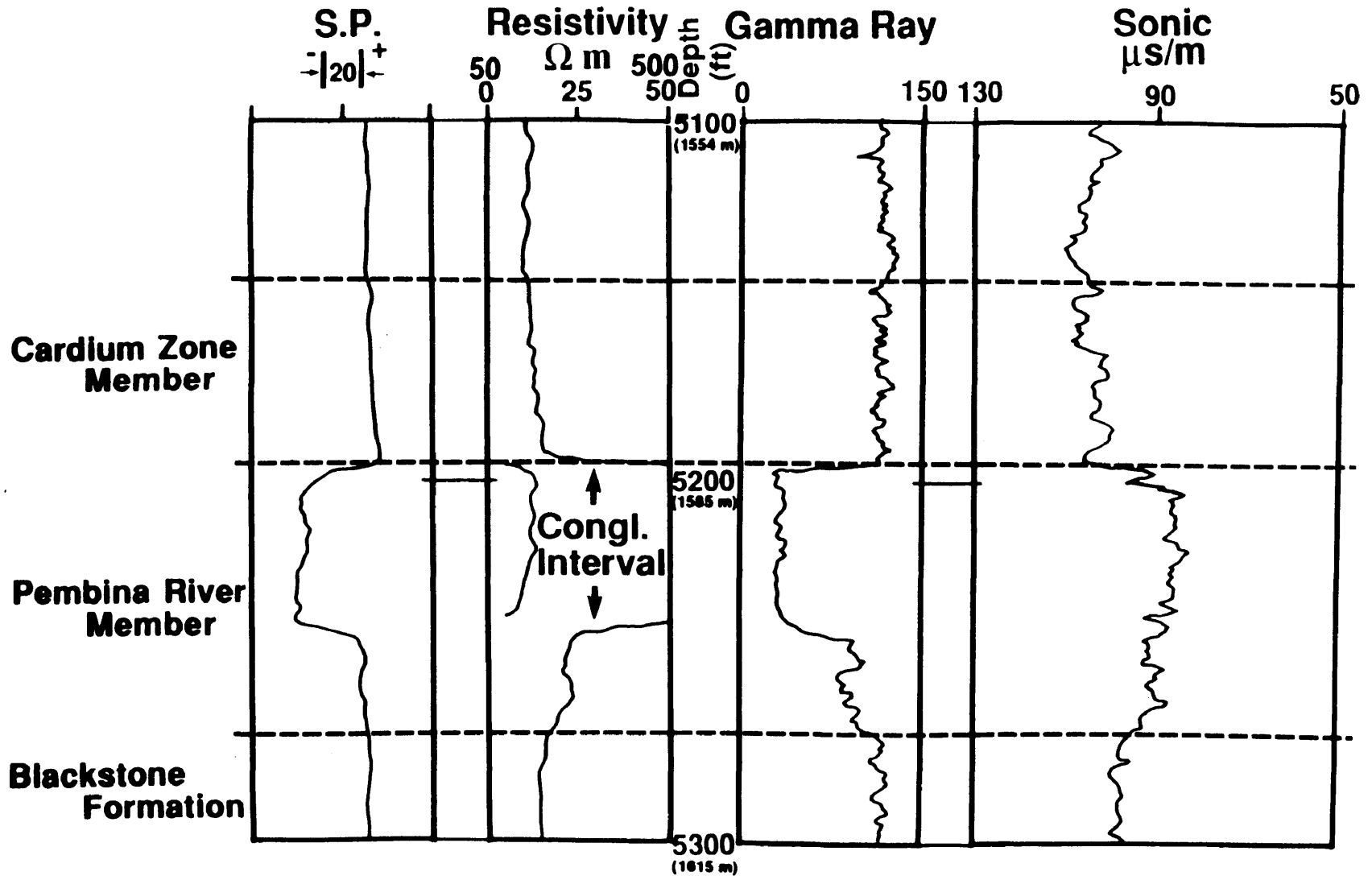


FIG. 2.3. Characteristic well-log response of the Cardium Formation taken from well 10-35-52-13W5. The location of this well is identified in Figure 2.6.

reservoir rocks for the Carrot Creek field.

The transport mechanisms and depositional environments of these conglomerate bodies have been debated for many years. The seeming contradiction of having coarse conglomerates contained within what are believed to be offshore muds has nurtured many theories as to their origin. Two of the most recent theories to be proposed are those of Krause and Nelson (1984) and Bergman and Walker (1987).

Krause and Nelson (1984) believe these conglomerates were deposited upon a series of shelf ridges by a combination of storm-induced currents and wave action during a time of low sea-level. This theory was also supported by Joiner (1989). Bergman and Walker (1987), on the other hand, suggested that the conglomerates can be explained by sea-level changes and shoreface incision. Gravel was worked, by wave action, alongshore into the resulting erosional hollows to produce the conglomerate bodies.

The conglomerate itself can only be identified on well logs with confidence using micro-resistivity logs (Krause, personal communication), but unfortunately the study area contains very few of these. The high resistivity zone found in the Pembina River member may, however, indicate the presence of conglomerate. This zone is also identified by large downward shifts in the gamma-ray and SP responses and an increase in the sonic velocity (Figure 2.3). This interval shall be referred to hereafter as the conglomerate interval. Figure 2.4 shows an isopach map of this interval, based upon the examination of logs from all wells shown on this map. Variation in this isopach in turn is hoped to be an indication of the variation in conglomerate thickness. The possible location of several northwest-southeast trending conglomerate bodies can be identified, in Figure 2.4, by an increase in the isopach values. These possible conglomerate locations are confirmed by their correlation with the locations of producing conglomerate deposits. Figure 2.5 is a cross-section for the Wapiabi-Blackstone interval across two producing conglomerate deposits in the Carrot Creek field,

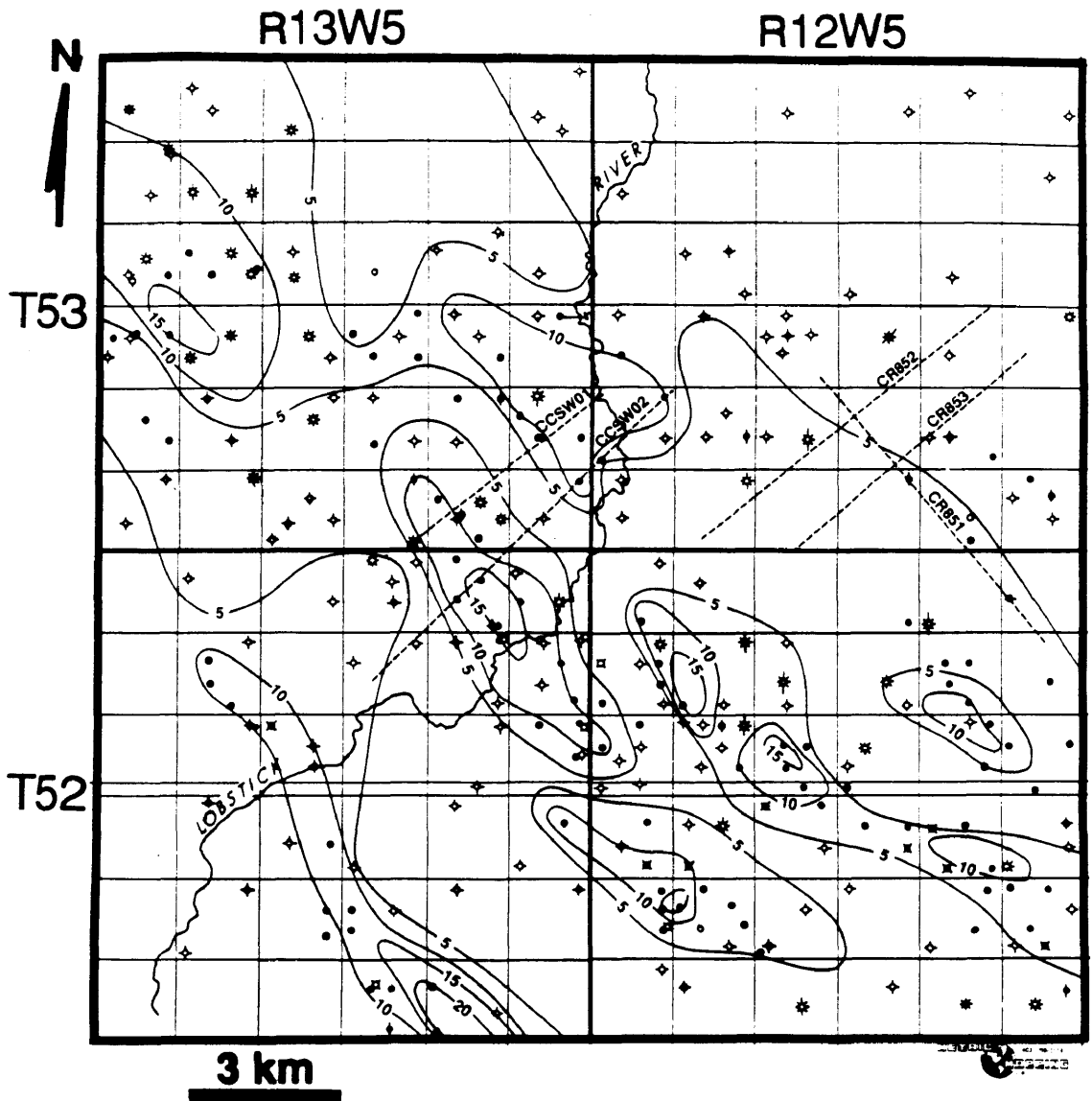


FIG. 2.4. Isopach map of high resistivity zone within the Cardium Formation - higher contour values may reflect location of conglomerate bodies.

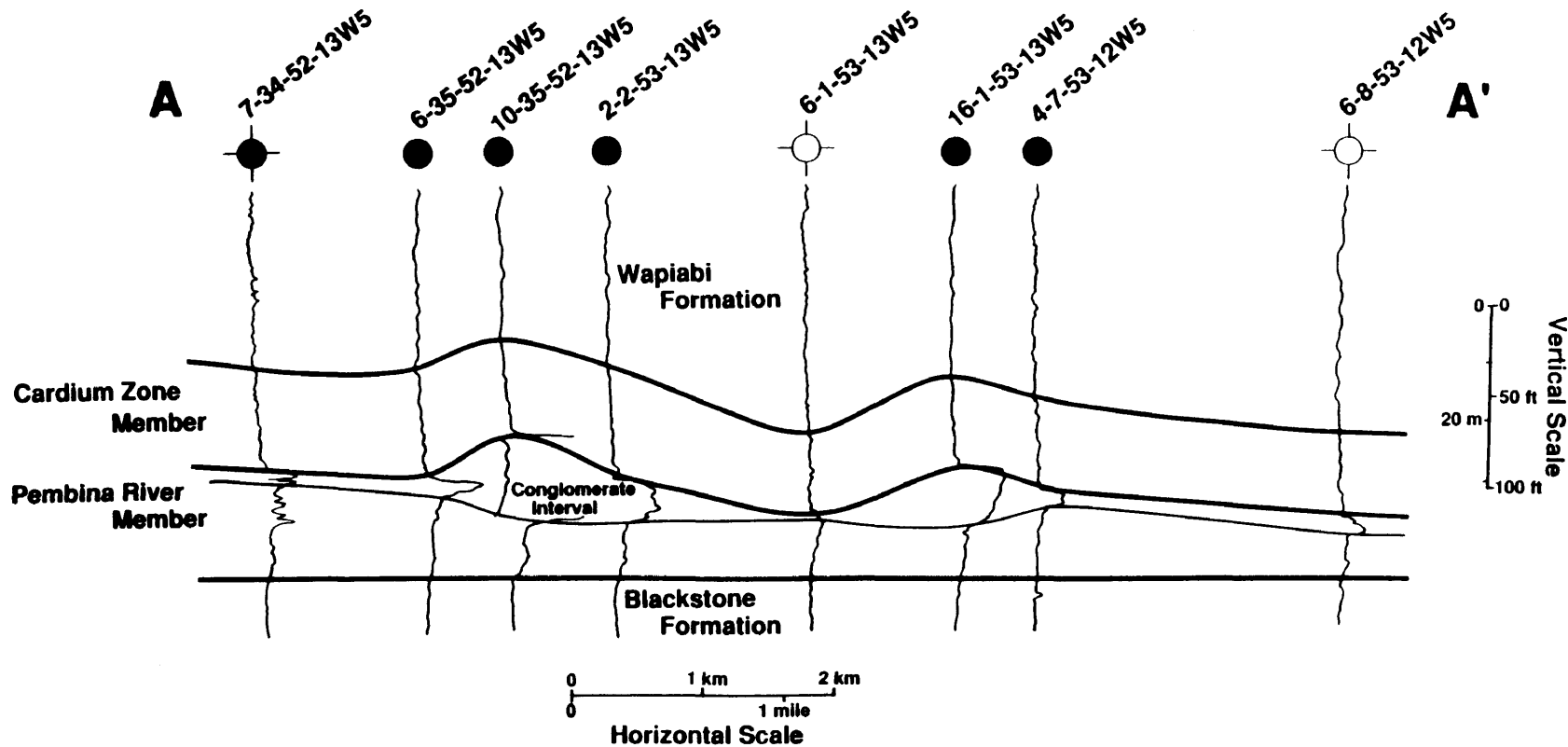


FIG. 2.5. Cross-section A-A' of the Wapiabi-Blackstone interval (the resistivity curve of each well is included). The cross-section is flattened on the Blackstone Formation.

and shows typical thickness variations in the Pembina River Member, due primarily to variation in conglomerate thickness. The line of section is shown in Figure 2.6 and was chosen to coincide as closely as possible with a multicomponent seismic line.

The lack of major structural trapping for the area is indicated by the structure map of the top of the conglomerate interval (i.e. top of the Pembina River Member), shown in Figure 2.7. This map indicates a northeast-southwest regional dipping structure with no structural closure present at the location of the producing wells.

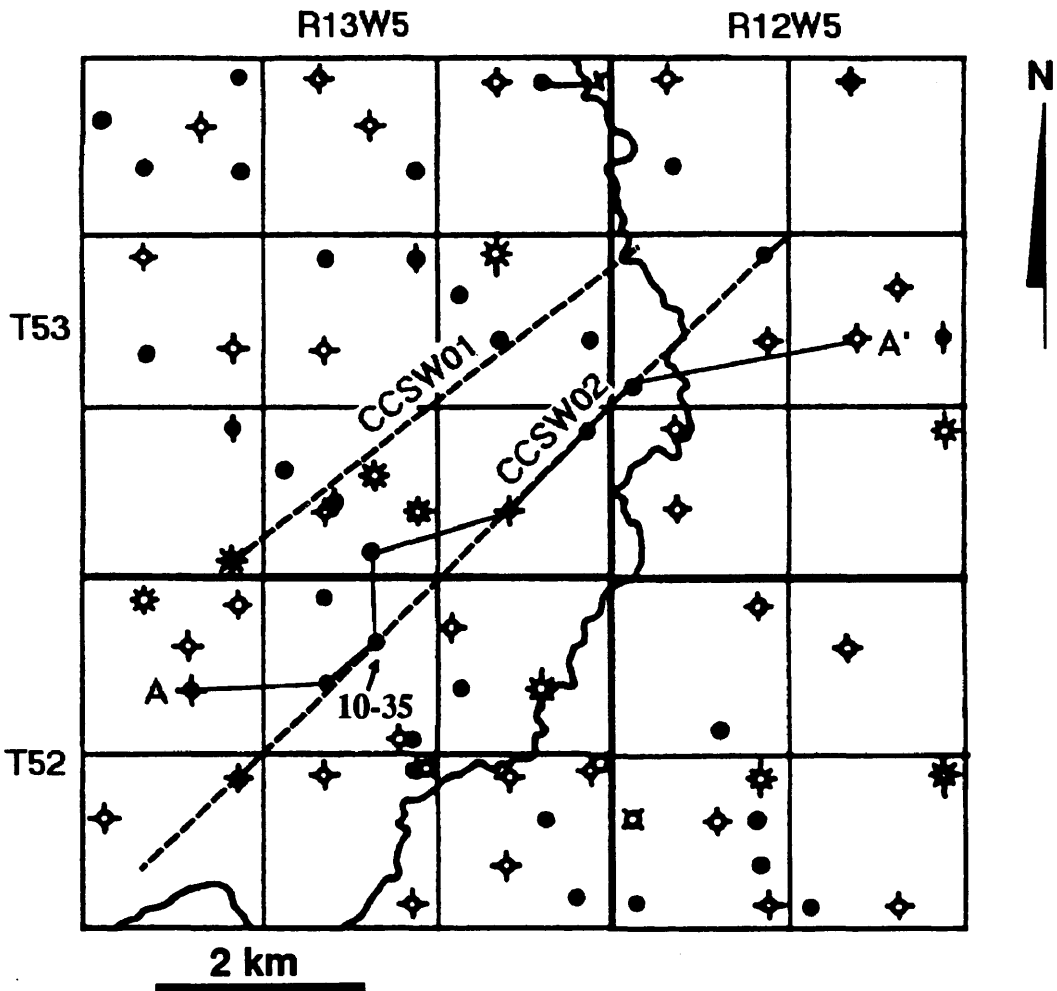


FIG. 2.6. Orientation of cross-section (A-A') and the two multicomponent seismic lines.

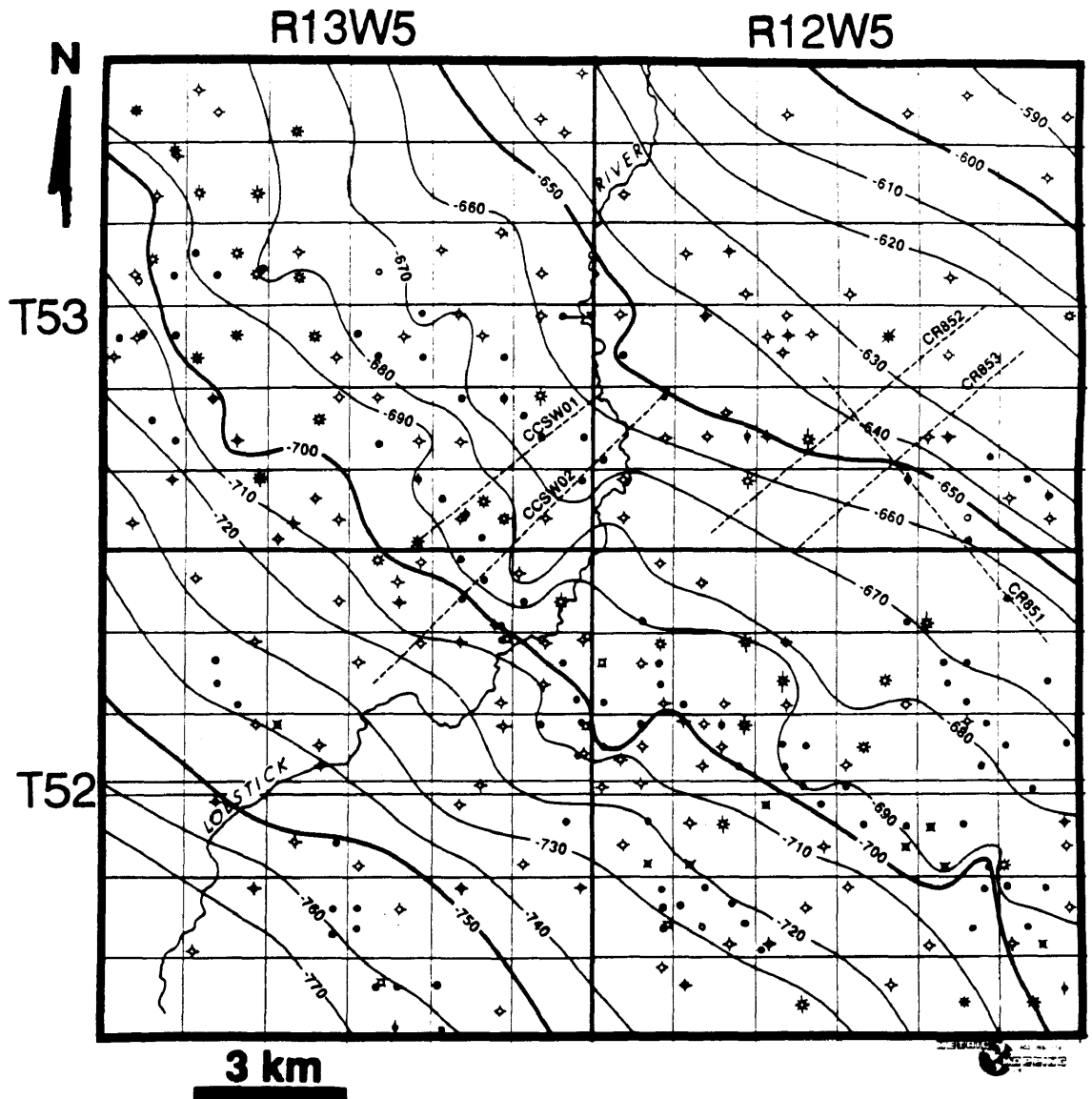


FIG. 2.7. Structure map of the top of conglomerate interval (i.e. top of the Pembina River member), relative to sea-level. The contour interval is 10 m.

## **Chapter 3 - DATA PROCESSING (Conventional)**

### **3.1 Introduction**

This chapter discusses, in detail, the processing flow applied to the conventionally acquired seismic data (lines CR851, CR852 and CR853 of Figure 1.3). This flow is summarized in Figure 3.1, with each processing step discussed in the following sections. All processing was undertaken using Western Geophysical software. Figure 3.2 shows an example of typical shot records from the conventional data set possessing varying data quality. These records are generally characterized by a good signal-to-noise ratio and strong refractions. Surface waves can also be seen in these records.

### **3.2 Preprocessing**

#### **3.2.1 Demultiplexing**

During seismic acquisition, data are recorded in multiplexed format (i.e. time-sequential format). In order to undertake data processing this data had to be re-organized into trace-sequential format. This procedure is a matrix transpose operation and is referred to as demultiplexing (see e.g. Krebs, 1988).

#### **3.2.2 Geometry and Editing**

Based upon survey information and observer logs, source-receiver geometries and elevations were input to the trace headers. Noisy traces were also removed to minimize the detrimental effect on the signal-to-noise ratio of the final section.

#### **3.2.3 Correction for Spherical Divergence**

As a seismic wave propagates away from a source, its amplitude decays with distance traveled. This decay is due to three factors; spherical divergence (i.e. geometrical spreading)

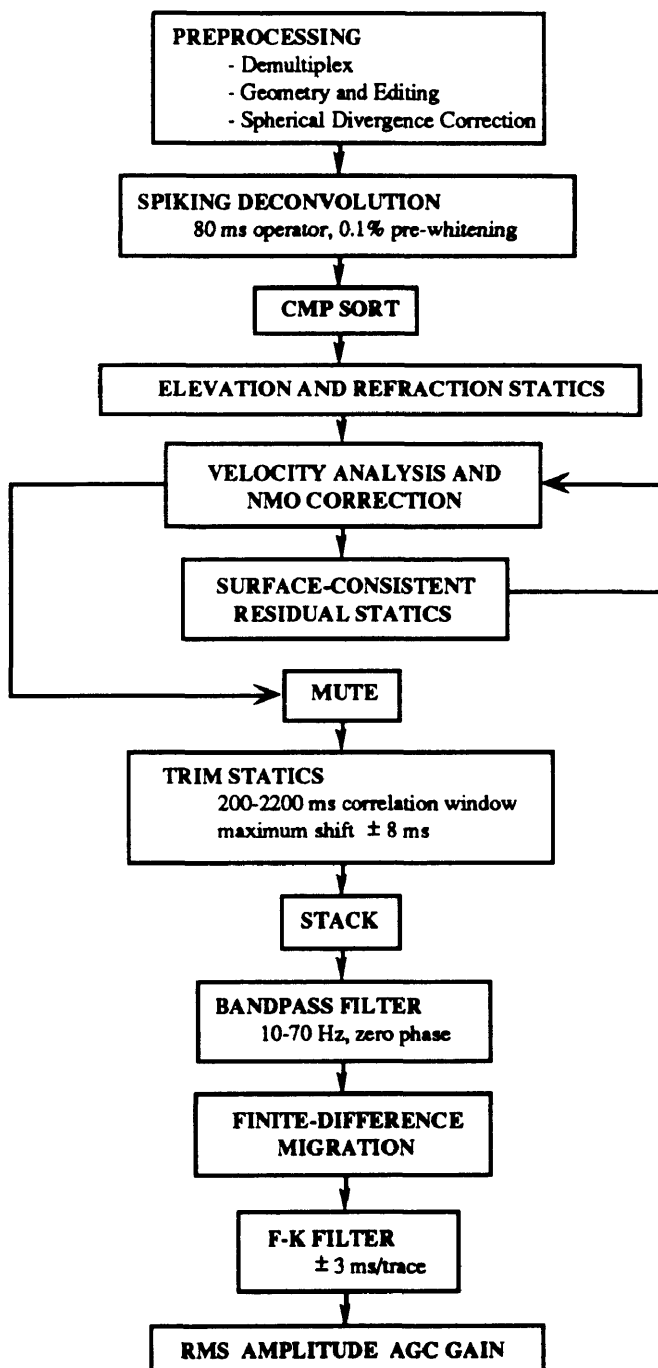


FIG. 3.1. Seismic data processing flow (conventional data).

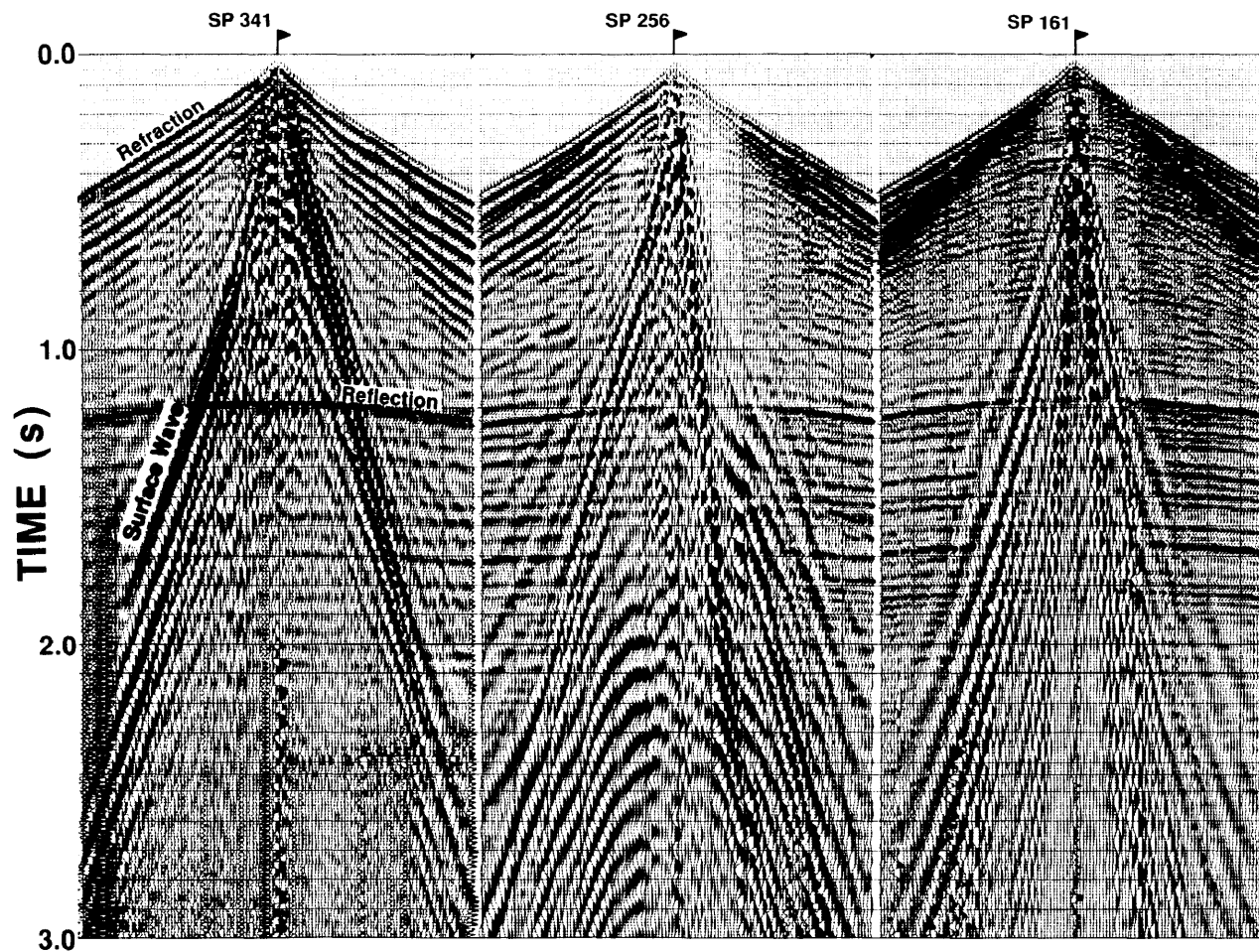


FIG. 3.2. Shot records from line CR851 showing varying data quality (records scaled using an RMS amplitude AGC gain). The maximum offset is 1200 m.

of the wavefront, reflection and transmission losses, and attenuation (i.e. anelastic absorption; Krebs, 1988). Spherical divergence contributes the most to amplitude decay and is generally corrected for by applying a gain recovery function to the data. Newman (1973) showed that, for a layered earth, amplitude decay can be described approximately by:

$$D_0 = \frac{tV_{rms}^2}{V_1} \quad (3.1)$$

where  $t$  is the two-way reflection time,  $V_{rms}$  is the rms-velocity and  $V_1$  is the velocity of the first layer. This was the geometric spreading compensation used in this study.

### 3.3 Spiking Deconvolution

Spiking deconvolution was applied pre-stack to each trace to sharpen the reflection events and to restore the amplitudes of the high frequencies lost by attenuation. Before deconvolution, pre-whitening of the amplitude spectrum was undertaken (i.e. adding an artificial level of white noise to the trace's amplitude spectrum). Prewhitening prevents zeroes in the amplitude spectrum which would cause high-frequency pre- and post-event noise after deconvolution (Yilmaz, 1987). For these data, an 80 ms deconvolution operator was applied, along with prewhitening of 0.1%.

### 3.4 CMP Sort

In order to undertake further processing, the data had to be transformed from shot-receiver to midpoint-offset coordinates (Yilmaz, 1987); this is referred to as CMP (common midpoint) or CDP (common depthpoint) sorting. This procedure involves sorting traces with common source-receiver midpoints into what are called CMP gathers. The geometry of a typical CMP gather is shown in Figure 3.3. The number of traces contained within each gather is referred to as the fold (maximum fold for this data set is 20).

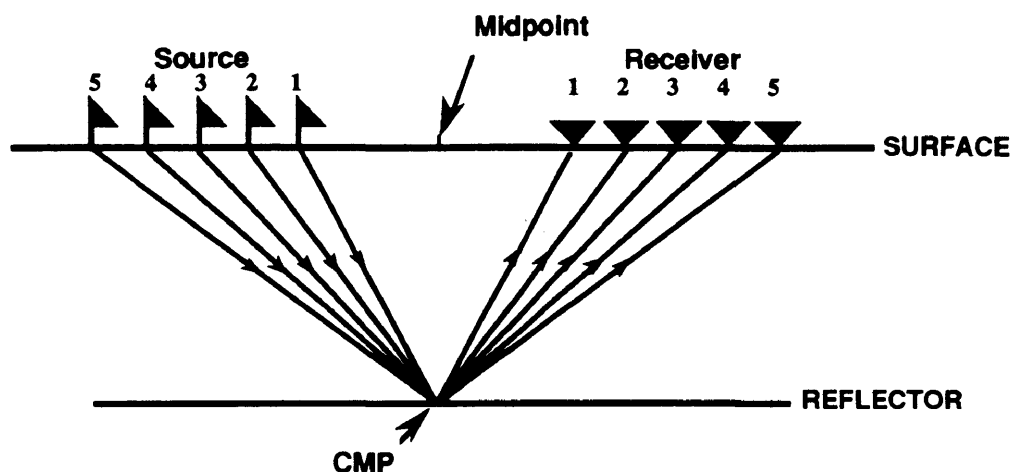


FIG. 3.3. Geometry of a typical CMP gather (after Yilmaz, 1987).

### 3.5 Elevation and Refraction Statics

To obtain a true representation of the subsurface using seismic reflection data both static and dynamic corrections are required to put the individual traces into their proper time position (Keary and Brooks, 1984). This section discusses the static correction, the dynamic correction will be discussed in Section 3.6.

Elevation differences between source locations and receivers as well as the presence of irregular low-velocity layers have the effect of shifting traces out of their proper time location. In Alberta, two low-velocity layers have to be considered: a weathering layer and a drift layer. The weathering layer is a near-surface layer consisting primarily of unconsolidated earth (Sheriff, 1991). The drift layer, on the other hand, consists of glacial deposits which are highly variable in thickness. Without correcting for variations in elevation, weathering and drift layer thicknesses, apparent structural relief may appear on underlying reflectors. To eliminate this effect, the sources and receivers are corrected to a datum plane and travel-time variations due to these low-velocity layers are removed. This correction is accomplished by applying a static or bulk time shift to each trace. This procedure, in effect, replaces the highly variable low-velocity layers with a constant velocity layer. Based upon the P-headwave first breaks, the replacement velocity of this layer was chosen to be 3050

m/s.

In order to determine the static correction for each shot and receiver, knowledge of the velocities and thicknesses of the weathering and drift layers had to be determined. This information, with the exception of the velocity of the weathering layer, was obtained from refractions (first breaks) recorded on each shot record (Figure 3.2). The weathering layer velocity was determined from the uphole times of each shot and averages approximately 650 m/s.

For this thesis all first breaks were picked by hand and then input into Western Geophysical's Extended Generalized Reciprocal Method algorithm (EGRM). This algorithm is based upon the GRM of refraction interpretation presented by Palmer (1980). An example of the refraction model and static corrections obtained from line CR851 using the above algorithm is shown in Figures 3.4. Static corrections were computed for a datum elevation of 875 m.

### 3.6 Velocity Analysis and NMO Correction

Before a stacked section could be generated, the effects of normal moveout (NMO) had to be removed (i.e. dynamic correction). The larger the source-receiver offset, the greater is the reflection traveltime, producing a hyperbolic moveout of the event. For an n-layer case NMO can be expressed by the following equations:

$$t_{nmo} = t_x - t_0 \quad (3.2)$$

where,

$$t_x^2 = t_0^2 + \frac{X^2}{V_{rms}^2}, \quad (3.3)$$

$t_{nmo}$  is the normal moveout,  $t_x$  is the traveltime for a source-receiver separation of  $X$ ,  $t_0$  is the zero-offset traveltime and  $V_{rms}$  is the rms-velocity.

To correct for NMO, using equation 3.2,  $V_{rms}$  was determined by generating velocity spectra (i.e. semblance plots) for several CMP gathers from each line. A sample velocity spectra is shown in Figure 3.5. Note the velocity function increases quickly in the first 900

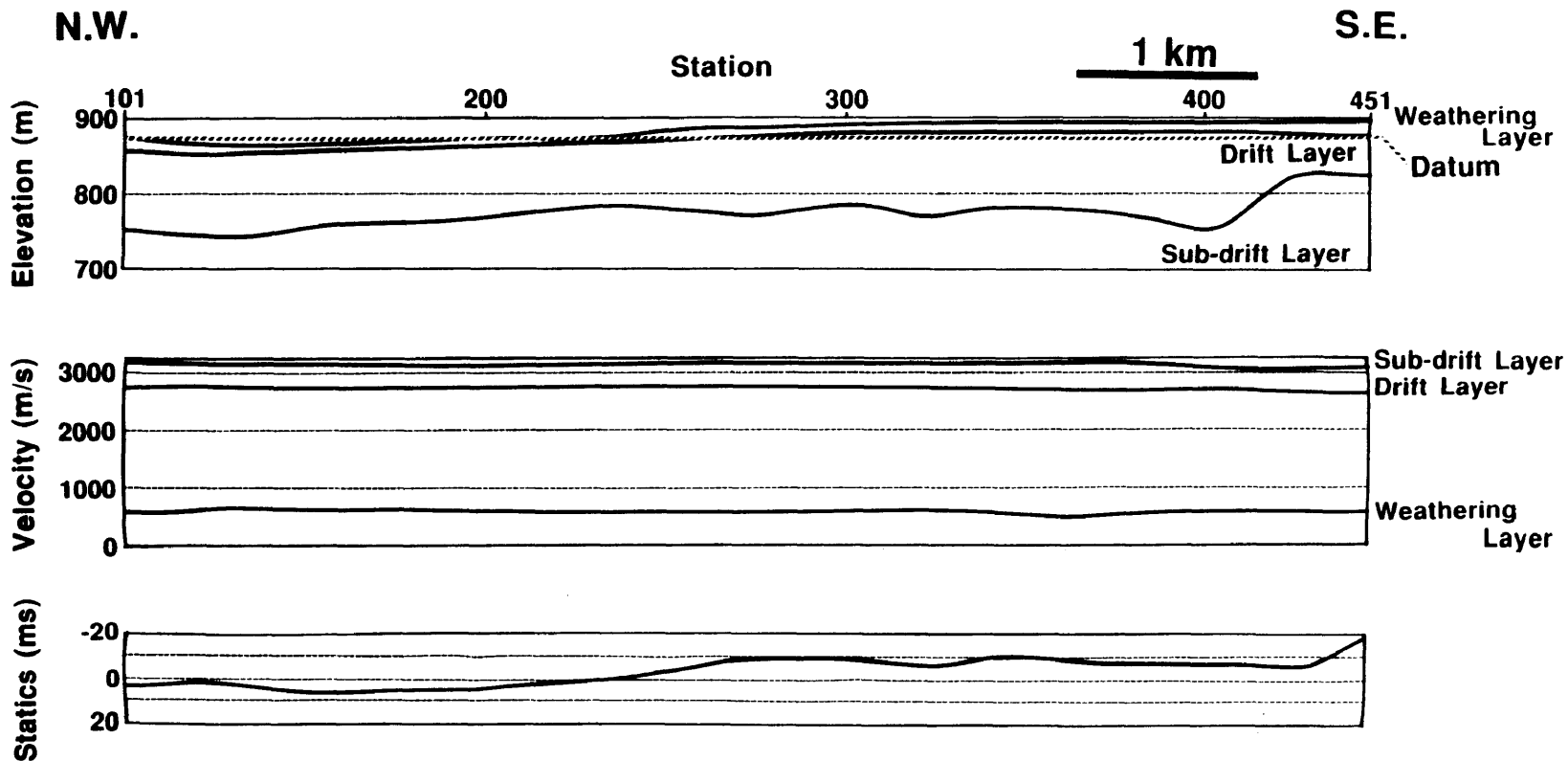


FIG. 3.4. Refractor model for line CR851, determined using uphole times and first breaks, and the resulting static correction.

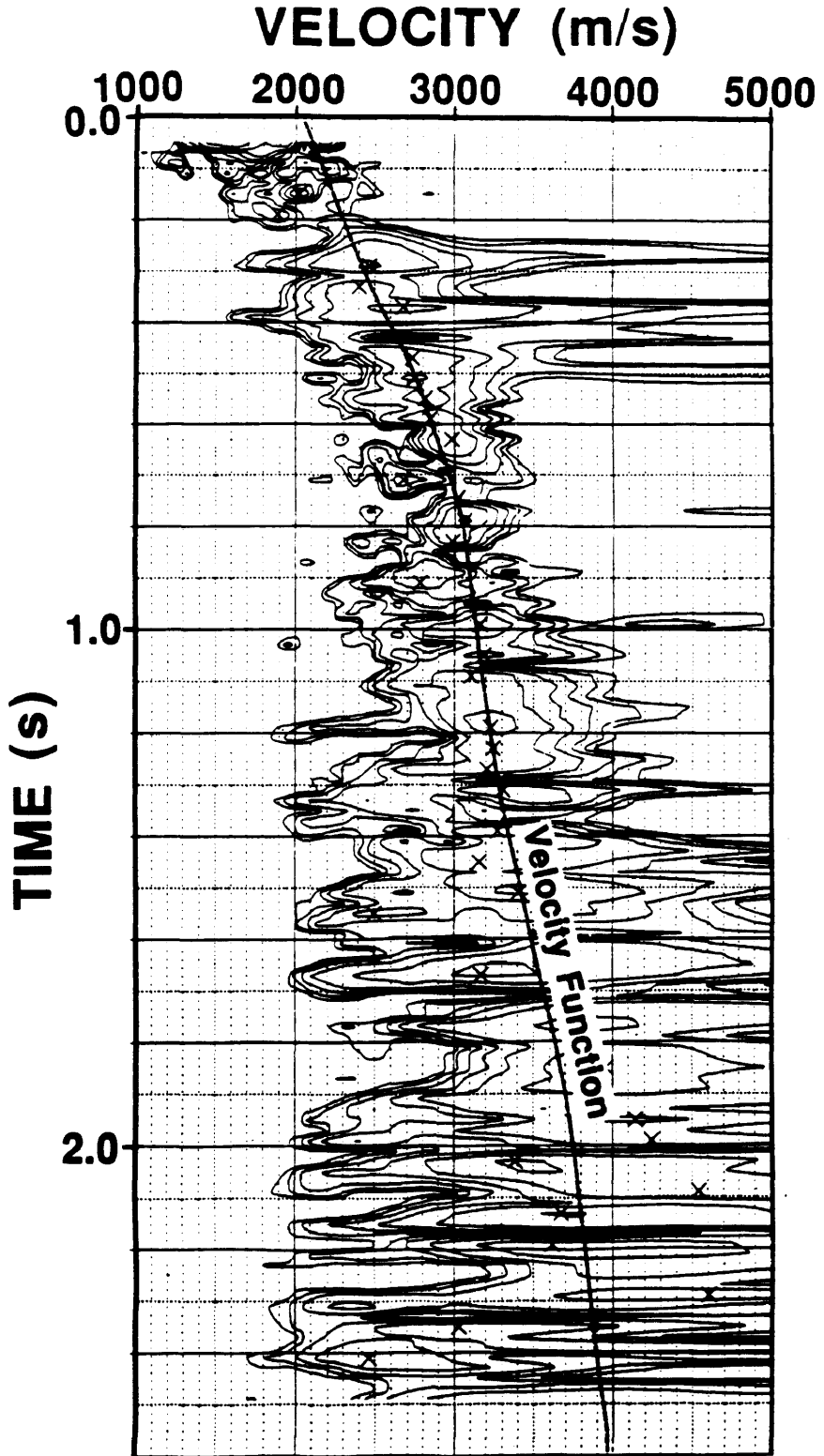


FIG. 3.5. Velocity spectrum for CMP 222 of line CR851. The velocity function based upon maximum semblance is also shown.

ms and then much more gradually. Each spectra was generated by repeatedly NMO-correcting and stacking the gather, thus producing a plot of semblance versus stacking velocity and two-way zero-offset time. The largest semblances on this plot correspond to the best stacking velocities and therefore were used as the velocity function. Since very little variation in velocity was observed for different CMP gathers, only two velocity functions were used for each line. The velocity functions used are listed in Appendix A.

### 3.7 Surface Consistent Residual Statics

Although the refraction statics, discussed in Section 3.4, remove much of the distortion caused by near surface irregularities, it is often unable to correct for abrupt changes in surface elevation and in weathering layer thickness and velocity (Yilmaz, 1987). To remove distortions caused by these changes, residual static corrections were applied.

In this thesis, surface-consistent residual statics were applied. Surface consistency assumes that all static shifts are dependent only on source and receiver locations, not on the raypath along which the energy travels (Sheriff, 1991). This assumption is believed to be valid because the low velocity of the weathering layer, with respect to the underlying rock velocities, will tend to cause the raypaths to be vertical. Yilmaz (1987) shows that the traveltime  $t_{ijh}$  corresponding to the  $i$ th and  $j$ th receiver and source station respectively along the  $h$ th horizon can be approximately modeled as:

$$t_{ijh} = s_j + r_i + G_{kh} + M_{kh}X_{ij}^2 \quad (3.4)$$

where  $s_j$  and  $r_i$  are the residual statics of the  $j$ th source and  $i$ th receiver,  $G_{kh}$  is the difference in 2-way travel-time between a reference CMP location and the travel-time along the  $h$ th horizon at the  $k$ th CMP location,  $M_{kh}$  is the residual moveout term and  $X_{ij}$  is the source-receiver offset.

The determination of the individual components of  $t_{ijh}$  is a least-squares problem that

minimizes the error ( $E$ ) between the square of the difference of the observed pick times  $t'_{ijh}$  and the modeled time  $t_{ijh}$ ,

$$E = \sum_{ijh} (t_{ijh} - t'_{ijh})^2. \quad (3.5)$$

The observed pick times  $t'_{ijh}$  are determined using a pilot trace scheme (Yilmaz, 1987). This scheme takes an NMO-corrected gather and produces a stacked (pilot) trace from this gather over a specified window. A window from 600 to 2200 ms was chosen for this procedure because it contained the most coherent events, therefore allowing good correlation. Each trace in the gather is then cross-correlated with this pilot trace to determine the time shift  $t'_{ijh}$ . To minimize the risk of correlating the wrong events, the maximum time shift was placed at  $\pm 8$ ms. Using the time-shifted traces of the gather a new pilot trace is generated and used to produce the final values for  $t'_{ijh}$ . Starting with the previous pilot trace this procedure is repeated for the next CMP gather.

The solution of equation 3.4 using equation 3.5 was accomplished by using an iterative procedure known as the Gauss-Seidel method (see e.g. Wiggins et al., 1976). The resulting source- and receiver residual statics were then applied to the proper traces.

### 3.8 Front-end Mute

Although the high-amplitude direct arrival and refraction events are useful in determining the static solution for a seismic reflection survey (Section 3.4) it is only the reflected energy that is desired on the final stacked section. This first-break energy, if retained, would reduce the final stack quality and therefore it is digitally erased through a procedure known as muting. The mute applied to all three lines was defined by two points. The mute was interpolated between the tenth station away from the source-point (i.e. 300 m offset) and the far-offset station (i.e. 1200 m) removing all data before 340 and 700 ms respectively. The mute was not extended to the source (i.e. 0 m offset) in order to retain shallow events.

### **3.9 Trim Statics**

The primary purpose of the application of trim statics is to enhance the appearance of stacked reflections. Unlike the residual-static technique described in Section 3.7 this procedure is not surface-consistent. This technique correlates traces of an NMO-corrected CMP gather with a model trace over a specified time window. The window chosen for this data set ranged from 200 to 2200 ms and was chosen because most of the reflection events are found within it. The model trace used in the correlation was a conventional stack of all traces within a central gather and those contained in two gathers on each side (ie. there is a different model trace for each gather). Unlike the residual statics technique of section 3.7, each trace was then shifted by amounts corresponding to the shifts required for maximum cross-correlation. Because this technique is not surface-consistent (i.e. source and receiver statics not determined) and therefore could remove structural features, the maximum shift allowed was set at  $\pm 8$  ms. Any smaller shift would not remove some of the larger residual statics while any larger value could cause miscorrelation of events.

### **3.10 CMP Stack**

The traces in each NMO-corrected CMP gather were next stacked (ie. summed) to produce a single trace. The purpose of CMP stacking is to enhance reflections and attenuate random noise. Stacking also has the characteristic of attenuating unwanted multiple reflections (Yilmaz, 1987).

### **3.11 Bandpass Filtering**

In seismic surveys the primary reflection signal is generally found over a specific frequency range. Above and below this desired range, high- and low-frequency coherent noise due, for example, to machinery and surface waves, respectively, is present. Random

noise will also be present but this is generally found over the entire seismic-frequency spectrum. If not removed or reduced in amplitude, these noise types would have a detrimental effect upon the final quality of the stack section. To remove these unwanted frequencies a bandpass filter is applied to the data. This filter passes all frequencies within a certain range and rejects others.

This filtering was undertaken in this study in the time-domain by convolving the trace with a band-limited zero-phase filter wavelet. The output trace then contains only the frequencies that were contained in the filter wavelet (Yilmaz, 1987). To determine the pass range of the filter a panel display of a CMP gather, after deconvolution, filtered by various narrow bandpass filters was generated (Figure 3.6). This display shows that the primary reflections occur predominantly in the 10-70 Hz range and therefore this bandpass range was chosen for the filter. The resulting bandpass-filtered stacked section of line CR852 is shown in Figure 3.7.

### **3.12 Finite-difference Migration**

Migration is a seismic processing technique which maps seismic data to their true lateral and time locations. The purpose is to produce a stacked section that shows the subsurface geologic structure in its true position (Yilmaz, 1987). This thesis uses the finite-difference migration method developed by Claerbout and Doherty (1972). This technique locates the true position of scatterers and reflectors by back-propagating the recorded wavefield into the subsurface.

The final migrated stacked sections of lines CR851, CR852 and CR853 are shown in Figures 3.8, 3.9 and 3.10, respectively. Because very little structural relief is present in the study area, the migration had minimal effects upon the final stacks. This can be seen when comparing the unmigrated stack of Figure 3.7 with the corresponding migrated stack of Figure 3.9. One difference that can be observed between the unmigrated and migrated final

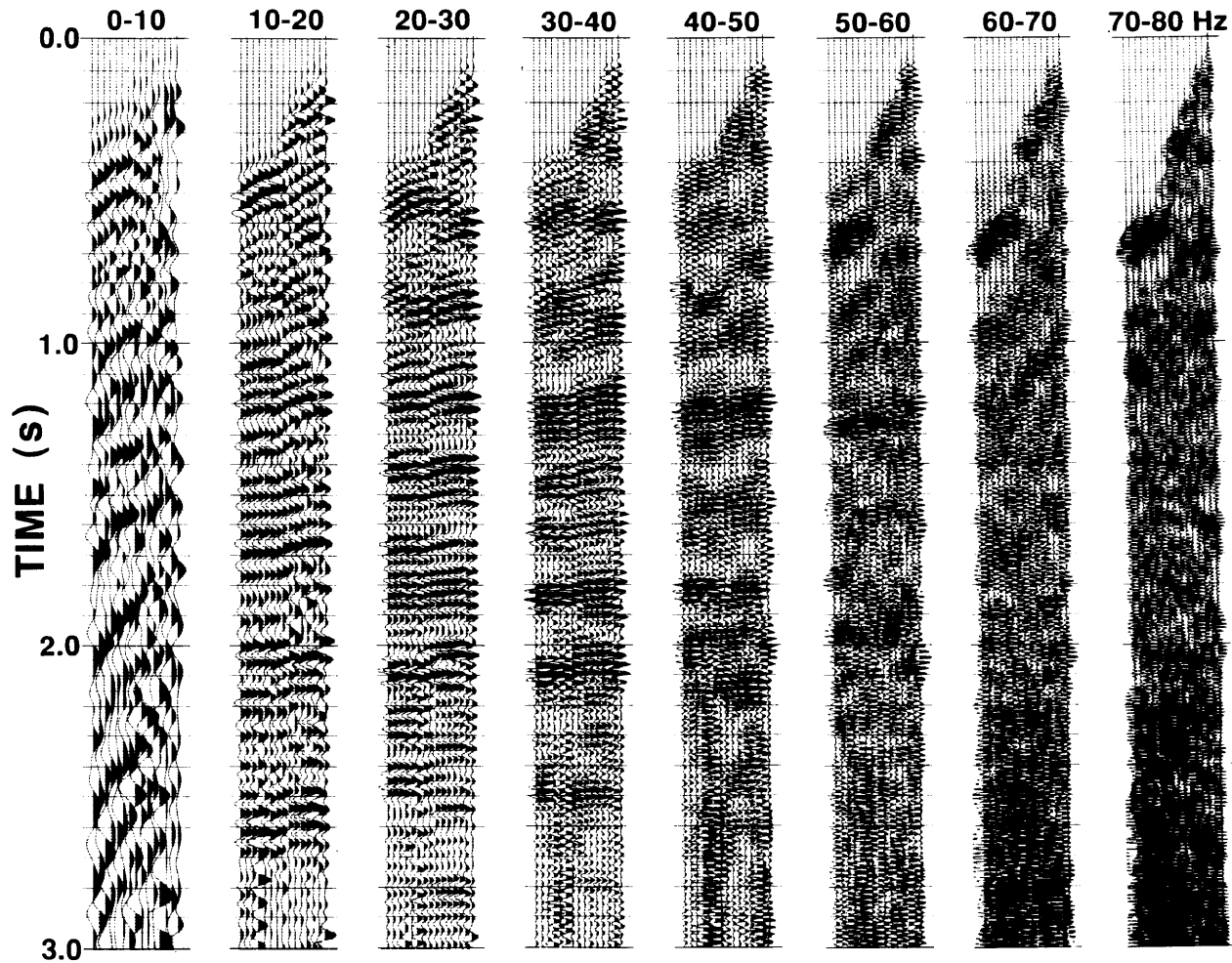


FIG. 3.6. Frequency panels of CMP gather 200 from line CR851. Note that although some reflection energy can be observed in the 60-70 Hz panel most of the energy is contained in the 10-40 Hz range (RMS amplitude AGC gain applied).

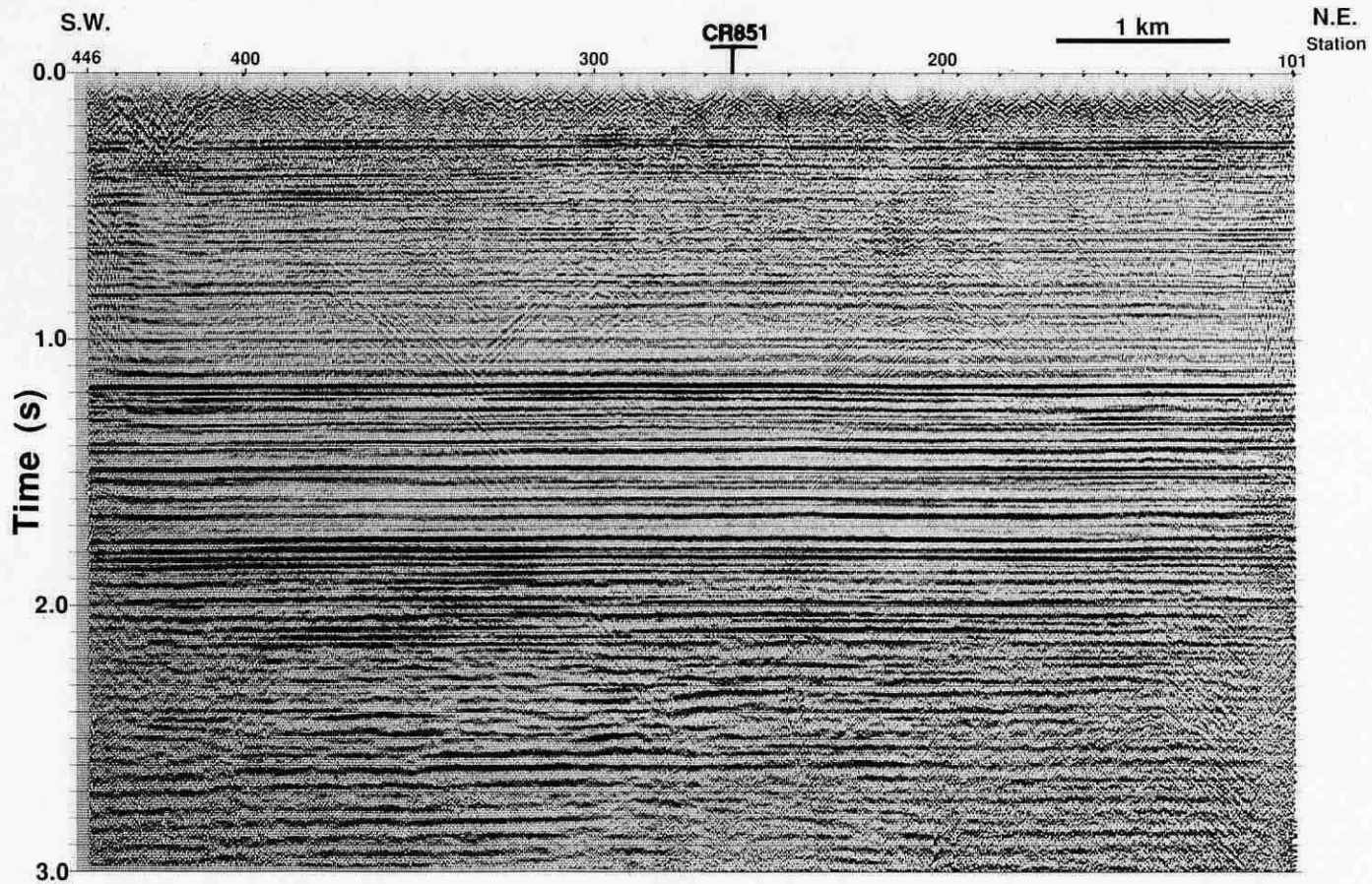


FIG. 3.7. Stack of line CR852 with final statics and 10-70 Hz bandpass filter applied (RMS amplitude AGC gain applied).

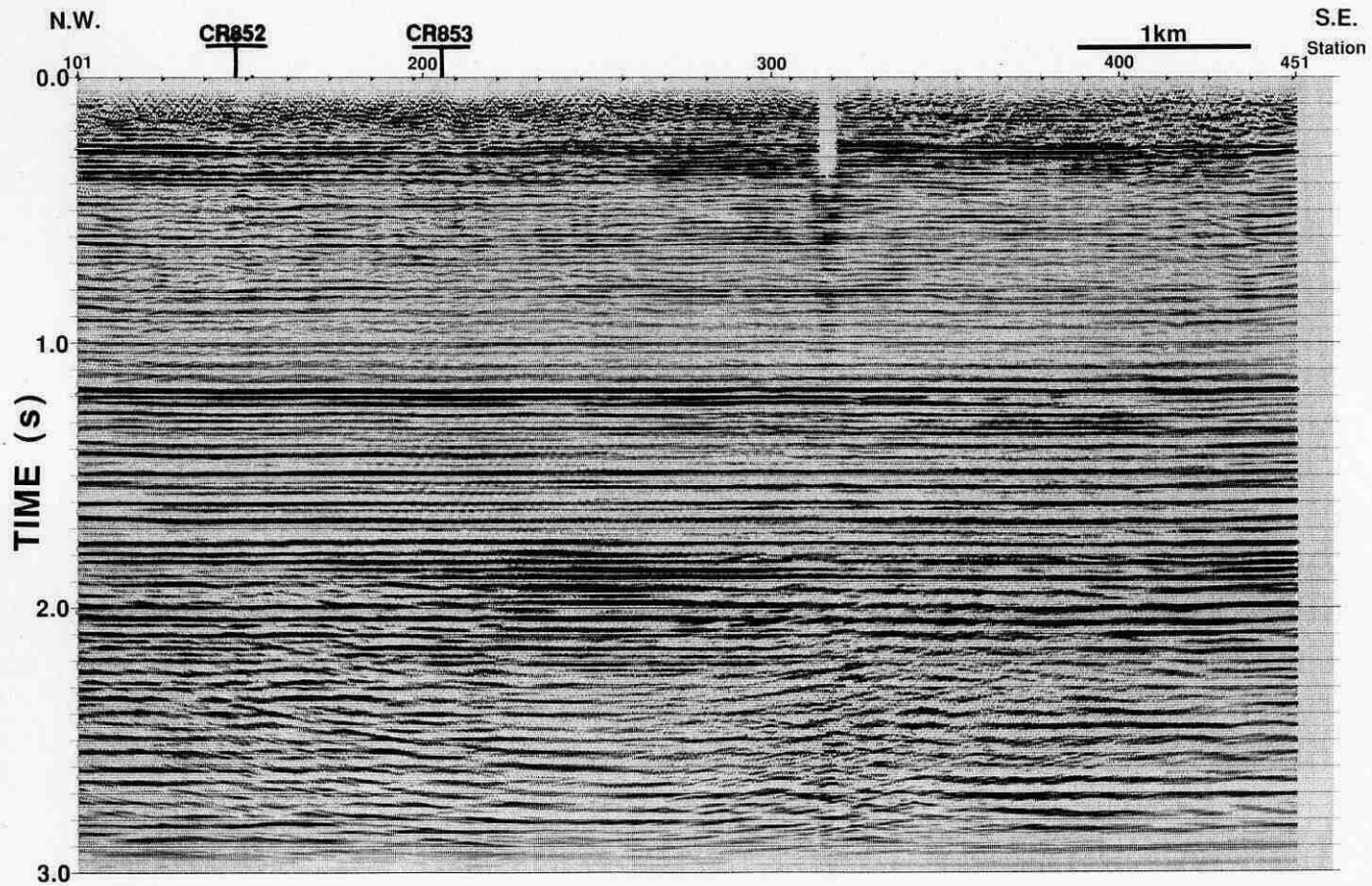


FIG. 3.8. Final migrated stack of line CR851 with an RMS amplitude AGC gain applied.

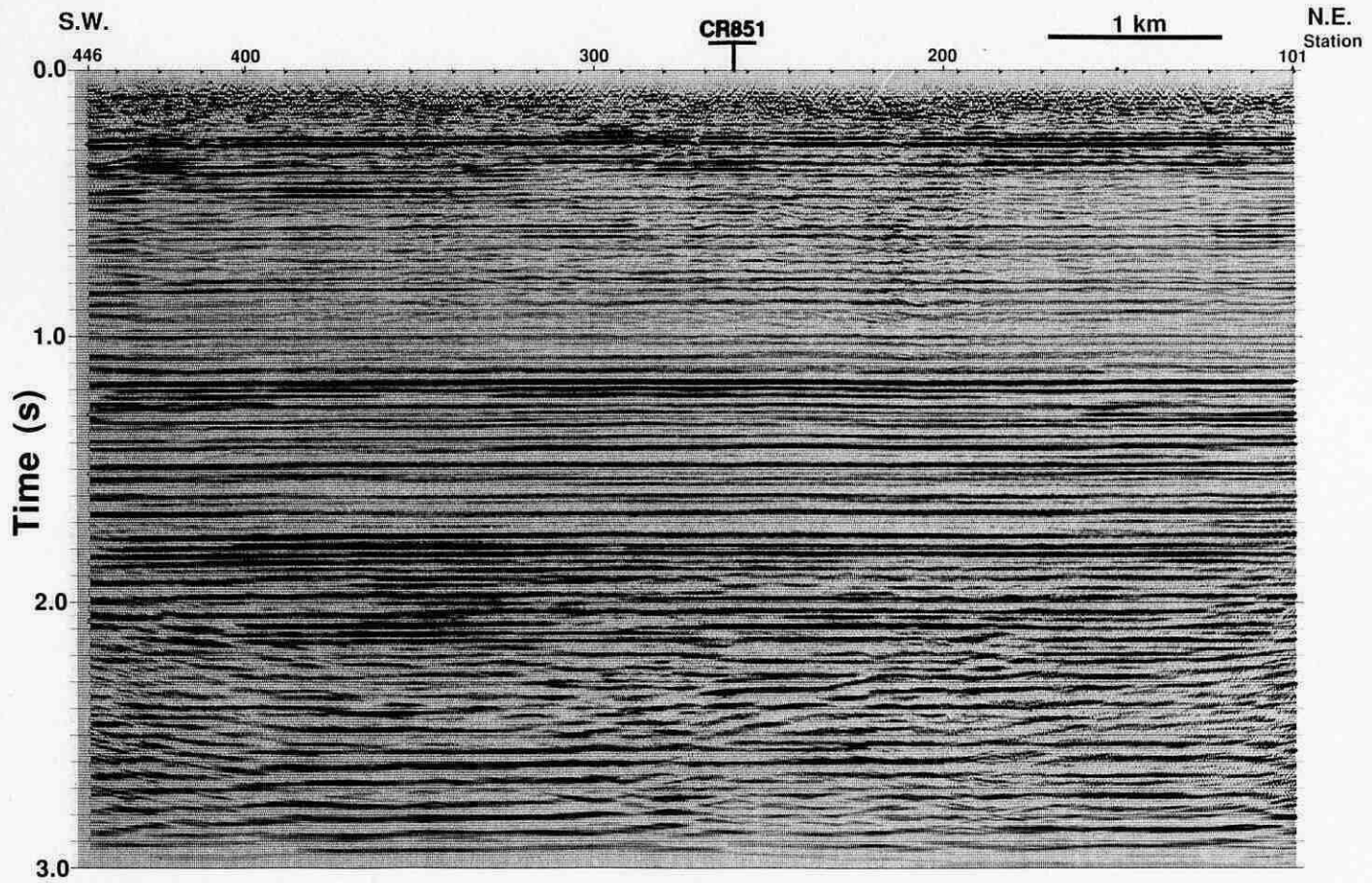


FIG. 3.9. Final migrated stack of line CR852 with an RMS amplitude AGC gain applied.

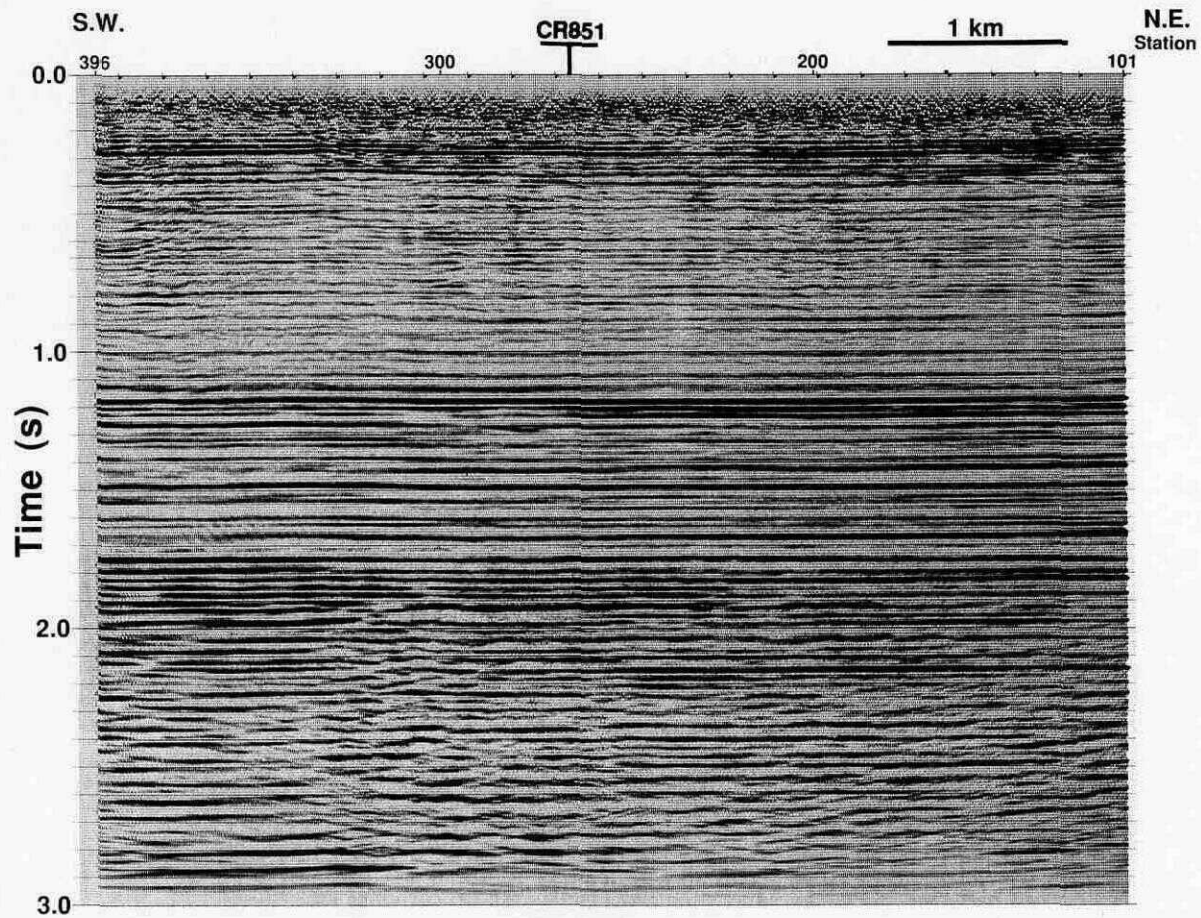


FIG 3.10. Final migrated stack of line CR853 with an RMS amplitude AGC gain applied.

stacked sections is the presence of dipping events at the bottom of the migrated sections (i.e. >2 s). These artifacts are due to overmigration of the later events.

### **3.13 *f-k* Filtering**

The stacked section of Figure 3.7 shows the presence of a significant amount of coherent dipping noise (e.g. at SP 360, 1 s reflection time). This noise can be attributed to refraction multiples, not removed with the mute. Because this coherent noise is usually isolated from the reflected energy in *f-k* (frequency-wavenumber) space their removal was accomplished through the use of an *f-k* dip filter (Yilmaz, 1987).

This filter discriminates on the basis of dip moveout (i.e. velocity) (Sheriff, 1991). Since very little geologic structure is present in the study area, an *f-k* filter was applied removing any dips greater than  $\pm 3$  ms/trace.

## Chapter 4 - DATA PROCESSING (Multicomponent)

### 4.1 Introduction

The three-component geophones used in acquiring the Carrot Creek multicomponent lines recorded particle motion polarized in the vertical, radial and transverse directions. Figure 4.1 shows an example of the data recorded on all three components from a single shot. In addition to the reflected P-wave and converted S-wave energy recorded on the vertical and radial channels respectively, several linear events can be observed. For example, an airwave traveling at 340 m/s is present on the vertical component. Another linear event traveling at 1300 m/s can also be seen on both the radial and transverse components. This low velocity, coupled with the fact that it was not recorded on the vertical channels, suggests that it is a source-generated S-wave refraction possessing both radial and transverse components. Edelmann (1985) showed that such source-generated S-waves from a P-wave vibrator are a common occurrence. The radial component S-wave refraction may also have a contribution from S-waves produced by mode-conversion of P-waves at the base of the weathering layer.

After careful inspection of all records, it was found the transverse component for both multicomponent lines recorded little, if any, reflected energy. This result is not unusual since vertically polarized vibrators were used as the source and hence no transverse particle motion should be present. A significant amount of reflected P- or converted S-wave energy on the transverse component would indicate either the presence of geological structure out of the plane of acquisition or the presence of velocity anisotropy. To help minimize these possibilities, the two multicomponent lines (CCSW01 and CCSW02) were acquired by Boyd Exploration in a direction perpendicular to the regional geologic strike in the Carrot Creek area, which is northwest to southeast (see Figure 2.7). Because this orientation also corresponds to the direction of maximum stress for the region (Bell and Babcock, 1986), it can aid in minimizing any effects of stress-induced anisotropy that are present. Crampin et

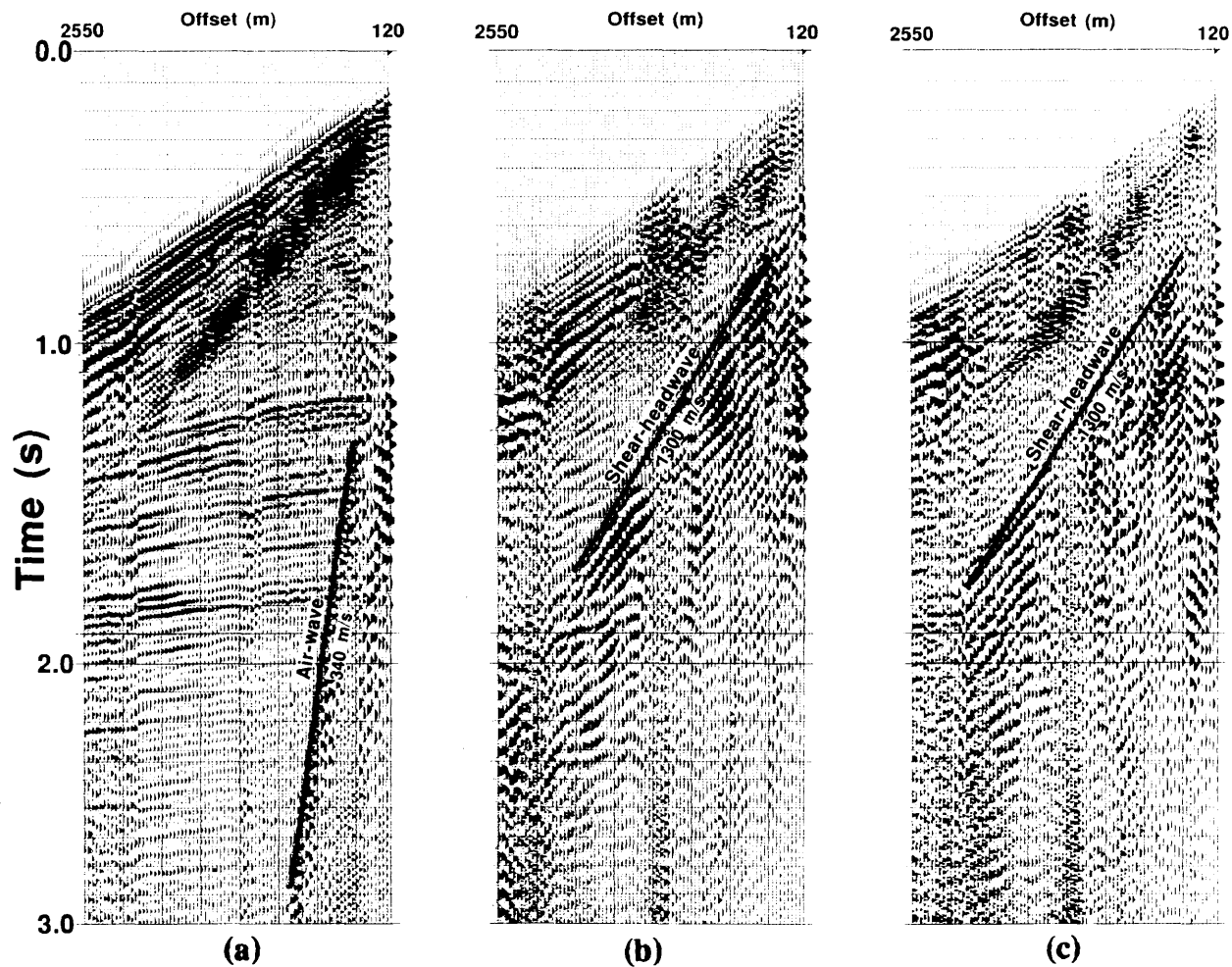


FIG. 4.1. Data recorded in the (a) vertical, (b) radial and (c) transverse direction from shot 27 (source at station 138) of line CCSW02, with an RMS amplitude AGC gain applied.

al. (1984), however, stated that stress-induced anisotropy is seldom a dominant source of anisotropy and would therefore have a minimal effect upon the seismic data. Because of the absence of reflected energy on the transverse component no further processing of this component was undertaken.

The processing of the Carrot Creek multicomponent seismic lines required two individual flows; one for the vertical component and the other for the radial component. The vertical-component processing flow is shown in Figure 4.2 and is essentially identical to that used for the conventional data (Chapter 3), and therefore it will not be discussed further in this chapter.

The asymmetric geometry of the P-SV raypath (Figure 1.1) introduces several problems in P-SV processing that do not arise with conventional P-wave seismic data. The radial-component processing flow followed in this thesis is shown in Figure 4.3. The highlighted portions of this flow represents additional steps required or areas of concern that arise when processing P-SV data. These highlighted portions are described in this chapter.

## **4.2 Reverse Polarity of Trailing Spread**

As discussed in Chapter 2, the Carrot Creek field contains predominantly horizontally layered geology. With very little structural relief being present, converted S-wave energy will arrive at the surface with primarily horizontal polarization, symmetrical about the source (see e.g. Harrison, 1989). Due to this symmetry of the SV-wave particle velocity and the radial geophone sensors being orientated in the same direction along the entire line (Figure 4.4), a reversal in polarity of a P-SV event will occur on opposite sides of the source. Since for processing, the same polarity is required on both sides of the source, the polarity on one side (i.e. trailing spread) was reversed. This was only necessary at the southwest ends of the lines where the source stepped through the receiver spread.

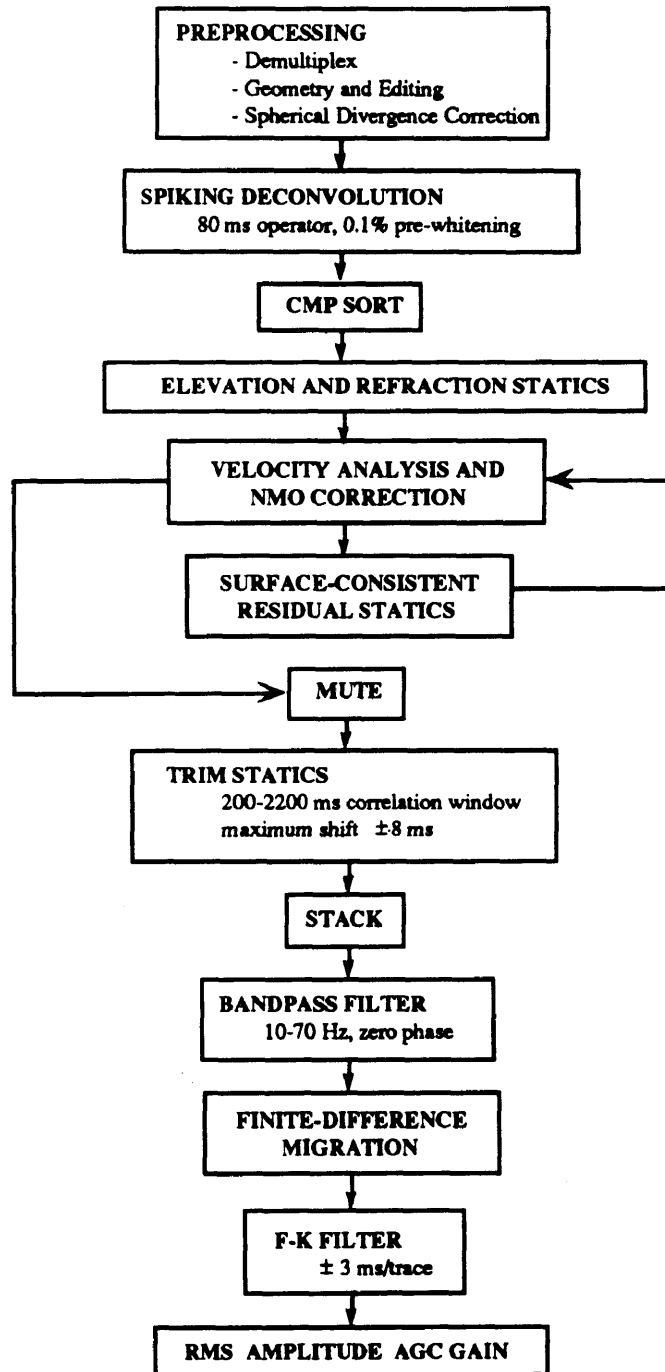


FIG. 4.2. Vertical-component processing flow.

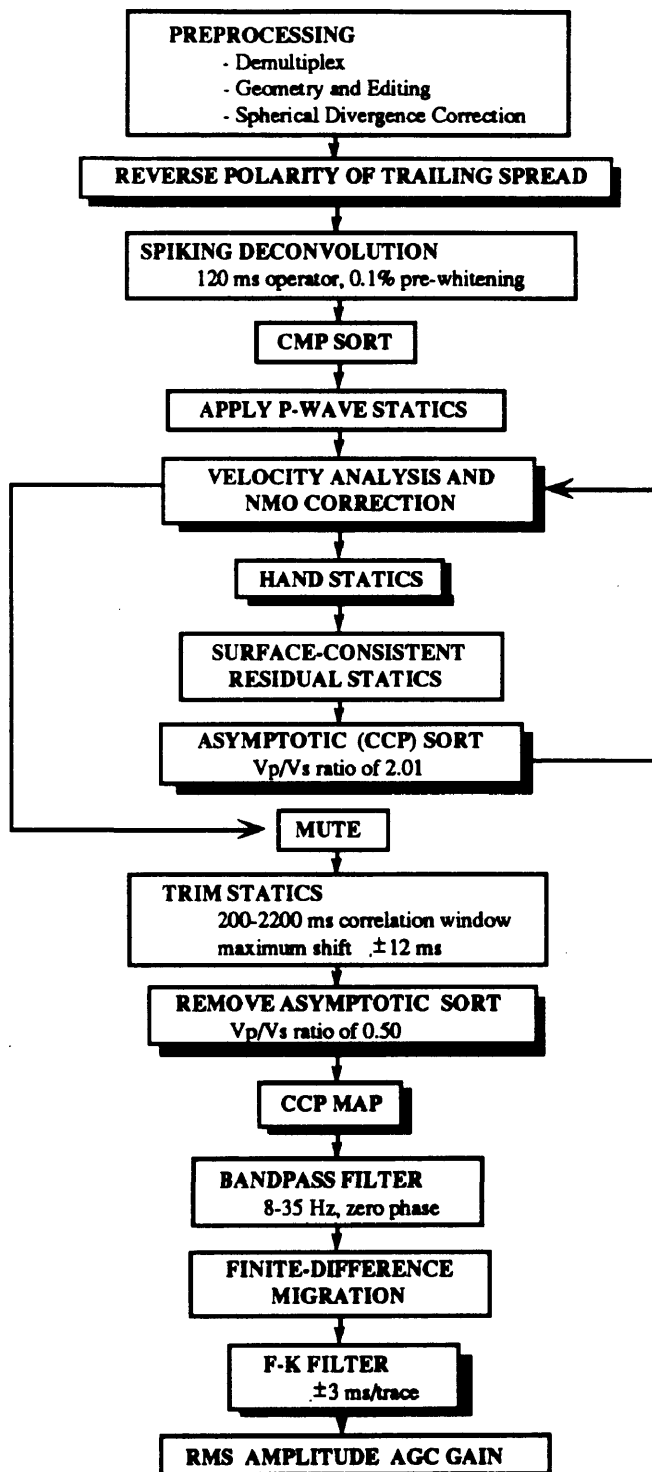


FIG. 4.3. Radial-component processing flow.

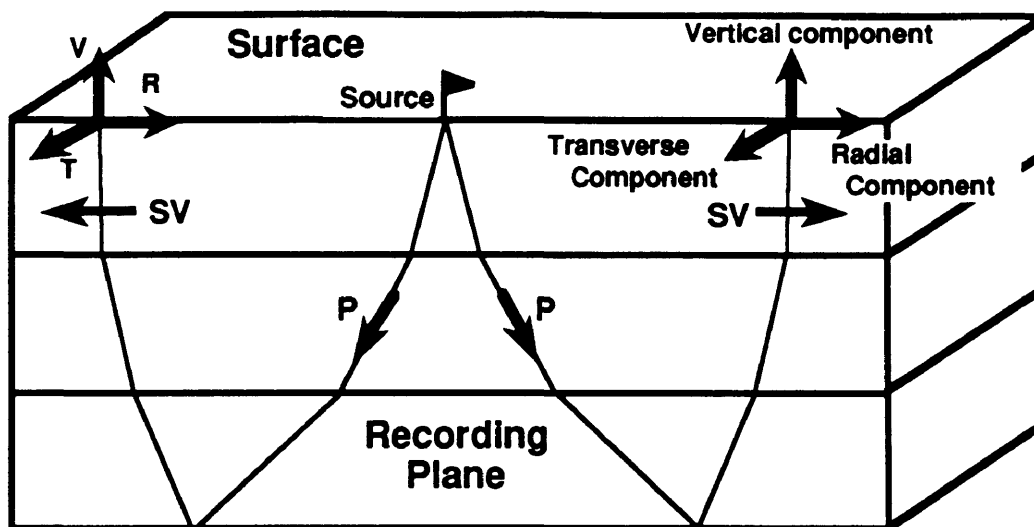


FIG. 4.4. Particle motion and receiver orientation for a P-SV survey.

### 4.3 P-SV Weathering Statics

The static solution for any seismic data set can be divided into two separate parts; a source component and a receiver component, which correspond to traveltimes delays associated with the downgoing and upgoing wavefronts respectively. In the case of conventional seismic data, the static solution (i.e. the sum of the source and receiver statics) can be determined entirely through headwave analysis, as described in Section 3.5. Since the P-SV arrivals have traveled downward through the earth as P-waves, and are influenced by the same surface conditions and delays as the vertical-channel data, the final source-static solution of the P-P data should approximately equal the source-static component of the P-SV data (Harrison, 1989). Due to the effect of the watertable, however, the P-P receiver-statics can only be considered a first-order approximation of the P-SV receiver-statics. The final P-SV receiver-static solution is often much more difficult to determine (Lawton, 1990).

The difficulty in determining the P-SV static solution arises because of two main factors. The downgoing P-waves do not pass through the same thickness of low-velocity weathering layer as the upgoing SV-waves. This discrepancy is due to the P-wave velocity increasing below the watertable whereas the S-wave velocity does not (i.e. S-waves are

essentially insensitive to fluid saturation). The watertable thus has the effect of thinning the weathering layer for P-waves (Lawton, 1990), and resulting in the S-waves traveling through an apparently much thicker, low-velocity layer. These large S-wave statics can be seen on the radial-component record of Figure 4.1. The second difficulty in determining the P-SV receiver-statics (i.e. S-wave statics) arises from the difficulty in undertaking S-headwave analysis. The problem arises in picking the S-headwave, due to low amplitudes and interference from P-wave multiple refractions (Lawton, 1990). Unfortunately, this problem is present with the Carrot Creek data set and therefore the P-SV receiver-statics had to be determined through the use of a common-receiver stack.

Figure 4.5 shows both common-source and common-receiver stacks of the radial component (P-SV) data from line CCSW02, with the final P-P source and receiver statics applied. As predicted, the common-receiver stack of Figure 4.5 indicates that the P-P source-static solution has in fact corrected most of the P-SV source-statics. The common-receiver stack, on the other hand, indicates the presence of significant residual S-wave statics. These residual statics, for line CCSW02, are as large as 120 ms. Similar residual statics were also observed for line CCSW01; their size is however significantly smaller, the largest being 60 ms. To remove these static shifts, the receiver-statics were picked by hand from the common-receiver stack and applied to the data. Any remaining statics were then removed later in the processing flow using the residual statics procedure discussed in Section 3.7.

#### **4.4 NMO Correction**

Another concern in P-SV processing is the correction for normal moveout. Although the standard hyperbolic NMO equation (eq. 3.3) is a good approximation for unimodal seismic data (i.e. P-P or S-S), Slotboom et al. (1990) showed that P-SV moveout could be better approximated by a time-shifted hyperbola;

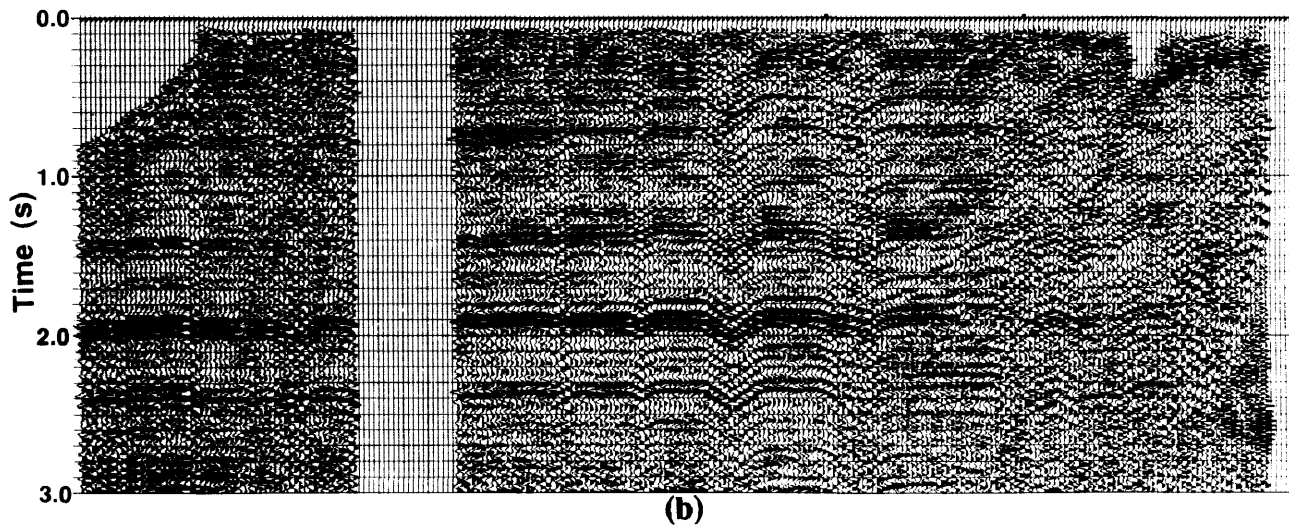
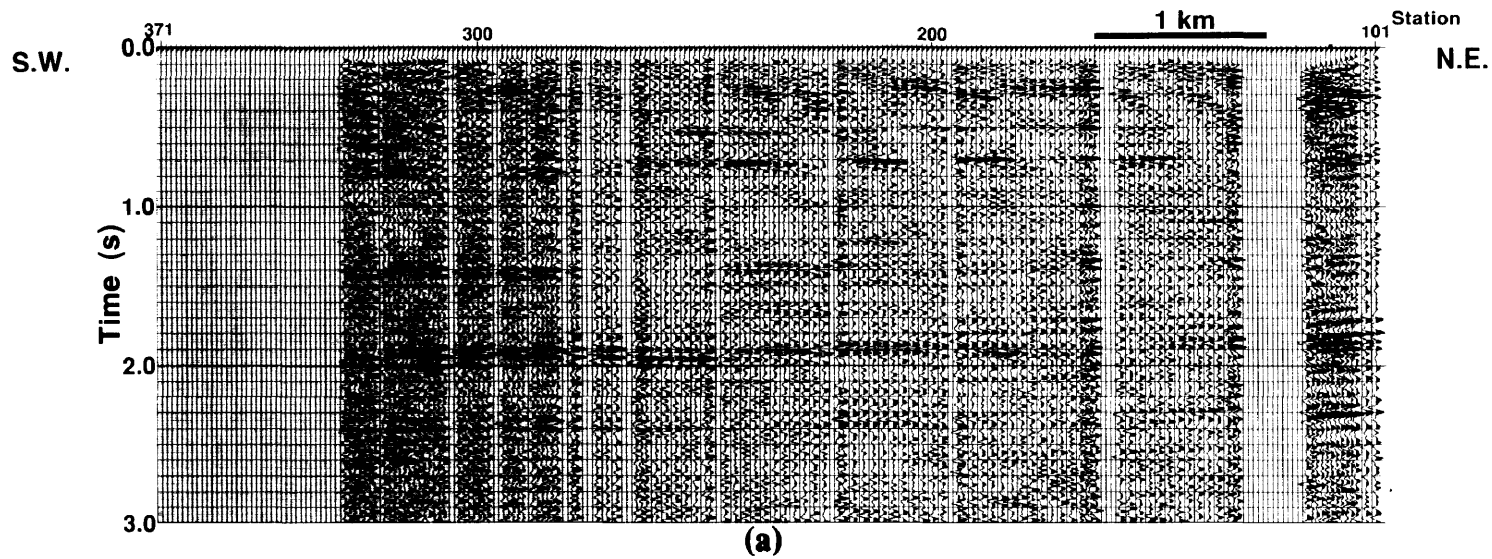


FIG. 4.5. (a) Common-source and (b) common-receiver stacks of the P-SV (radial component) data of line CCSW02 with the P-P source- and receiver-statics applied. Note the large static shifts present on the common-receiver stack, but lacking on the common-source stack.

$$t = \frac{t_0}{2} + \sqrt{\frac{t_0^2}{4} + \frac{X^2}{2V_{rms}^2}}, \quad (4.1)$$

where  $t$  is the offset travel-time,  $t_0$  is the “zero-offset” P-SV travel-time,  $X$  is the source-receiver offset and  $V_{rms}$  is the P-SV rms-velocity. The P-SV  $V_{rms}$  is given by the following equation;

$$V_{rms}^2 = \frac{\sum_{i=1}^N (V_{pi}^2 t_{pi} + V_{si}^2 t_{si})}{\sum_{i=1}^N (t_{pi} + t_{si})} \quad (4.2)$$

where  $t_{pi}$  and  $t_{si}$  are the P-wave and S-wave interval transit times for a specific interval  $i$ , possessing P- and S-wave velocities of  $V_{pi}$  and  $V_{si}$  respectively. Iverson et al. (1989) showed using equation 4.2 the velocity for any interval ( $V_i$ ) is given by:

$$V_i^2 = V_{pi} V_{si}. \quad (4.3)$$

In order to test the effectiveness of this improved NMO equation, two synthetic P-SV common-offset gathers were generated (Figure 4.6), using the same geometry as the field data (i.e. far-offset of 2550 m), and NMO-corrected using both the conventional and "Slotboom" NMO equations. The same front-end mute as used on the field data was also applied. These common-offset gathers were generated from the P-wave sonic log of well 1-3-53-13W5, assuming  $V_p/V_s$  to be 2.0 and using the technique discussed by Howell et al. (1991). These gathers show that only a slight overcorrection can be observed on the conventionally NMO-corrected gather as opposed to the Slotboom-corrected gather; i.e. the mute has removed most of the overcorrected data of the conventionally NMO-corrected gather. Since, when the mute is applied, only a small difference can be observed in the effectiveness of the two NMO equations, the conventional NMO equation was used. Common-offset gathers of the vertical and radial components of line CCSW02, which have both been NMO-corrected using the conventional NMO equation, are shown in Figure 4.7. As predicted, this figure shows that

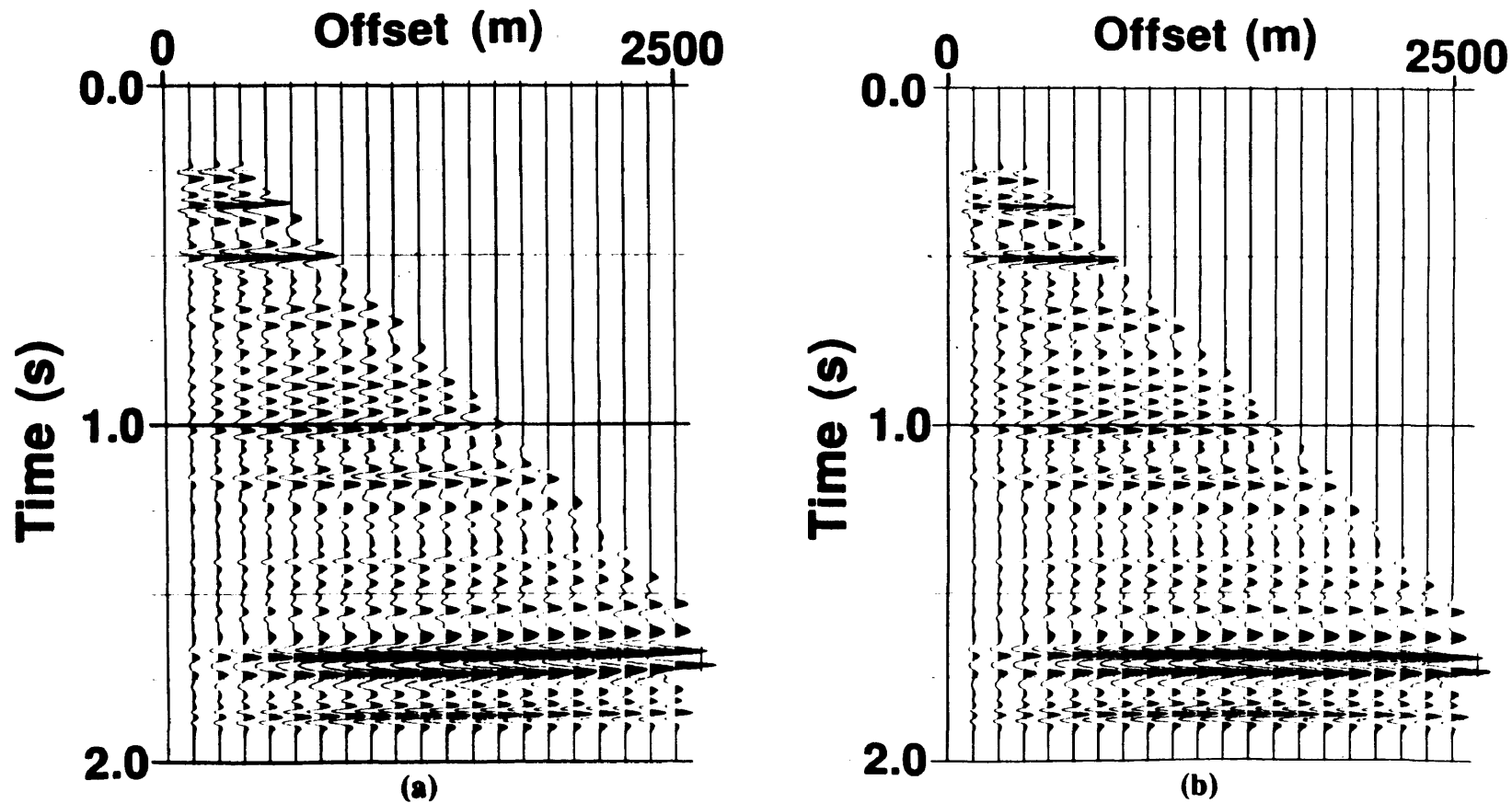


FIG. 4.6. Synthetic P-SV common-offset gathers (generated from the P-wave sonic of well 1-3-53-13W5) NMO-corrected using the (a) conventional and (b) "Slotboom" NMO equations. The same mute as applied to the field data was also applied.

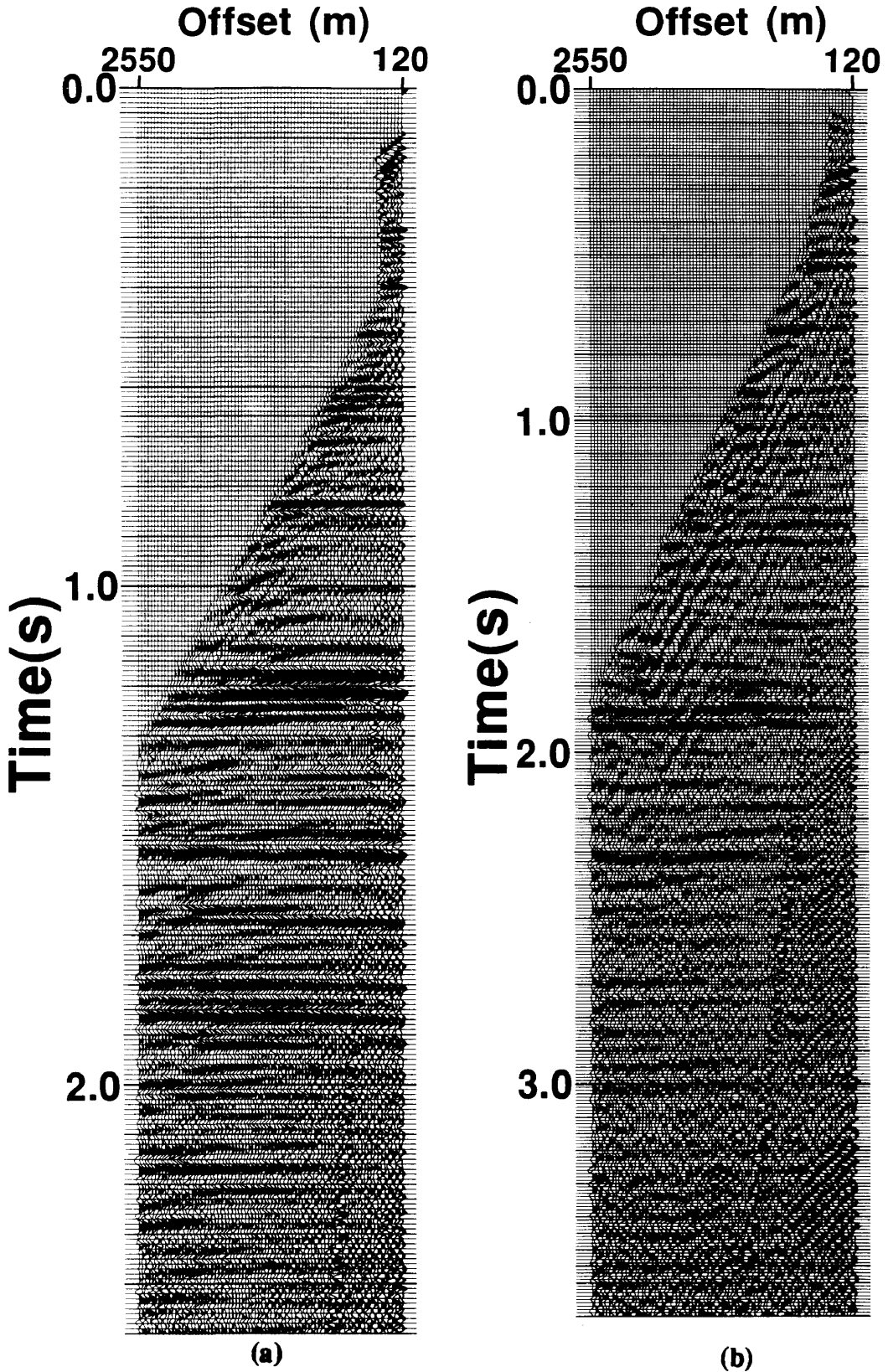


FIG. 4.7. (a) Vertical and (b) radial common-offset gathers from station 320 of line CCSW02, NMO corrected using the standard moveout equation (eq. 3.3).

both components are sufficiently flattened using the conventional moveout correction.

Examples of the velocity spectra from the vertical and radial components of line CCSW02, are shown in Figure 4.8, along with their respective velocity functions. This figure shows that both the P-P and P-SV velocity function are very similar except the P-SV velocities are approximately 70% of the P-P velocities. The final velocity functions, utilized for the vertical and radial component of lines CCSW01 and CCSW02, are all listed in Appendix A.

## **4.5 Common Conversion-point Sort**

Due to the asymmetric raypaths of converted-wave seismic data, conventional midpoint gathering, as discussed in Section 3.4, could not be used. Figure 4.9 shows that the conversion-point is offset from the source-receiver midpoint and is depth-variant, reaching an asymptotic value when the reflection depths are much greater than the source-receiver offset. Eaton et al. (1990) identifies three methods for the sorting of converted-wave data: sorting using an asymptotic approximation (Fromm et al., 1985), sorting using a straight raypath approximation (Tessmer and Behle, 1988) and depth-variant mapping. In the processing of the Carrot Creek radial-component data, both the asymptotic and depth-variant techniques were implemented.

### **4.5.1 Asymptotic Sort and Stack**

This technique is analogous to the CMP sort except that the data are gathered according to the asymptotic value of the conversion-point trajectory (Figure 4.9), not the source-receiver midpoint (Slotboom and Lawton, 1989). The position of the asymptote is determined using the following formula, derived by Fromm et al. (1985);

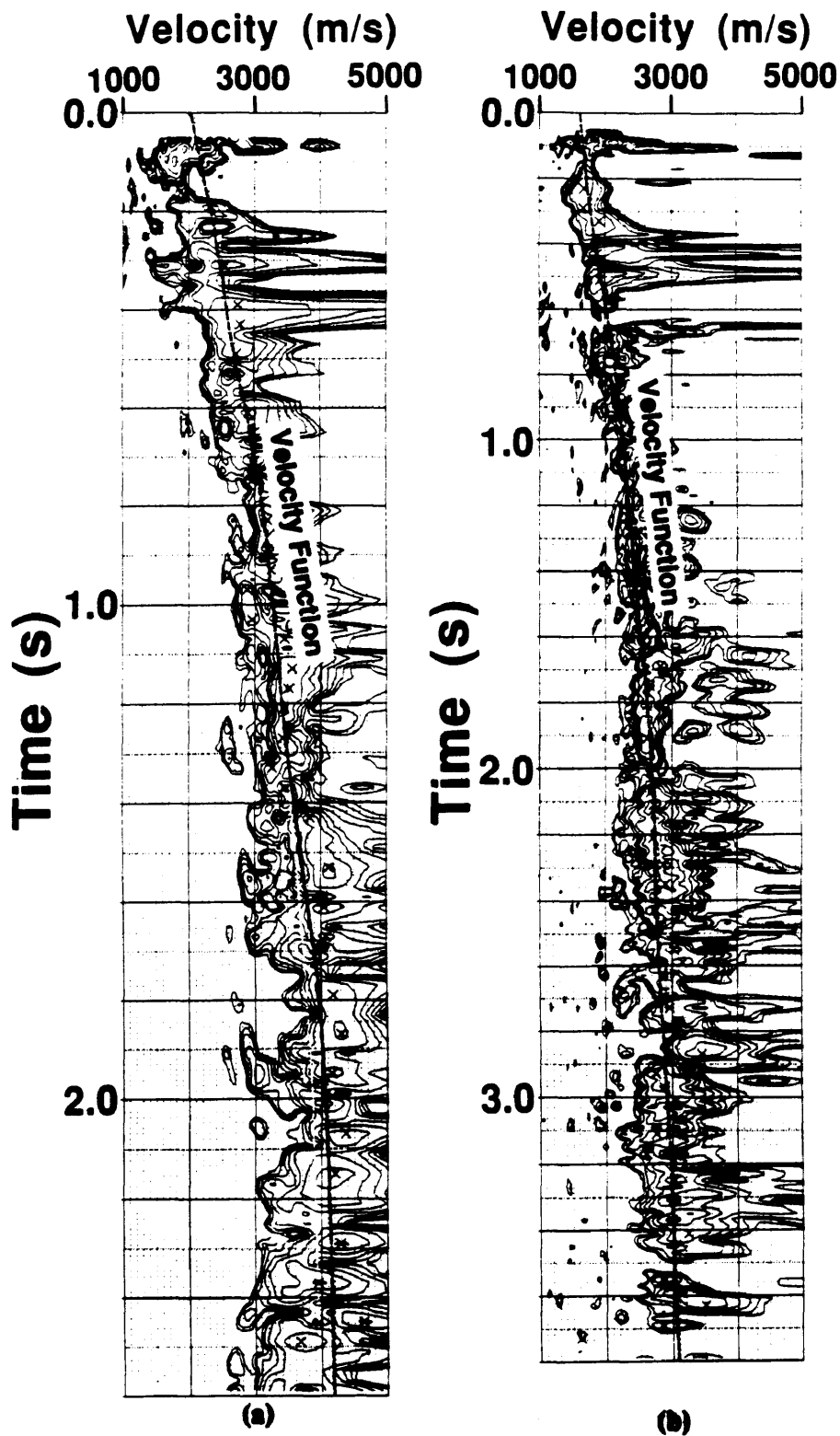


FIG. 4.8. Velocity spectra of the (a) P-P and (b) P-SV data of station 320 of line CCSW02. The velocity functions based upon maximum semblance are also shown.

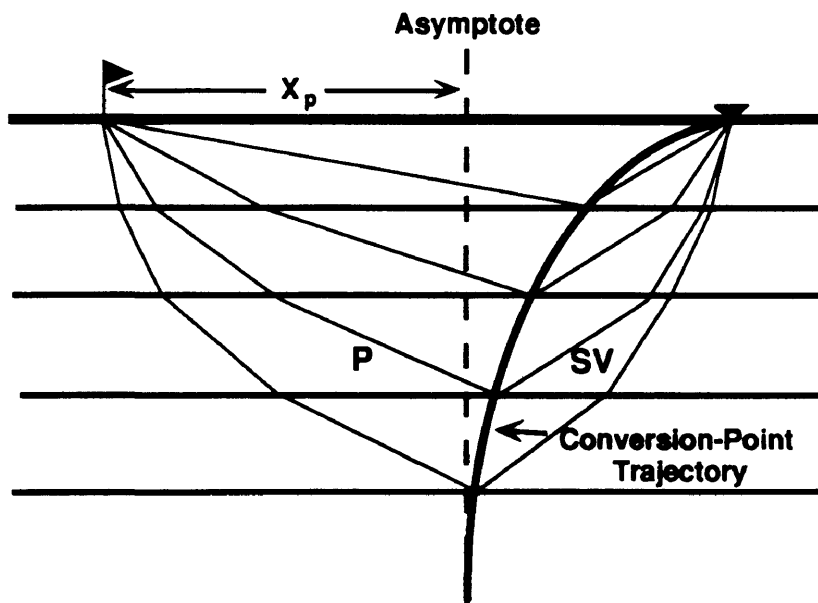


FIG. 4.9. Raypath geometry for P-SV data (after Slotboom and Lawton, 1989).

$$X_p = \frac{X}{1 + \left[\frac{V_p}{V_s}\right]^{-1}}, \quad (4.4)$$

where  $X_p$  is the offset of the conversion-point asymptote from the source,  $X$  is the source-receiver offset and  $V_p/V_s$  is the average compressional-to-shear wave velocity ratio for the area. For the processing of the Carrot Creek data, the value of  $V_p/V_s$  to use in equation 4.4 was determined by correlating the final vertical-component stack and a CMP-sorted brute stack of the radial component. Using the procedure that is discussed in Chapter 5 (Section 5.2),  $V_p/V_s$  for specific seismic intervals were determined. Using these calculated interval  $V_p/V_s$  values, and weighting them by their respective P-SV isochron, an average  $V_p/V_s$  down to each event was calculated; these values are listed in Chapter 5 (Table 5.2). Since the zone of interest for the area is the Cardium Formation (P-P travel time of 1000 ms) the average  $V_p/V_s$  down to this event (i.e. 2.0) was used in equation 4.4.

Because the asymptotic sorting technique does not take into consideration variation of the conversion-point with depth, several undesirable effects on the final stack section arise.

The most prominent effect is the smearing of events that do not have their conversion-points corresponding to the location of the asymptote (Slotboom and Lawton, 1989). Eaton and Lawton (1991) also showed that fluctuations in amplitude and character can arise with asymptotic sorting due to periodic variations in trace multiplicity and offset range in adjacent CCP bins. The use of depth-variant mapping could in turn remove these problems. Unfortunately, the depth-variant mapping program available could only output a stack section and not CCP gathers. Since gathers could not be output, the final static solution had to be first determined using asymptotically sorted data. Once the final static solution was determined, the data were then re-sorted back to CMPs, using a  $V_p/V_s$  of 0.5, to allow for the application of depth-variant mapping.

#### 4.5.2 Depth-variant (CCP) Mapping

Unlike the asymptotic sort, which shifts the entire trace to the asymptote position, depth-variant mapping repositions each sample to its proper location along the conversion-point trajectory (Figure 4.9). This procedure is analogous to the VSPCDP map used with offset VSP data (Wyatt and Wyatt, 1984).

The mapping algorithm utilized for this thesis, developed by Eaton et al. (1990), determines the conversion-point location for each sample by raytracing through a velocity model and then stacking the data. The model used was based upon the P-wave interval time and the respective  $V_p/V_s$  values obtained by the interval-time analysis discussed in Chapter 5. The final vertical-component (P-P) and radial-component (P-SV) sections of lines CCSW01 and CCSW02 are shown in Figure 4.10 through 4.13 respectively, plotted using the Aki and Richards (1980) polarity convention. Since  $V_p/V_s$  for most rock types is around 2.0 (Tatham, 1985), the P-SV data were plotted at two-thirds the P-P time scale to allow for easier correlation between the P-P and P-SV sections. As with the vertical-component (P-P) data, the radial-component (P-SV) data were migrated using a finite-difference migration tech-

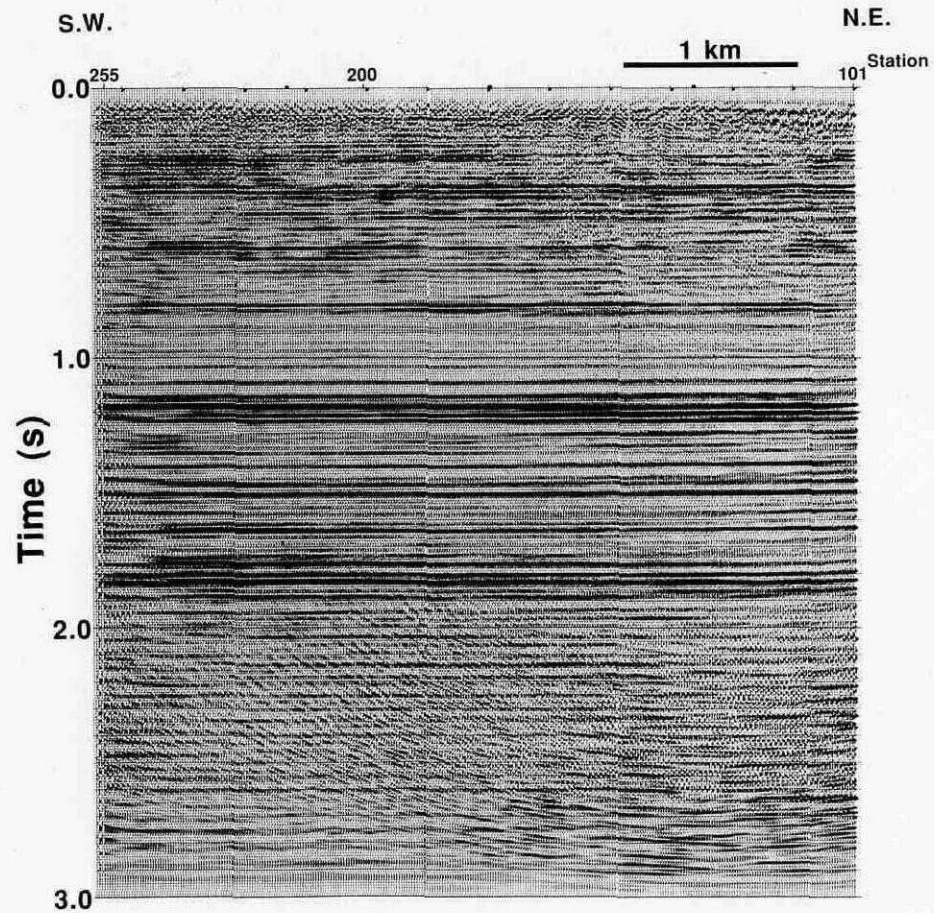


FIG. 4.10. Final vertical-component migrated section from line CCSW01 (RMS amplitude AGC gain applied).

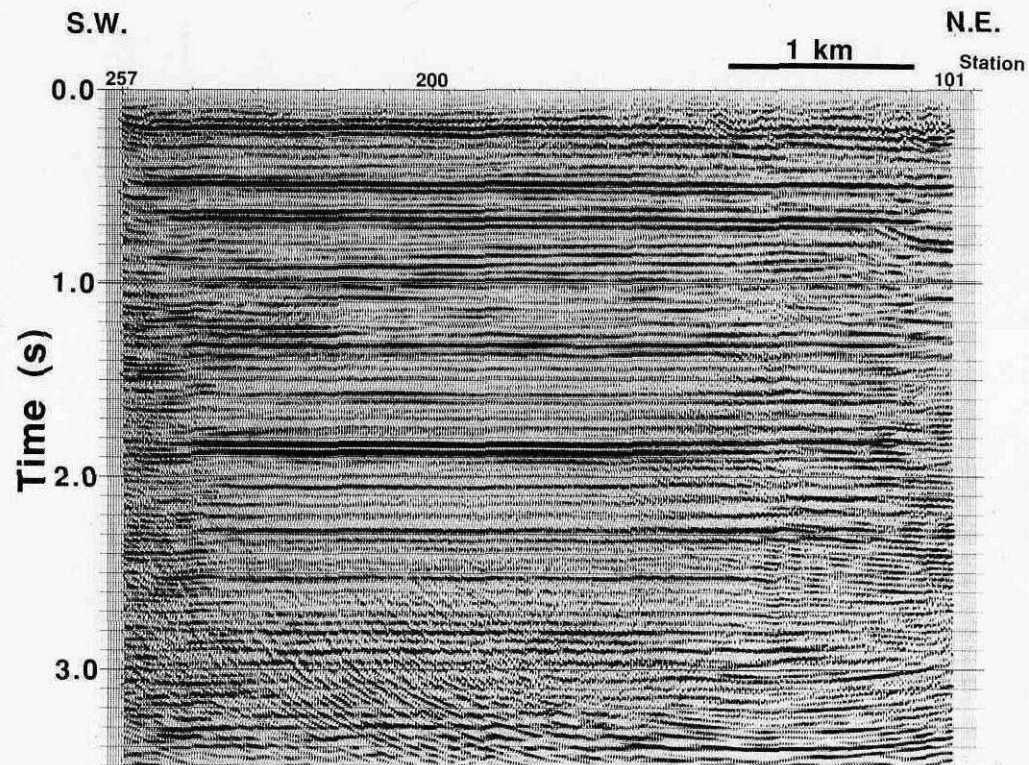


FIG. 4.11. Final radial-component migrated section from line CCSW01 (RMS amplitude AGC gain applied).

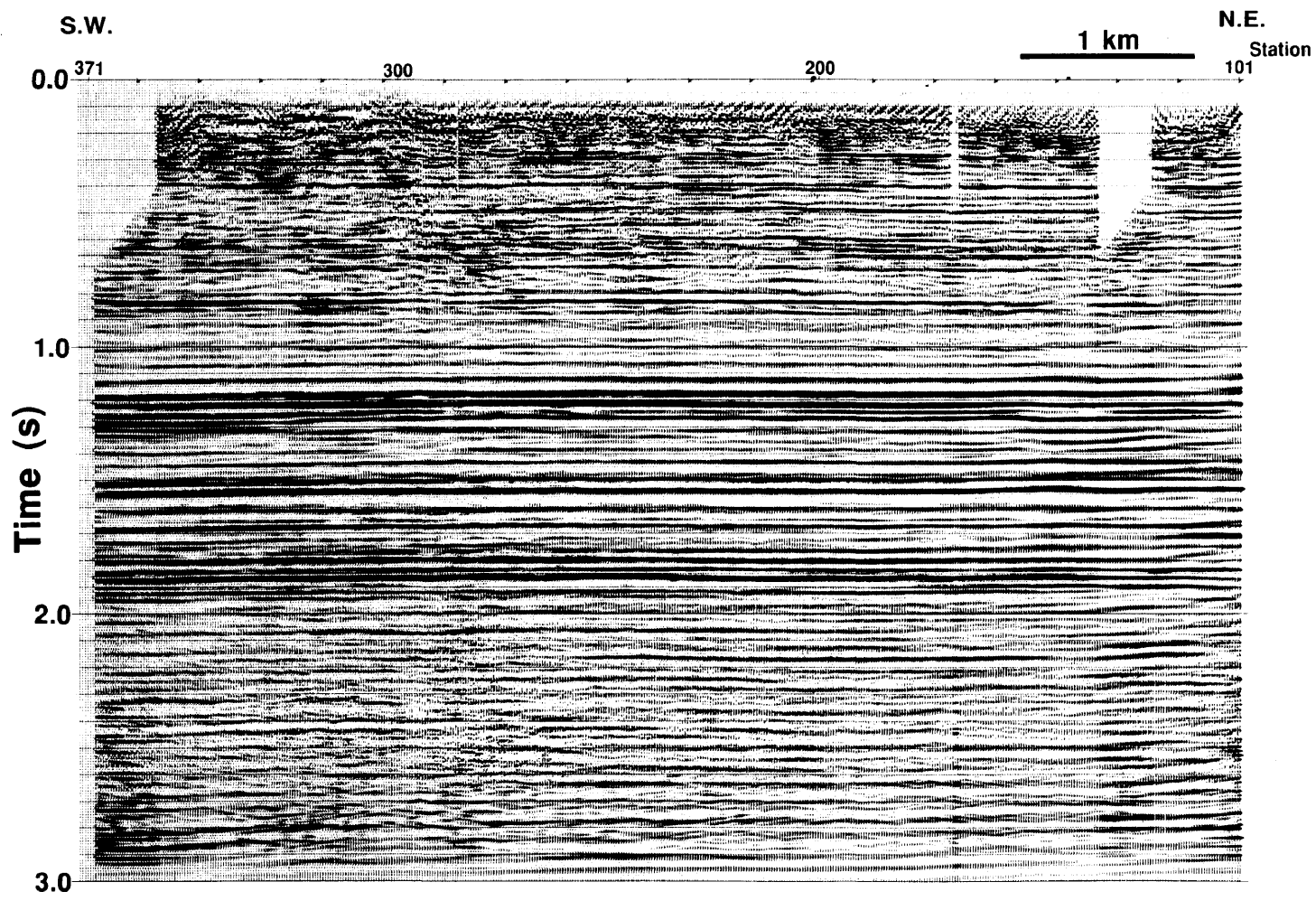


FIG. 4.12. Final vertical-component migrated section from line CCSW02 (RMS amplitude AGC gain applied).

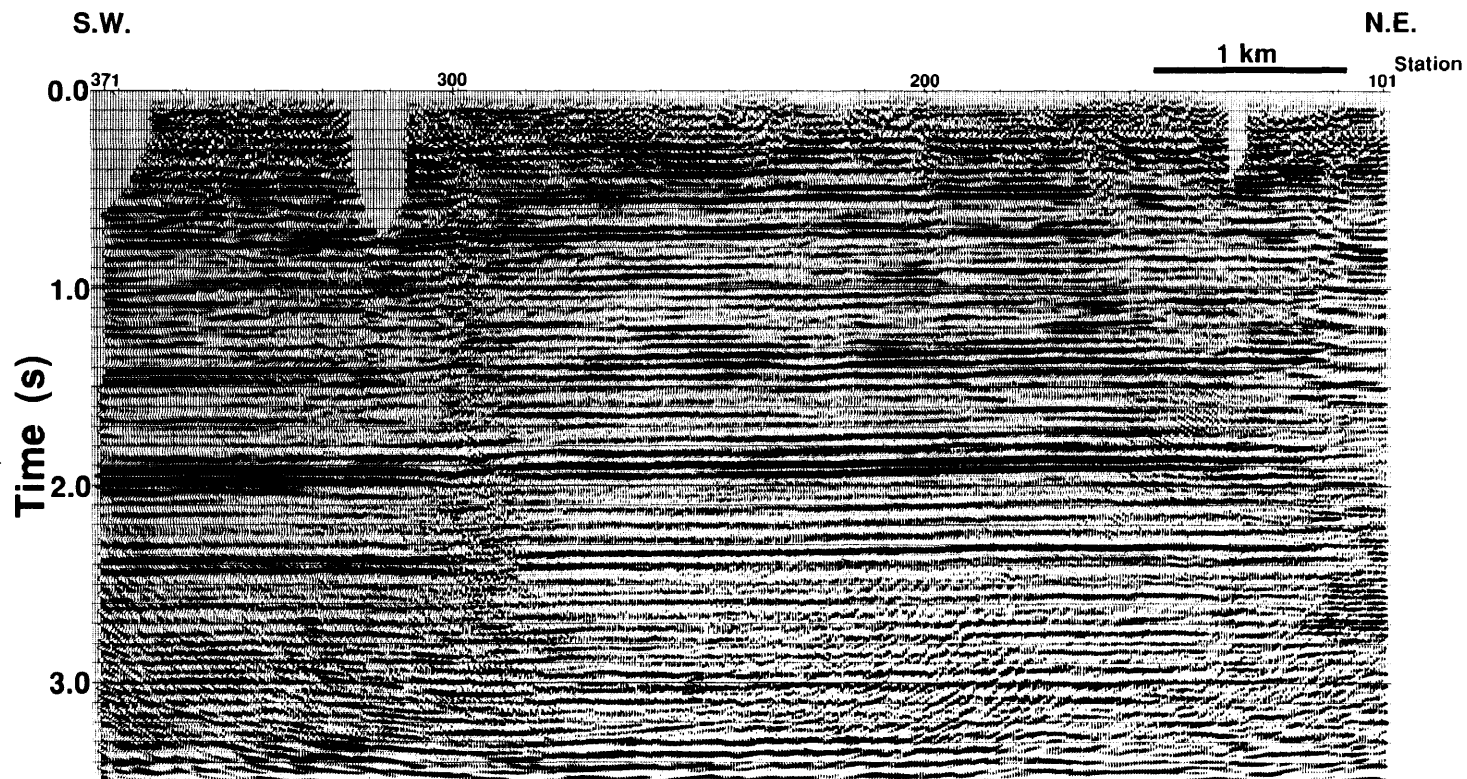


FIG. 4.13. Final radial-component migrated section from line CCSW02 (RMS amplitude AGC gain applied).

nique. Unlike the P-P data, however, the P-SV migration velocities do not correspond to the rms-velocities. Harrison (1991) showed that the Carrot Creek P-SV migration velocities are on average 9% lower than the rms-velocity. Since the reflection events of the Carrot Creek data set are flat-lying this difference between the rms- and migration-velocities on the final migrated sections was found to make little difference on the final stacked section. For convenience, the rms-velocity function was therefore used.

## 4.6 Discussion

Although the final sections for all the conventional and multicomponent lines possess relatively high signal-to-noise ratios, several differences can be observed between them. For example, there appears to be a slight difference in character between the conventional (Figures 3.8 to 3.10) and vertical-component (Figures 4.10 and 4.12) data. This difference can be attributed to two factors:

- i) Since the conventional and multicomponent lines were not acquired in the same locations, the geology, and therefore seismic parameters, may be slightly different.
- ii) The use of different types of sources (i.e. dynamite for the conventional data and vibrators for the multicomponent data) as well as different recording instruments could produce differences in phase of the reflections between the lines. Often when such differences are present the data is phase-rotated to produce a better match. This was not done in this case since only a slight difference in character is observed between the lines.

Differences can also be observed between the final sections from the processed multicomponent data set (Figures 4.10 to 4.13).

- i) The data from line CCSW01 (Figure 4.10 and 4.11) generally has a slightly higher signal-to-noise ratio than the data from line CCSW02 (Figure 4.12 and 4.13). This difference can be observed when comparing the radial-component stacks (Figures

4.11 and 4.13).

ii) The vertical-component data exhibit a significantly higher signal-to-noise ratio than the radial-component data.

The slightly lower signal-to-noise ratio of the data from line CCSW02 (Figure 4.12 and 4.13) is a result of a combination of low fold, due to occasional large gaps between shots, and the presence of several oil wells along the line which are thought to have attributed additional noise into the final sections. The significant decrease in coherency of the radial-component events of line CCSW02 (Figure 4.13) arises primarily from the considerably higher magnitude of the S-wave statics located along line CCSW02 (Figure 4.5). These larger statics indicate a thicker weathering layer which will also result in a greater attenuation of the reflection signal (McCormack and Tatham, 1986).

The stronger vertical-component response arises partially because vertically polarized vibrators were used as the source. The amplitude of the radial component is therefore dependent upon the amount of P-SV conversion that occurs. For example, the low signal-to-noise ratio observed at the end of the radial-component section of line CCSW01 (Figure 4.12) is due to small angles of incidence, therefore producing little P-SV conversion and poor data quality. In addition, the P-SV data has a lower signal-to-noise ratio due to the greater attenuation of the converted S-wave in the near-surface weathering layer.

## Chapter 5 - INTERPRETATION

### 5.1 Introduction

This chapter discusses the assumptions made and techniques used in interpreting the surface seismic data of the Carrot Creek field. Much of the interpretation is based upon the representative geologic model of the field, discussed in Section 5.2. Using seismic parameters defined in this model, forward seismic modeling was undertaken on selected horizons for both the vertical (P-P) and radial (P-SV) component case (Section 5.3). Analyses of both lateral and vertical variations of interval  $V_p/V_s$  values, determined from the stacked/migrated seismic sections, were also undertaken; these results are summarized in Section 5.2 and 5.4, respectively. Incorporating all these results, Section 5.5 then discusses and interprets the seismic response observed in the Carrot Creek field.

### 5.2 Geologic Model

The geologic model used to represent the Carrot Creek field is shown in Figure 5.1. It is based upon well-log and core data, and the following seismic interpretations. The model layers were horizontal, as this is a close approximation to the long wavelength geology of the area. The velocities, Poisson's ratios, and densities for each layer are summarized in Table 5.1. Geologic markers, corresponding to seismic events identified on the seismic sections, were used to make up the model's layers. These markers were identified on the P-wave seismic sections by correlating the processed seismic data with synthetic seismograms generated from P-wave sonic logs found in the area (Figure 5.2). Figures 5.3 through 5.7 show the migrated stacks of the P-wave seismic data, with and without the interpreted events.

Due to the lack of a complete full-waveform sonic or an offset VSP, events on the P-SV (radial-component) stacks were identified by visually correlating each radial-component stack with its respective vertical-component stack, as illustrated in Figure 5.8. To aid in the

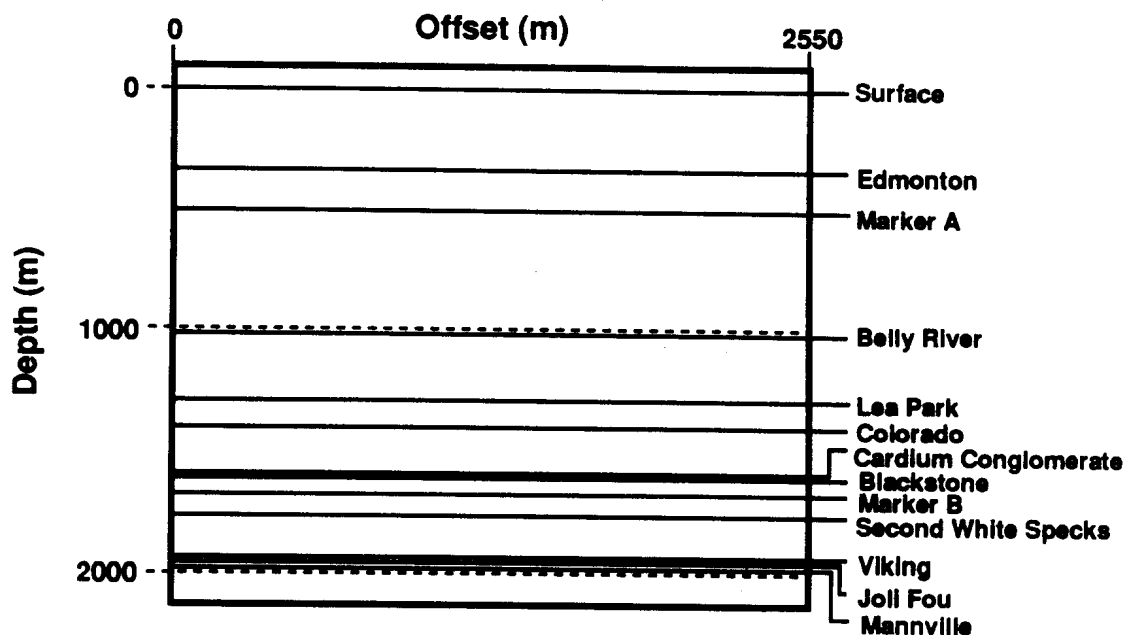


FIG. 5.1. Geometry of the Carrot Creek geologic model.

Table 5.1. Carrot Creek model parameters.

Geologic Marker	Depth (m)	Thickness (m)	$V_p$ (m/s)	$V_s$ (m/s)	$V_p/V_s$	Poisson's Ratio	Density (Mg/m <sup>3</sup> )
Surface	0	355	2800	1044	2.68	0.42	2.37
Edmonton	355	200	3226	1453	2.22	0.37	2.37
Marker A	555	470	3200	1517	2.11	0.36	2.37
Belly River	1025	290	4150	2268	1.83	0.29	2.45
Lea Park	1315	117	3650	1780	2.05	0.34	2.50
Colorado	1432	173-188	3920	2031	1.93	0.31	2.38
Cardium (congl.)	1605-1620	5-20	4327	2591-2704	1.60-1.67	0.18-0.22	2.61
Blackstone	1625	65	4003	2074	1.93	0.31	2.51
Marker B	1690	85	3900	2308	1.80	0.25	2.55
Second White Specks	1775	150	3600	2081	1.73	0.25	2.45
Viking	1925	33	4400	2543	1.73	0.25	2.60
Joli Fou	1958	14	3800	2197	1.73	0.25	2.30
Mannville	1972	-	4200	2428	1.73	0.25	2.60

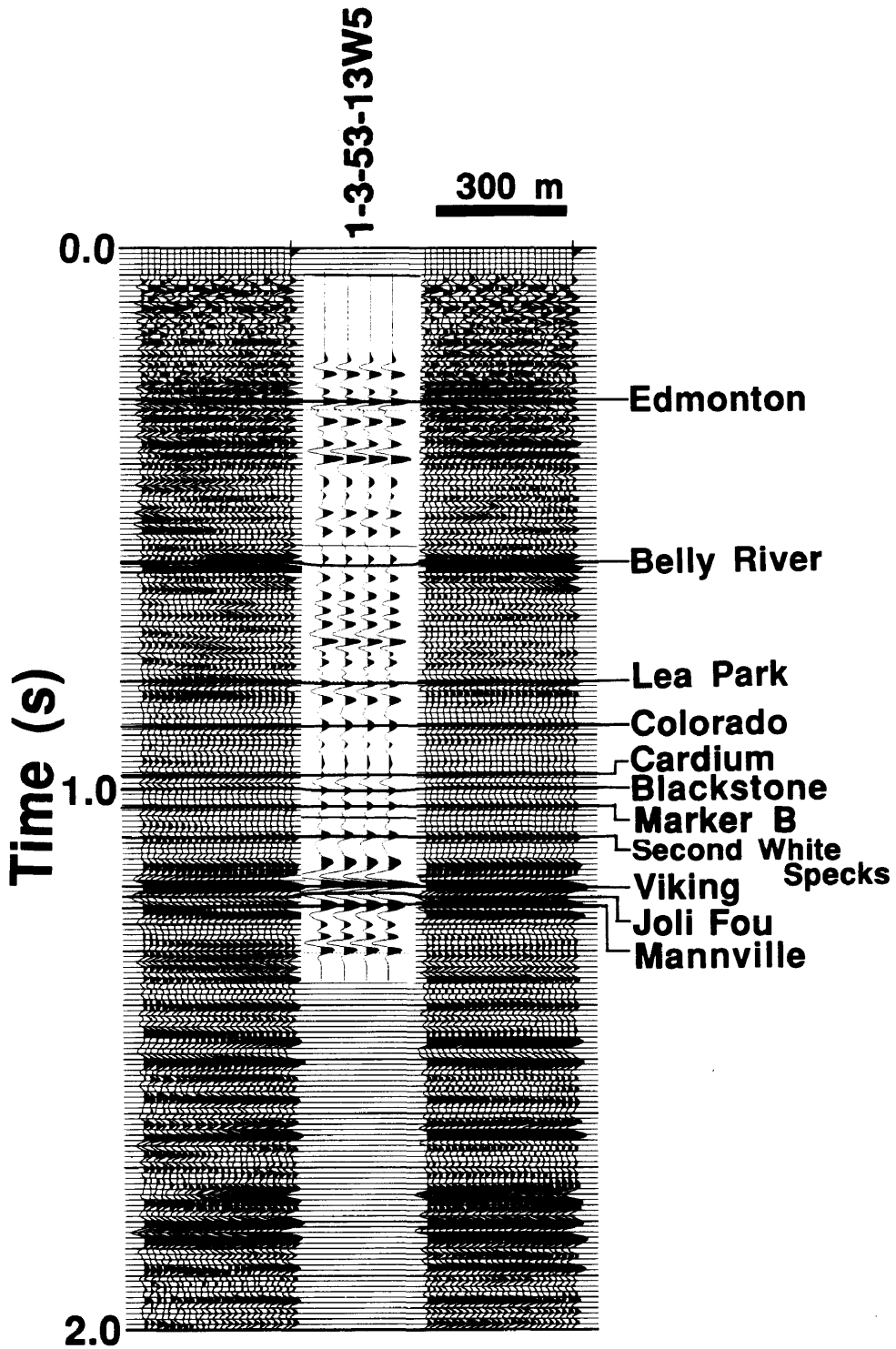


FIG. 5.2. Identification of events on the vertical component of line CCSW01 using a synthetic seismogram generated from the sonic log of well 1-3-53-13W5.

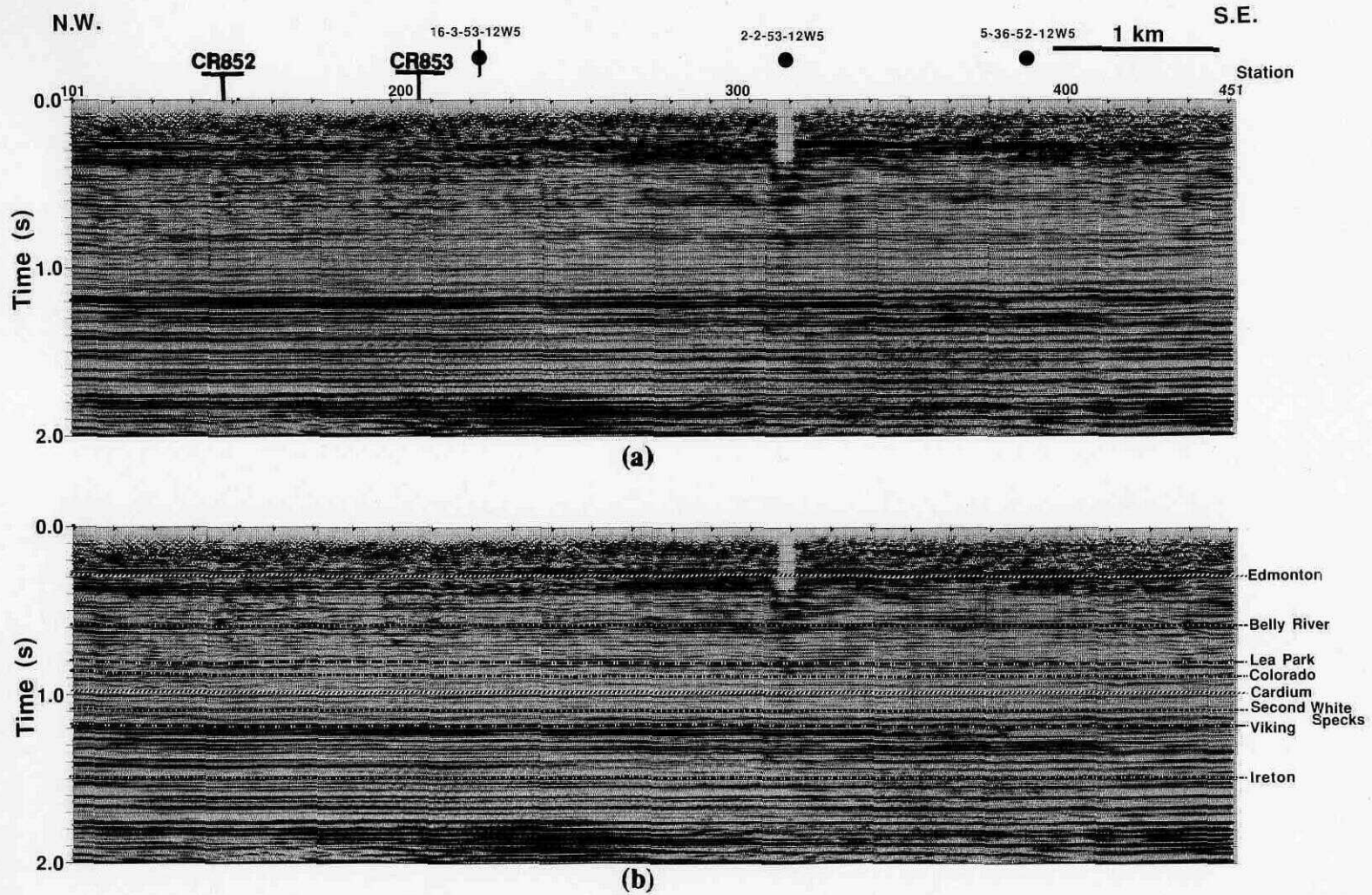


FIG. 5.3. Final migrated stack of line CR851 (a) without and (b) with interpreted events.

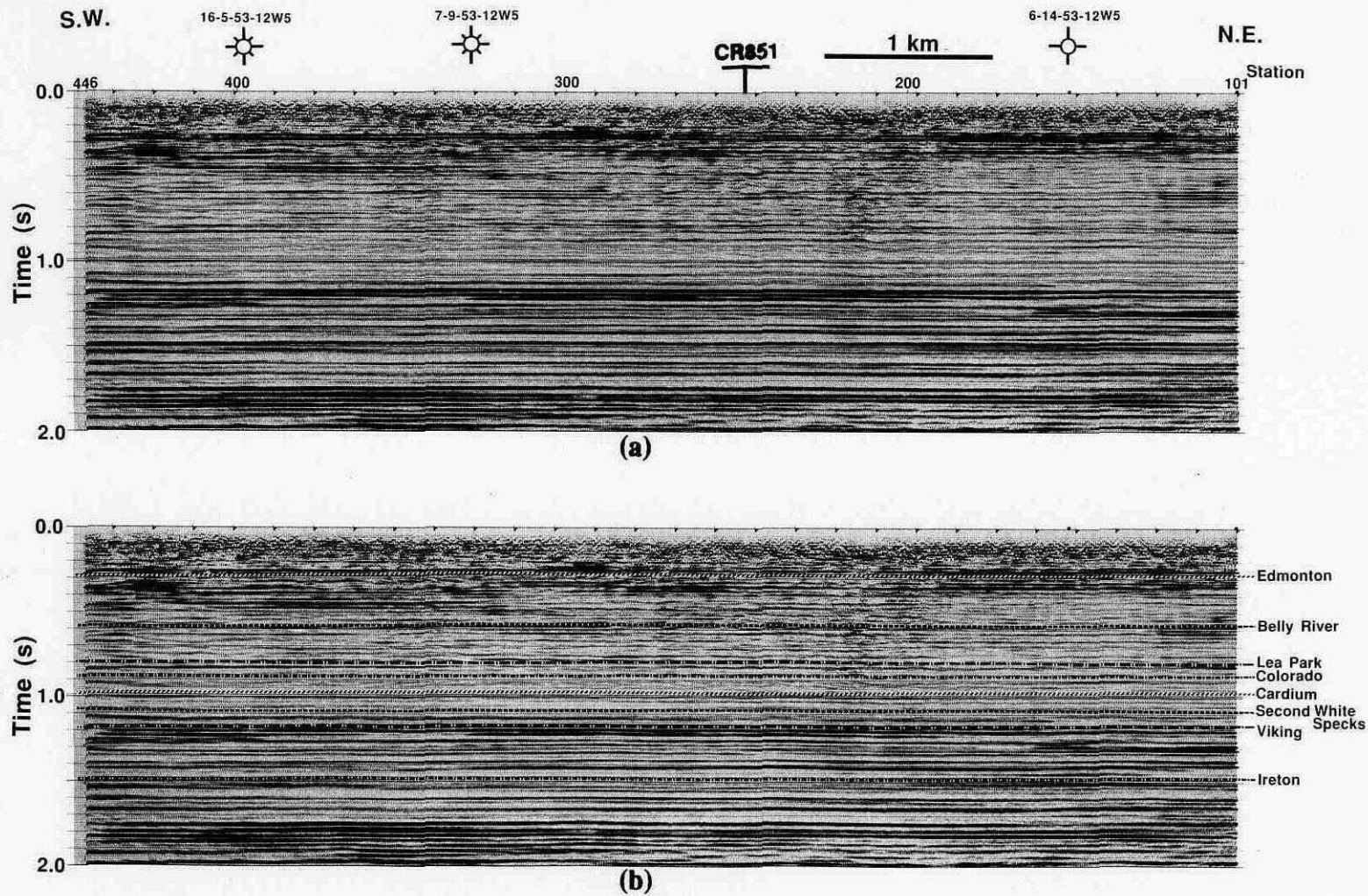


FIG. 5.4. Final migrated stack of line CR852 (a) without and (b) with interpreted events.

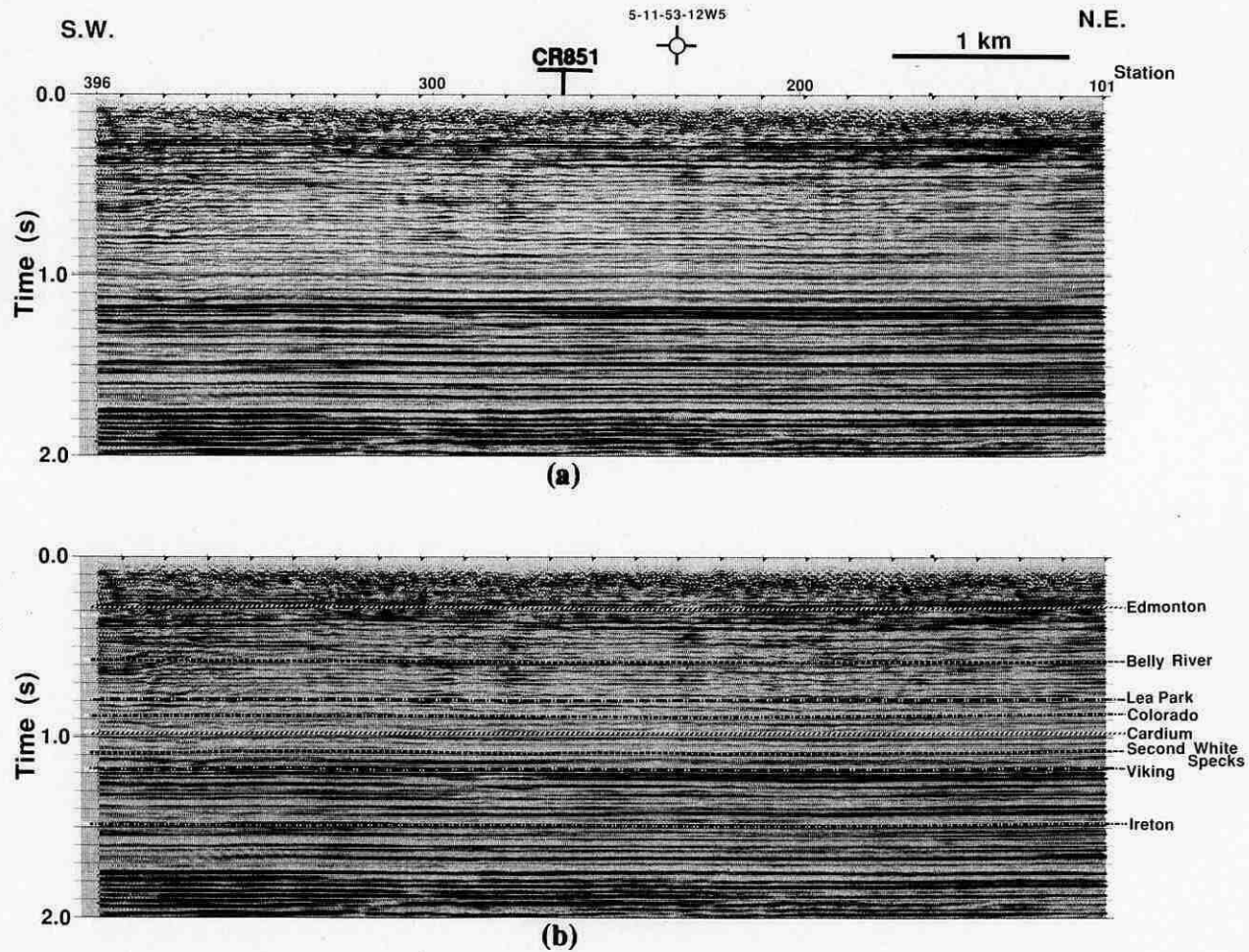


FIG. 5.5. Final migrated stack of line CR853 (a) without and (b) with interpreted events.

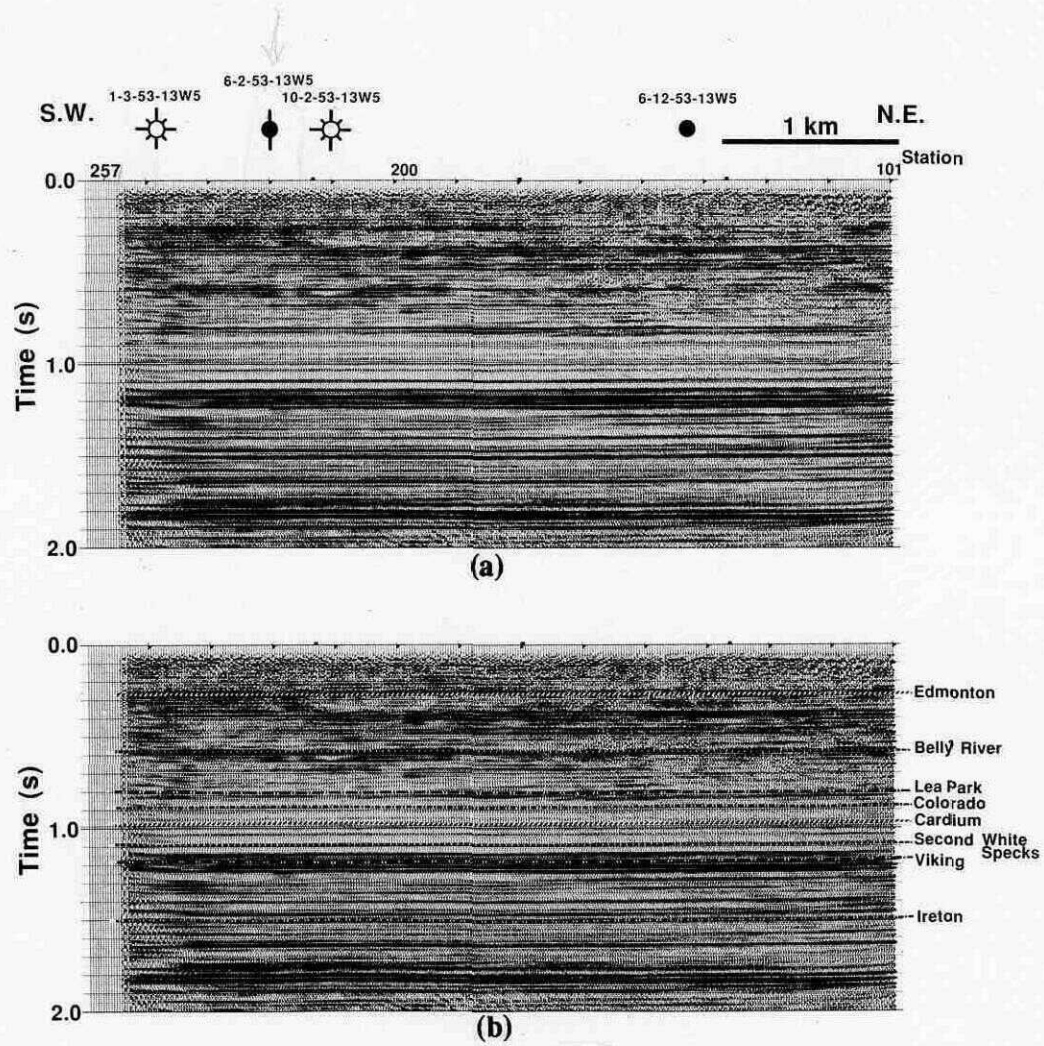


FIG. 5.6. Final migrated stack of the vertical component of line CCSW01 (a) without and (b) with interpreted events.

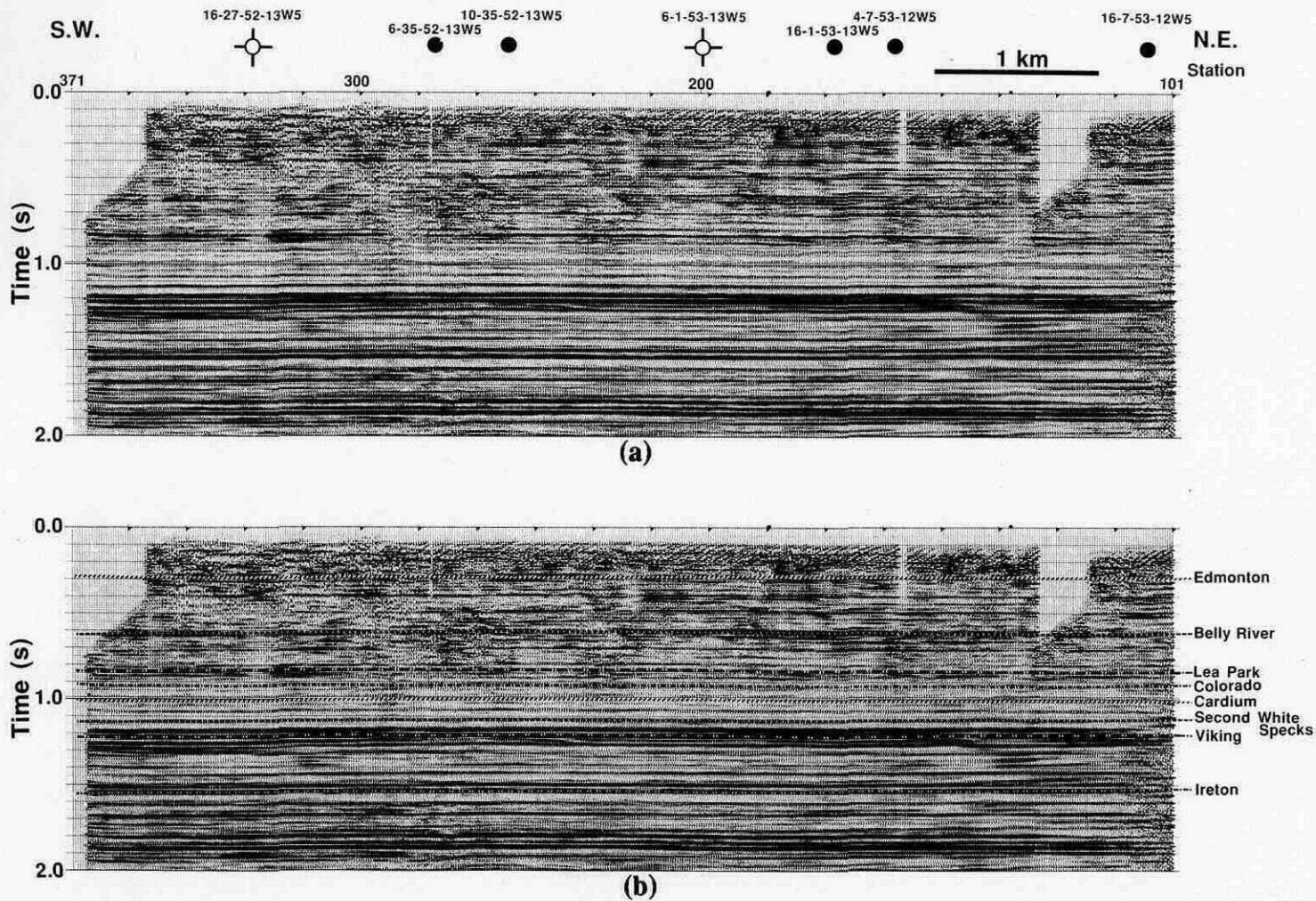


FIG. 5.7. Final migrated stack of the vertical component of line CCSW02 (a) without and (b) with interpreted events.

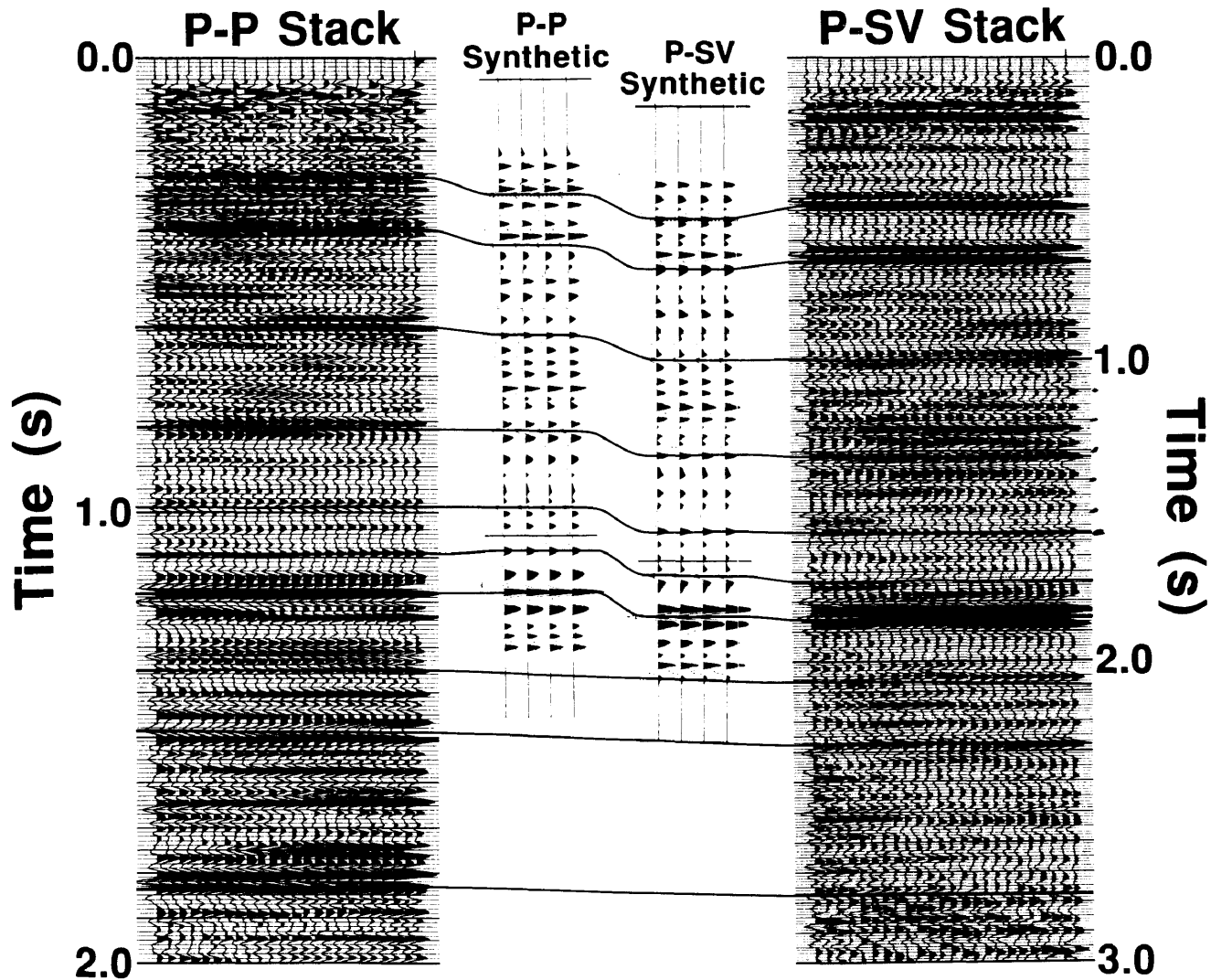


FIG. 5.8. Correlation between the vertical and radial components of line CCSW01, aided by P-P and P-SV synthetic seismograms generated from the P-wave sonic log of well 1-3-53-13W5. Plotted using Aki and Richards (1980) polarity convention.

identification of events, a P-wave synthetic along with a P-SV synthetic generated using the technique discussed by Howell et al. (1991) are included. Figure 5.9 and 5.10 show the radial-component migrated stacks of both multicomponent lines with and without the interpreted events.

The P-wave velocity and density for each layer in the model (Table 5.1), were obtained by blocking (i.e. averaging) the sonic and density logs over the intervals defined by the geologic markers. Of the wells located in the study area (see Figure 1.3), the sonic and density logs of well 1-3-53-13W5 were blocked. This well was chosen because it is located along seismic line CCSW01 and it is typical of wells in the area. All velocity ratios listed in Table 5.1, except for those of the Colorado, Cardium and Blackstone Formations, were determined using the following equation due to Harrison (1989):

$$\frac{V_p}{V_s} = \frac{2I_s}{I_p} - 1 \quad (5.1)$$

where  $I_p$  and  $I_s$  are the time-intervals on the vertical- and radial-component stacks respectively. Table 5.2 shows the results of these calculations. Using the interval  $V_p/V_s$  values and weighting them by their respective P-SV isochrons, average  $V_p/V_s$  values down to each event were also calculated. This procedure was undertaken in order to determine the  $V_p/V_s$  to be used in the asymptotic sorting procedure discussed in Chapter 4.

The seismic parameters of the Cardium conglomerate were based upon core analysis from well 6-12-53-13W5 and full-waveform sonic data collected over the Cardium Formation from wells 12-31-50-10W5 and 16-2-51-11W5, located just south-east of the study area. Using these data, the conglomerates of the Carrot Creek field were found to have an average velocity of 4327 m/s and a Poisson's ratio between 0.18 and 0.22. These values are significantly different from those of the thick shale units of the Wapiabi and Blackstone Formations overlying and underlying the conglomerate. The velocities of these shales, determined from well 1-3-53-13W5, were found to be  $3920 \pm 50$  and  $4003 \pm 50$  m/s respectively. Using equations 5.1 and 1.3 and the full-waveform sonic logs discussed previously,

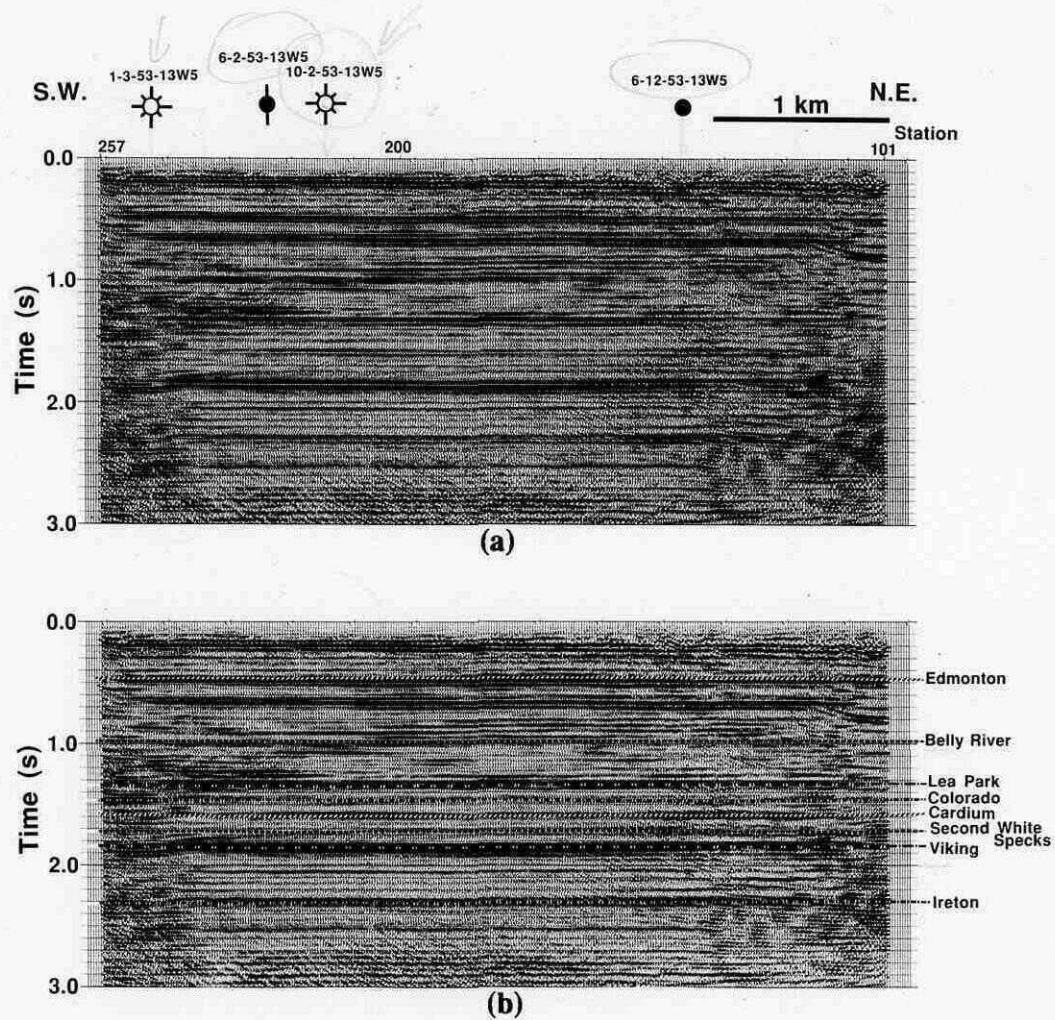


FIG. 5.9. Final migrated stack of the radial component of line CCSW01 (a) without and (b) with interpreted events.

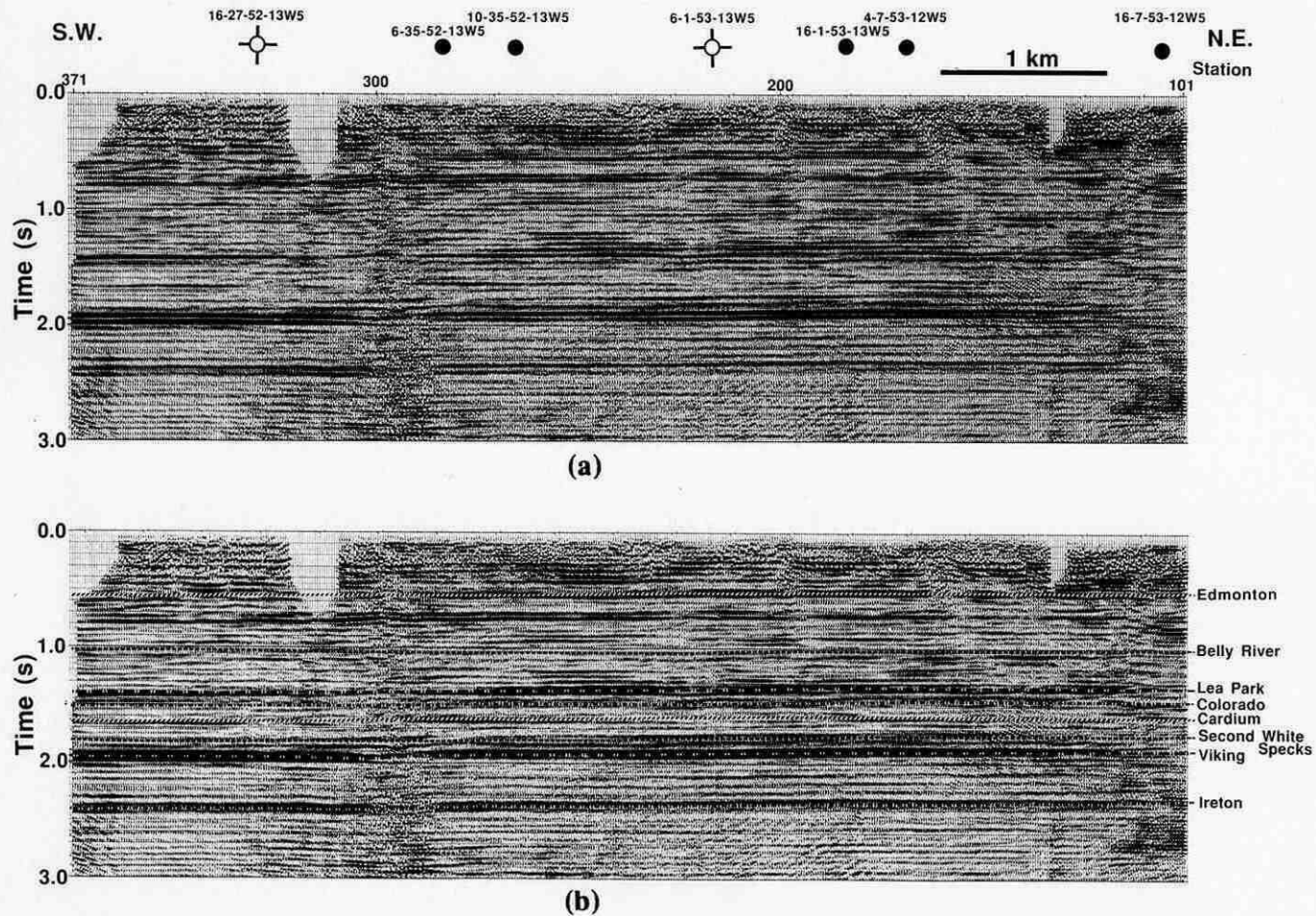


FIG. 5.10. Final migrated stack of the radial component of line CCSW02 (a) without and (b) with interpreted events.

the Poisson's ratios of these shales were determined to be approximately  $0.31 \pm 0.02$ .

Table 5.2.  $V_p/V_s$  for specific seismic intervals based upon interval times of the vertical (P-P) and radial (P-SV) data of line CCSW01

Geologic Marker	Event Travel-time		Isochron		$V_p/V_s$	
	P-P (ms)	P-SV (ms)	P-P (ms)	P-SV (ms)	Interval	Weighted
Edmonton	262	483				
Marker A	378	670	116	187	2.22	2.22
Belly River	590	1000	212	330	2.11	2.15
Lea Park	816	1320	226	320	1.83	2.03
Cardium	995	1593	179	273	2.05	2.03
Marker B	1094	1726	99	133	1.69	2.00
Viking	1185	1850	91	124	1.73	1.97
Marker C	1356	2075	172	225	1.73	1.94
Ireton	1510	2305	154	230	1.88	1.93
Marker D	1640	2503	130	198	2.05	1.94
Marker E	1834	2780	194	277	1.86	1.93

### 5.3 AVO Modeling

The significant difference in P-wave velocity and Poisson's ratio of the Cardium conglomerate, with respect to the encompassing shales, produces a promising situation to undertake amplitude-versus-offset (AVO) analysis. Both P-P (vertical-component) and P-SV (radial-component) AVO modeling was undertaken, using the velocities and densities listed in Table 5.1, to see if the conglomerate produces any observable AVO effects. Since the conglomerate deposits are isolated by thick over- and underlying shales, all modeling involved only the top and bottom interface of the conglomerate. The modeling was undertaken to a maximum source-receiver offset of 2550 m, which corresponds to the far-offset used during acquisition of the multicomponent seismic data. The P-P and P-SV AVO models were generated using Ricker wavelets of 30 and 20 Hz respectively. These frequen-

cies were used since they were determined, using cross-power spectra, to be the dominant frequencies of the Cardium event in the final appropriate seismic sections.

Figure 5.11 and 5.12 show examples of plots of the P-P and P-SV amplitude and phase versus angle of incidence (determined using Zoeppritz equations) of reflections from the top and bottom interfaces of the conglomerate. In these examples, the overlying shale, conglomerate and the underlying shale were assumed to have P-wave velocities of 3920, 4327 and 4003 m/s (from Table 5.1), respectively. Poisson's ratios, taken from Table 5.1, of 0.18 and 0.31 were assumed for the conglomerate and shales, respectively.

Figures 5.11 and 5.12 show that both the P-P and P-SV reflection amplitudes and phases are highly dependent upon the angle of incidence. Several significant differences can be observed between their respective responses.

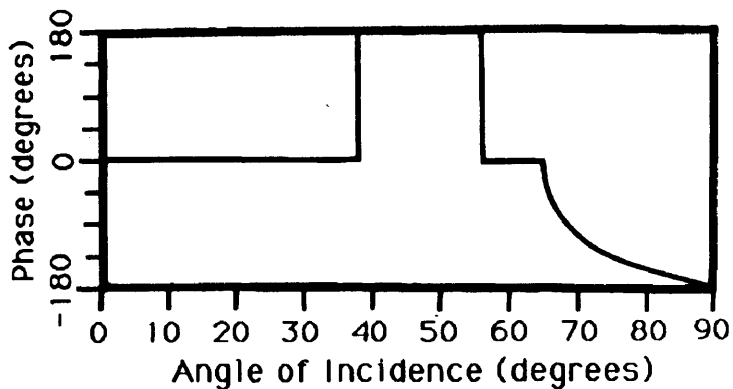
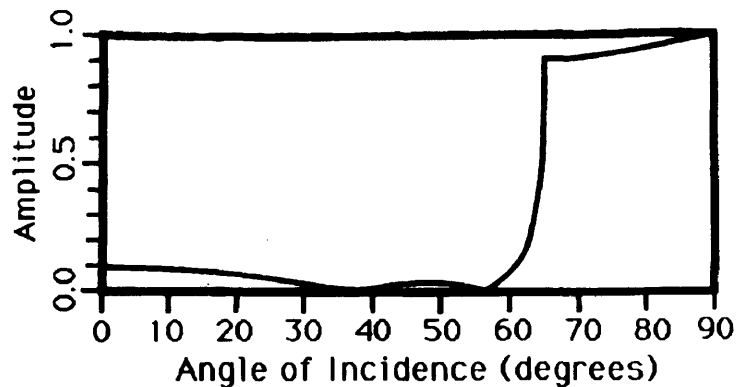
- i) The P-P and P-SV amplitudes appear to be inversely related up to angles of incidence just less than the critical angle; P-P amplitudes are decreasing with increasing angle of incidence (e.g. from  $0^\circ$  to approximately  $30^\circ$ ) whereas the P-SV amplitudes are increasing, and vice versa.
- ii) At small angles of incidence, for both a positive and negative impedance contrast (i.e. top and bottom of the conglomerate), the P-P data will be phase-shifted  $180^\circ$  with respect to the P-SV data (i.e. opposite polarity). This response results from the Aki and Richards' (1981) polarity convention.
- iii) At angles of incidence of approximately  $38^\circ$  and  $29^\circ$ , for the top and bottom interfaces respectively, the P-P amplitude decreases to zero. For incidence beyond these angles, the reflection amplitudes then increase but are  $180^\circ$  phase-shifted (i.e. polarity reversed) to make the reflections the same phase as those for the P-SV data. Other phase shifts also occur past the critical angles, but these will not be considered since angles of incidence this large are not reached in the Carrot Creek data set.

### Overlying Shale

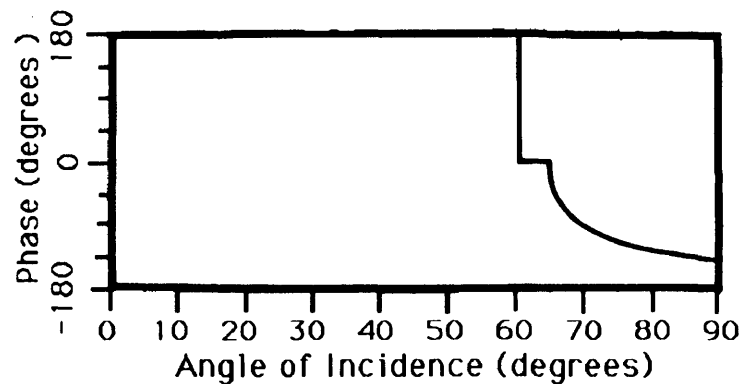
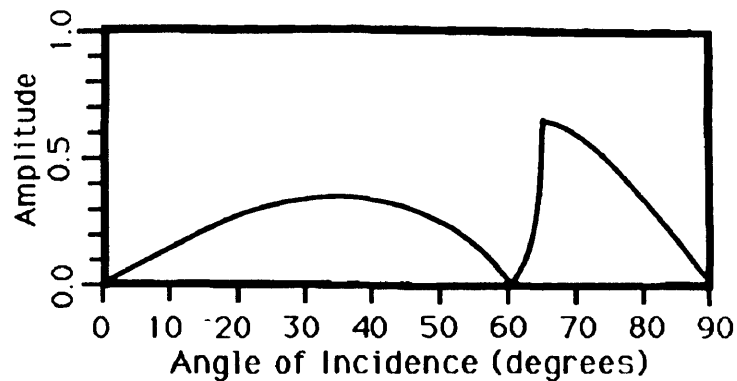
$$\begin{aligned} \rho_1 &= 2.380 \text{ gm/cm}^3 \\ V_{p1} &= 3920 \text{ m/s} \\ V_{s1} &= 2057 \text{ m/s} \\ \sigma &= 0.31 \end{aligned}$$

### Conglomerate

$$\begin{aligned} \rho_2 &= 2.610 \text{ gm/cm}^3 \\ V_{p2} &= 4327 \text{ m/s} \\ V_{s2} &= 2591 \text{ m/s} \\ \sigma &= 0.18 \end{aligned}$$



(a)



(b)

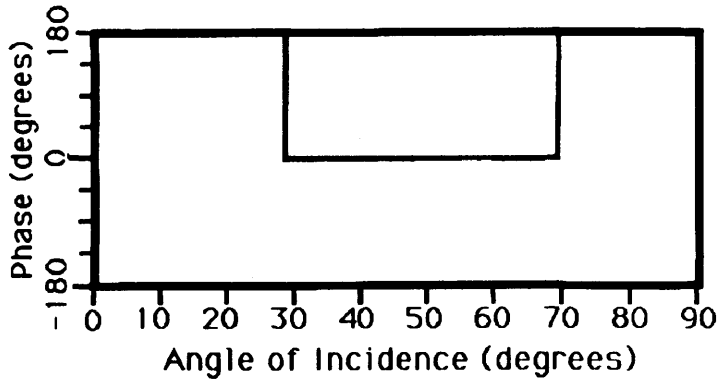
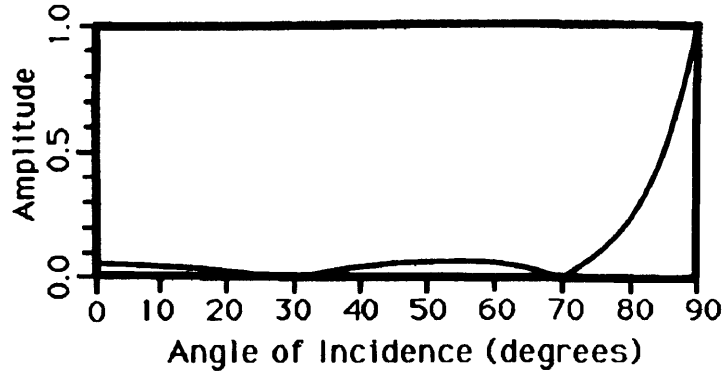
FIG. 5.11. Amplitude and phase for the (a) P-P and (b) P-SV events from the top of the conglomerate (seismic parameters are listed above). Note the P-P reflection undergoes polarity reversals at 38° and 56° (P-P critical angle occurs at 65°).

### Conglomerate

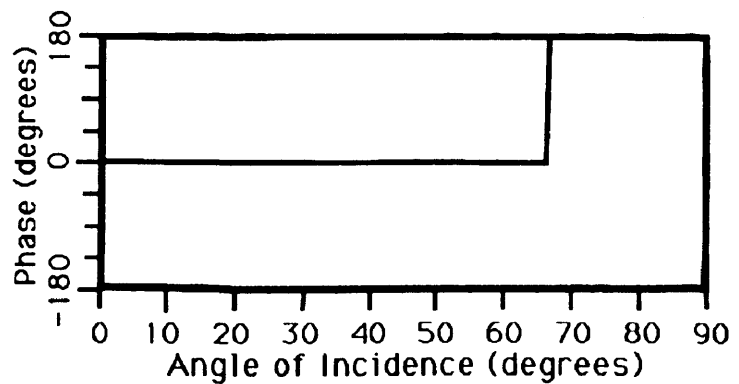
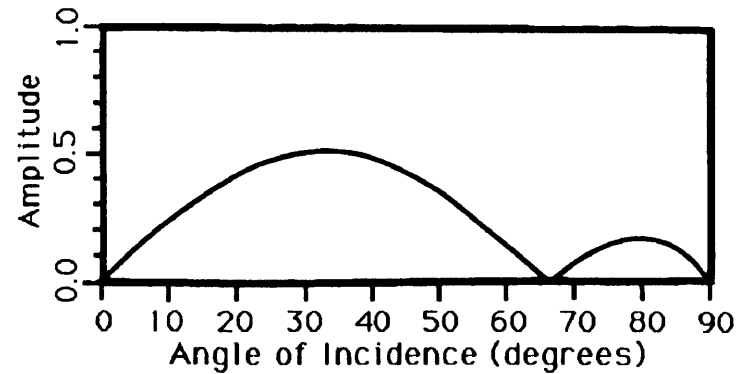
$\rho_2 = 2.610 \text{ gm/cm}^3$   
 $V_{p2} = 4327 \text{ m/s}$   
 $V_{s2} = 2591 \text{ m/s}$   
 $\sigma = 0.18$

### Underlying Shale

$\rho_3 = 2.510 \text{ gm/cm}^3$   
 $V_{p3} = 4003 \text{ m/s}$   
 $V_{s3} = 2100 \text{ m/s}$   
 $\sigma = 0.31$



(a)



(b)

FIG. 5.12. Amplitude and phase for the (a) P-P and (b) P-SV events from the bottom of the conglomerate (seismic parameters are listed above). Note the P-P polarity reversals at 29° and 70° (no P-P critical angle is present).

It should be noted that although these amplitude and phase plots represent the response for a specific set of velocities and densities, the trends observed would occur for any case in which the conglomerate has a higher P-wave velocity and lower Poisson's ratio than the surrounding shale. Differences would only occur in relative amplitude and the position of the polarity changes.

### 5.3.1 Tuning Effect

The above results indicate that strong individual AVO effects should be produced from the top and bottom interfaces of the conglomerate. However, because of the thin nature of the conglomerate deposits, interference between the top and bottom events (i.e. tuning of the events) has to be determined. Figure 5.13 shows an example of the seismic response with respect to offset (i.e. the AVO response) of the P-P and P-SV reflections for the top, bottom, and combined interfaces of a 15 m-thick conglomerate having a Poisson's ratio of 0.22. The combined response will hereafter be referred to in this thesis as the Cardium event. Note the polarity reversal that occurs with offset in the combined response for the P-P but not the P-SV Cardium event. The P-P peak-trough response at near-offsets becomes a trough-peak at far-offsets, whereas the P-SV trough-peak response occurs over all offsets. Another feature of the P-P data is an amplitude minimum at mid-offsets while a corresponding maximum is observed in the P-SV case.

To gain a full understanding of the conglomerate AVO response, the effect of variation in the conglomerate's Poisson's ratio and thickness had to be modeled.

### 5.3.2 Thickness Dependency

Figure 5.14 shows the P-P AVO response and corresponding amplitude of the Cardium peak, for conglomerate thicknesses ranging from 5 to 20 m. This figure shows the P-P data to be sensitive to variation in conglomerate thickness, with the sensitivity being quite

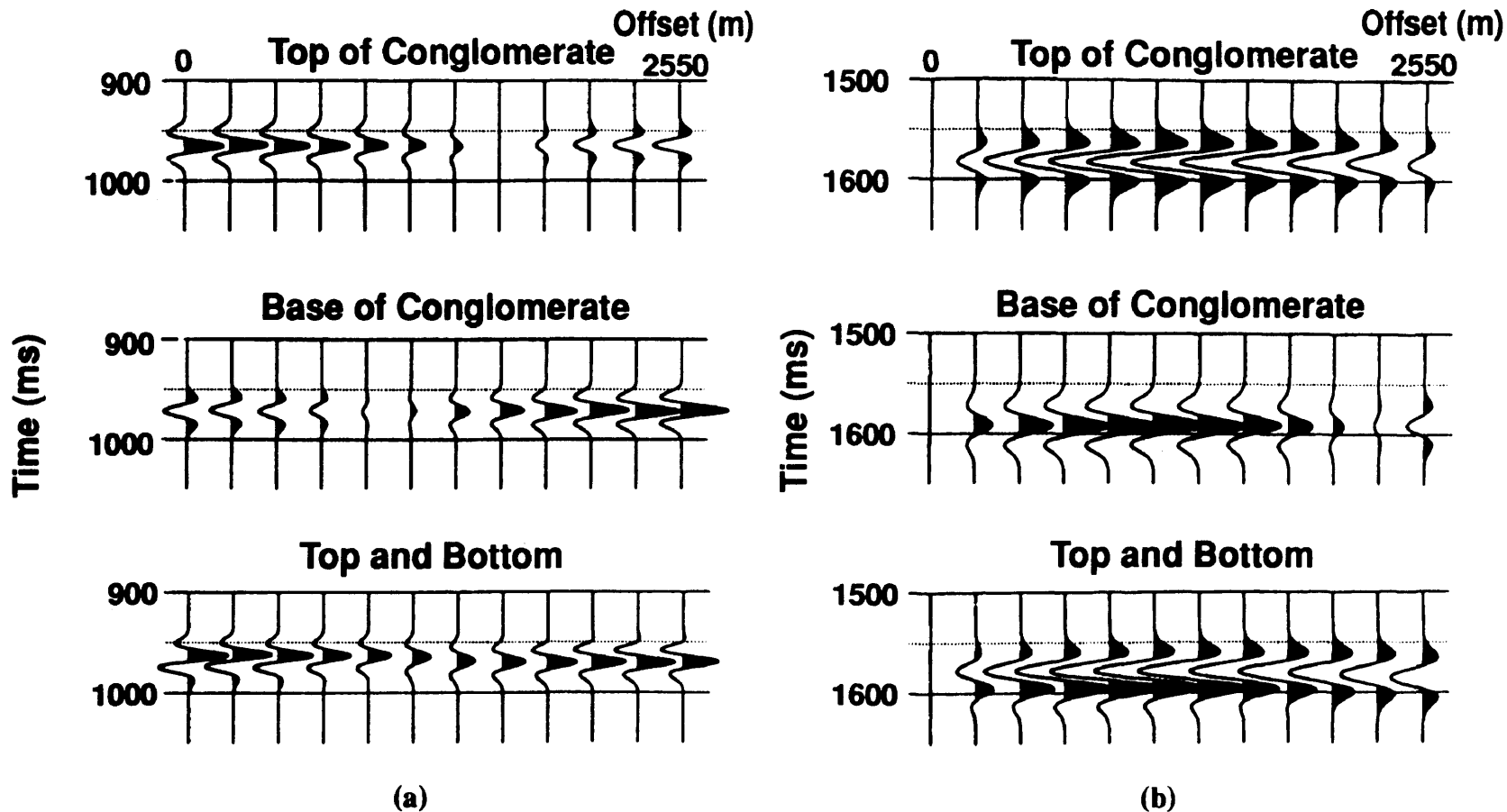
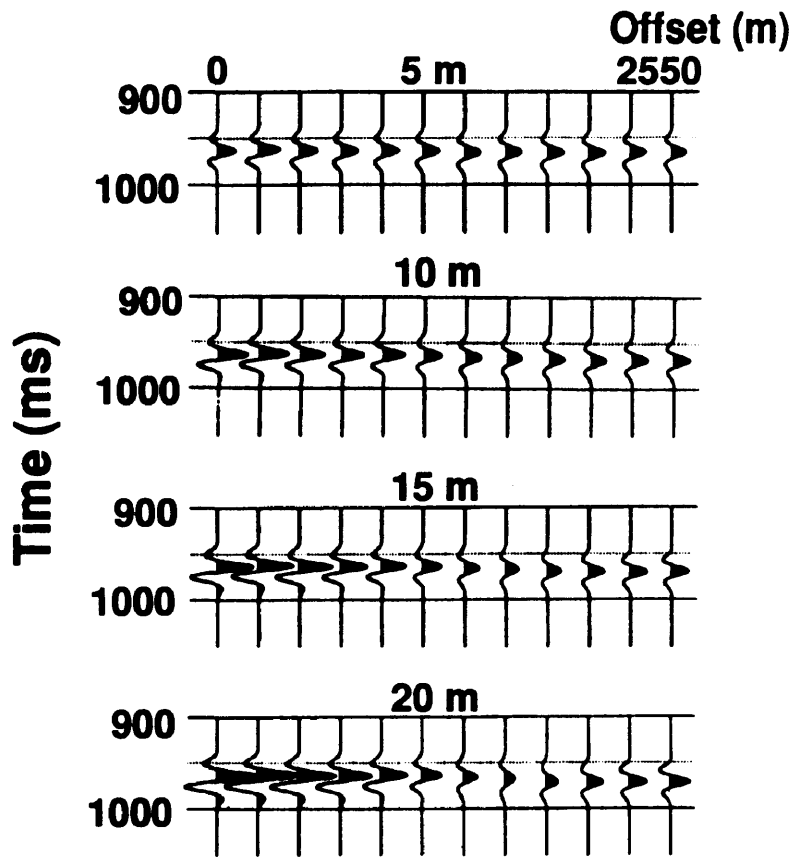
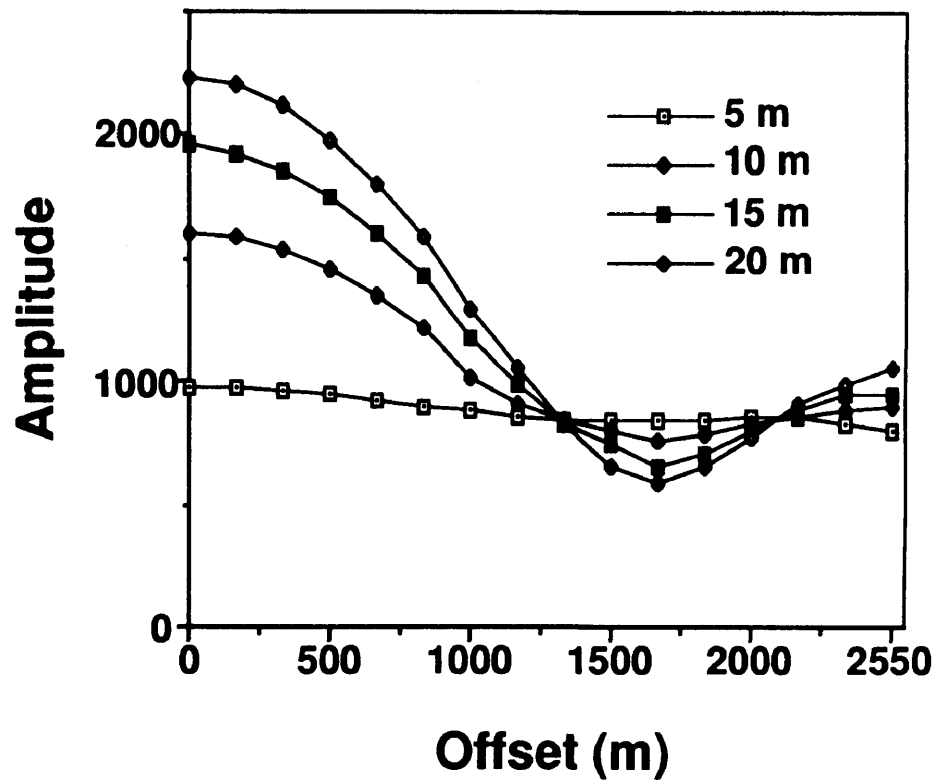


FIG. 5.13. Cardium AVO response for (a) P-P and (b) P-SV case of a 15 m thick conglomerate with a Poisson's ratio of 0.22. The Poisson's ratio of the over- and underlying shales is kept at 0.31. Note that a polarity reversal occurs with the combined P-P event but not the P-SV event.



(a)



(b)

FIG. 5.14. The effect of variation in conglomerate thickness on the P-P (a) seismic response and (b) the amplitude of the Cardium peak. The Poisson's ratio of the conglomerate and the over- and underlying shales are kept at 0.22 and 0.31 respectively. Note the Cardium Peak amplitude is at a minimum at mid-offsets and shows greatest sensitivity to thickness variations at near-offsets.

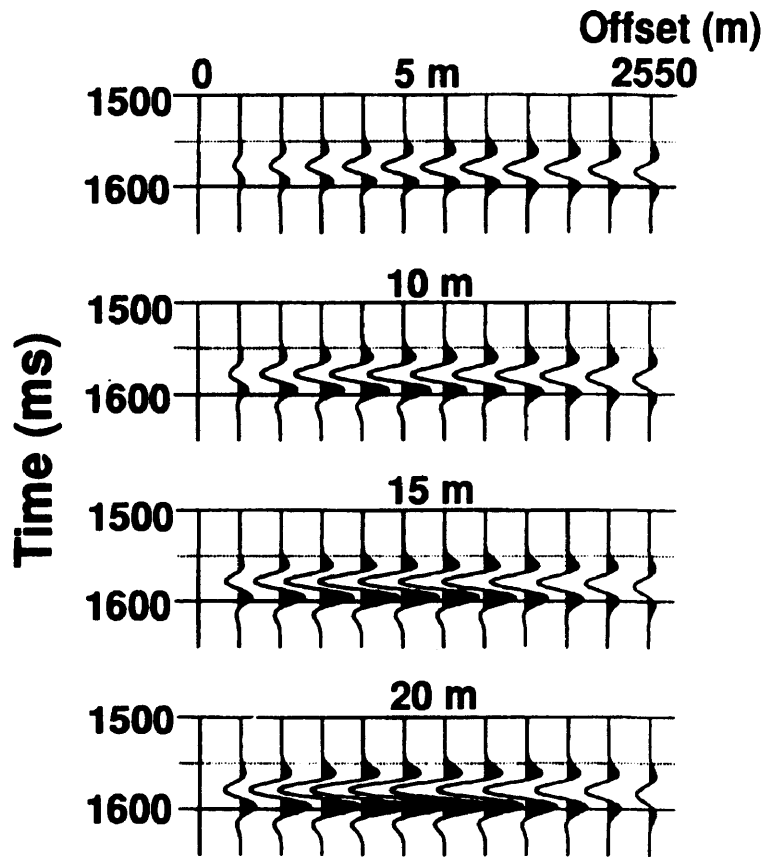
high in the near-offset range (0-1000 m). As mentioned previously, an amplitude minimum is observed in the mid-offset range (1000-2000 m). Unlike the near- and far-offset ranges, the mid-offset range exhibits an amplitude decrease with increasing conglomerate thickness.

The P-SV AVO response and corresponding amplitudes of the Cardium trough are shown in Figure 5.15 for the same range of thicknesses as in Figure 5.14. The P-SV data also shows a definite sensitivity to variation in conglomerate thickness. In this case, however, the greatest sensitivity is observed in the mid-offset range (1000-2000 m) with increasing thickness causing increasing amplitudes.

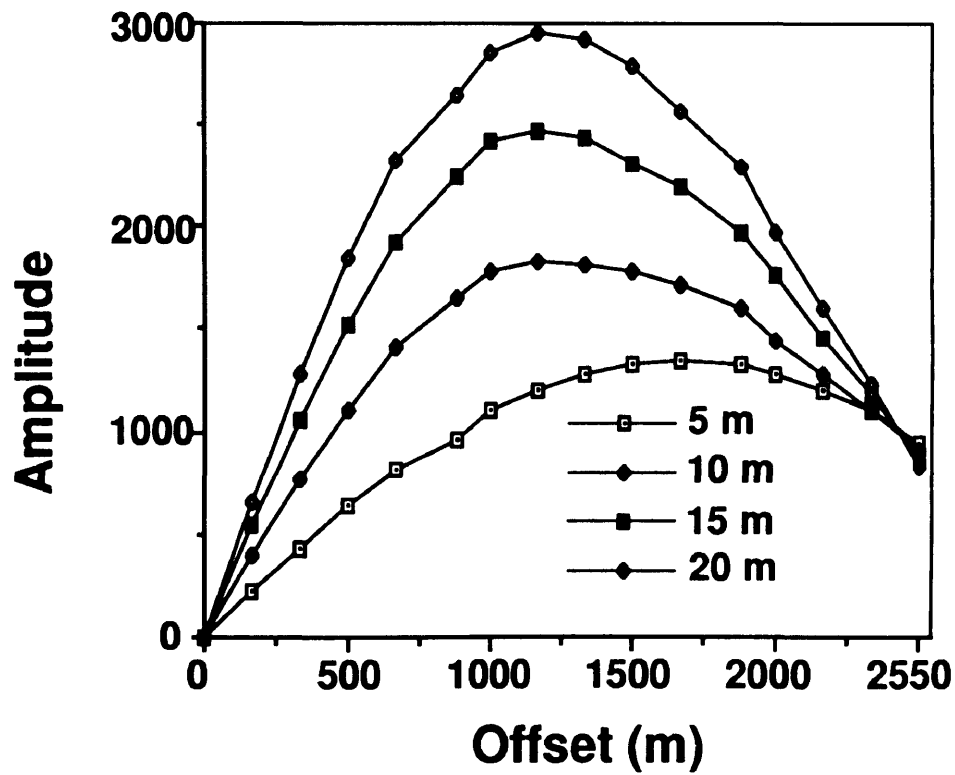
### 5.3.3 Poisson's Ratio Dependency

Figure 5.16 shows the P-P AVO response and corresponding amplitudes of the Cardium peak for Poisson's ratios of the conglomerate varying from 0.15 to 0.28. All variations in Poisson's ratio were obtained by changing  $V_s$  and keeping  $V_p$  constant. As in the case for variation in thickness (Figure 5.14), this figure also shows the P-P data to be quite sensitive to variations in Poisson's ratio. In this case, however, the greatest sensitivity is observed in the far-offset range (>1500 m). Increasing Poisson's ratio, in effect, shifts the amplitude minimum from the mid-offsets to the far-offsets. However, this far-offset dependency upon Poisson's ratio would most likely not be observed on the vertical component Carrot Creek data since the majority of the far-offset data have been removed by the front-end mute.

The P-SV AVO response and corresponding amplitudes of the Cardium trough for Poisson's ratios varying from 0.15 to 0.28, are shown in Figure 5.17. Over the range of 0.18 to 0.22 for Poisson's ratio of the conglomerate (discussed in Section 5.2), the P-SV AVO response does not appear to vary as much as that observed in the P-P case. Also, the P-SV AVO response does not appear to vary as much as that observed when the conglomerate's thickness is varied over the range of 5 to 20 m (Figure 5.15). For instance, much smaller

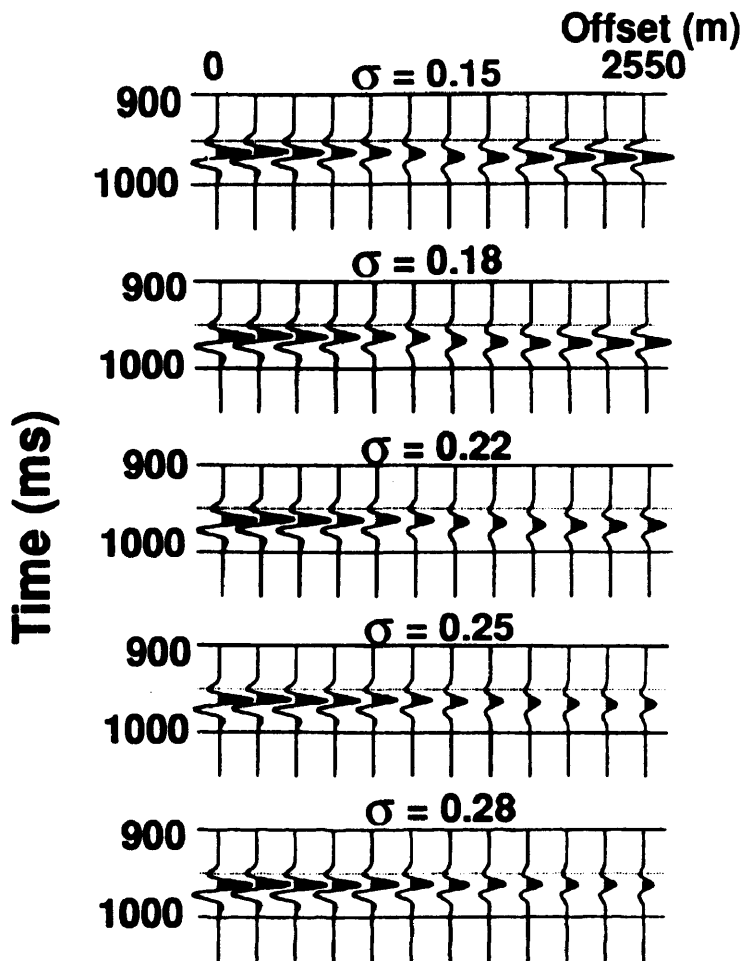


(a)

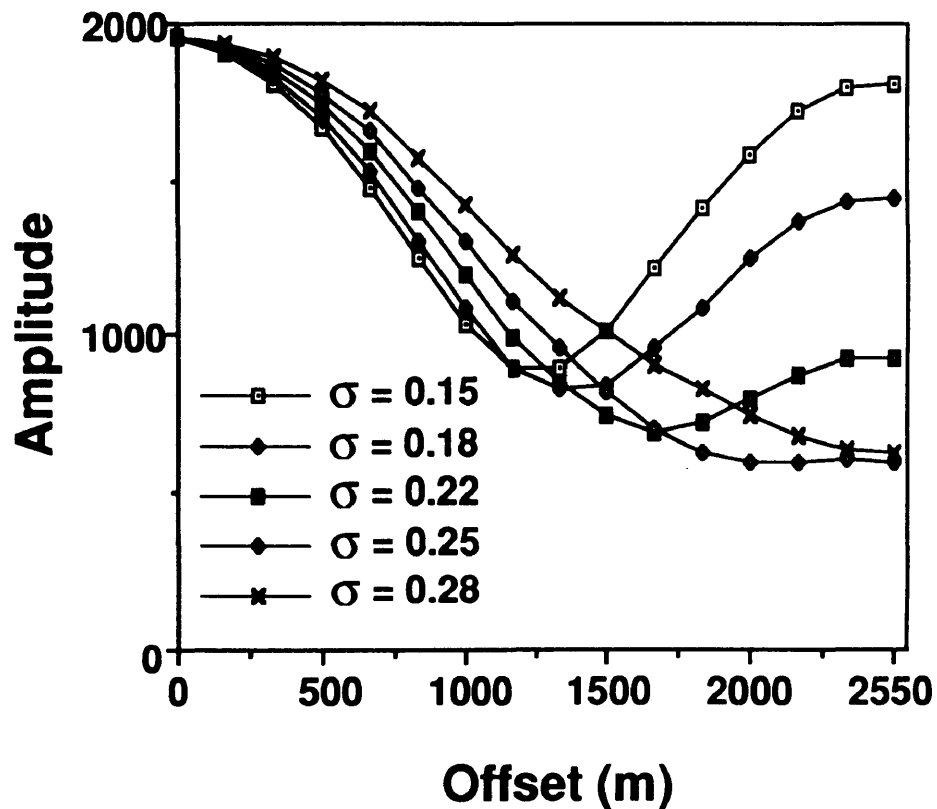


(b)

FIG. 5.15. The effect of variation in conglomerate thickness on the P-SV (a) seismic response and (b) the amplitude of the Cardium trough. The Poisson's ratio of the conglomerate and the over- and underlying shales are kept at 0.22 and 0.31 respectively. Note the amplitude of the Cardium trough shows the greatest sensitivity at thickness variations at mid-offsets.



(a)



(b)

FIG. 5.16. The effect of variation in the conglomerate's Poisson's ratio on the P-P (a) seismic response and (b) the amplitude of the Cardium peak. The conglomerate's thickness and the Poisson's ratio of the over- and underlying shales are kept at 15 m and 0.31 respectively. Note the amplitude of the Cardium peak exhibits the greatest sensitivity to variation in Poisson's ratio at far-offsets.

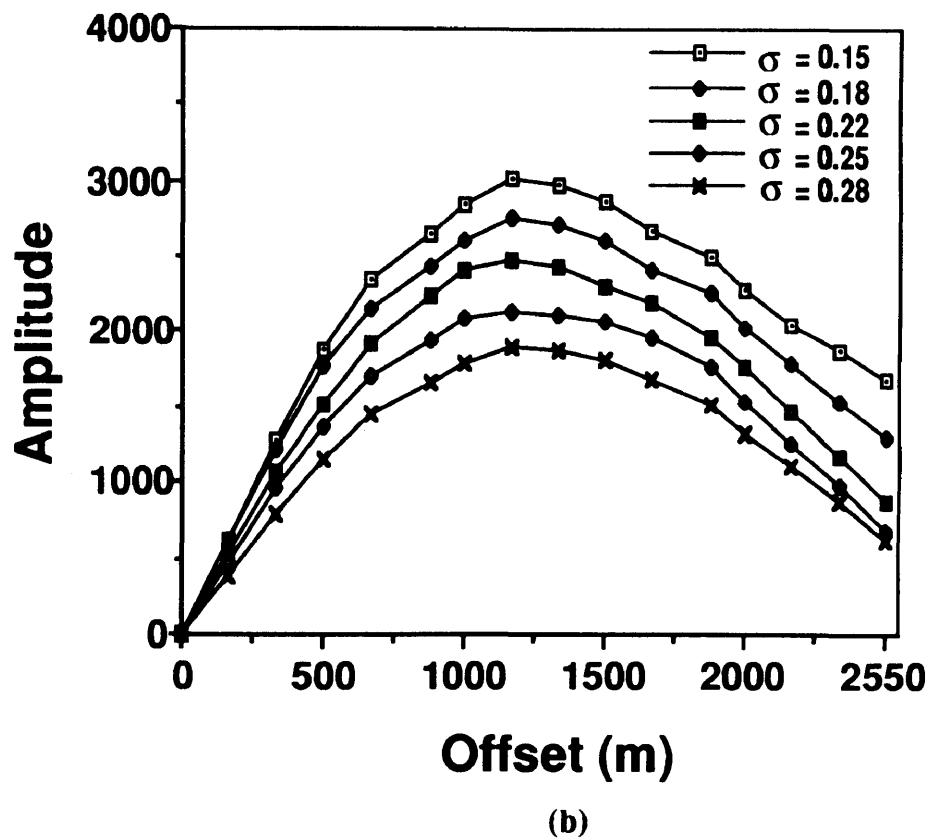
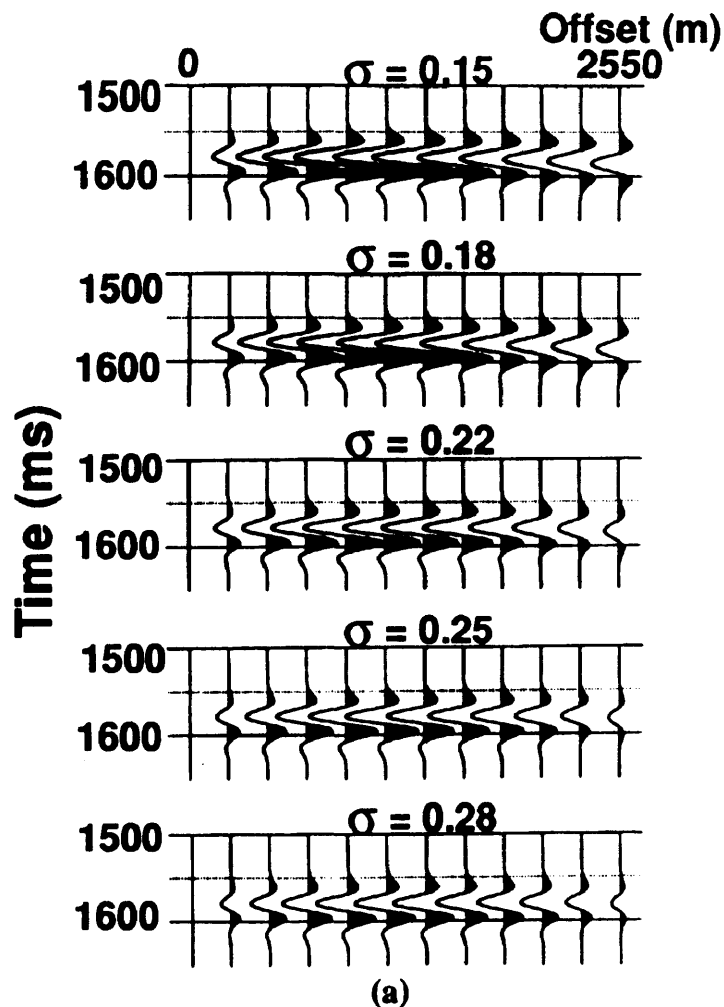


FIG. 5.17. The effect of variation in the conglomerate's Poisson's ratio on the P-SV (a) seismic response and (b) the amplitude of the Cardium trough. The conglomerate's thickness and the Poisson's ratio of the over- and underlying shales are kept at 15 m and 0.31 respectively. Note the amplitude of the Cardium trough is does not show great sensitivity to variation in Poisson's ratio.

increases in amplitude are observed in the mid-offset range (1000-2000 m), for decreasing Poisson's ratio (i.e. 0.22 to 0.18), than is observed when the thickness of the conglomerate is increased from 5 to 20 m (Figure 5.15).

#### **5.4 AVO Analysis of Carrot Creek Data**

In order to see if any of these AVO effects are present in the surface seismic data, various offset-range stacks were produced from the vertical (P-P) and radial (P-SV) components of the multicomponent seismic lines. The offset-stacks were generated over 500 m intervals (i.e. 0 - 500 m, 500 - 1000 m, etc.) using the same processing flows as described in Chapters 3 and 4. For both the P-P and P-SV cases, the 2000 - 2500 m stacks were not generated since the Cardium event in this range was partially removed by the front-end mute. Figures 5.18 and 5.19 show the offset stacks of a portion of the vertical- and radial-component stacks of lines CCSW02 and their respective amplitudes for the Cardium event (i.e. peak for the vertical component and trough for the radial component). These portions of the seismic line were chosen because of their high signal-to-noise ratio. To help reduce random noise for the picking of the amplitudes, a trace mix (weighting: 10-20-40-20-10) was applied over 5 adjacent traces.

The results from both the P-P (vertical-component) and P-SV (radial-component) offset-stacks support the conclusions predicted by modeling. The P-P case, for instance, shows a change in character from a Cardium peak-trough at near-offsets to a trough-peak at far-offset due to a polarity reversal (indicated by the downward shift in the Cardium peak with increasing offset). Amplitudes of the various stacks also indicate a minimum at mid-offset ranges on the vertical component. An interesting feature of these stacks is that although the 0-500 m offset-range generally possesses higher amplitudes than the 500-1000 m range, the Cardium event appears to be more coherent in the 500-1000 m range. This phenomenon was also documented by Wren (1984) and appears to arise because of the presence of source-

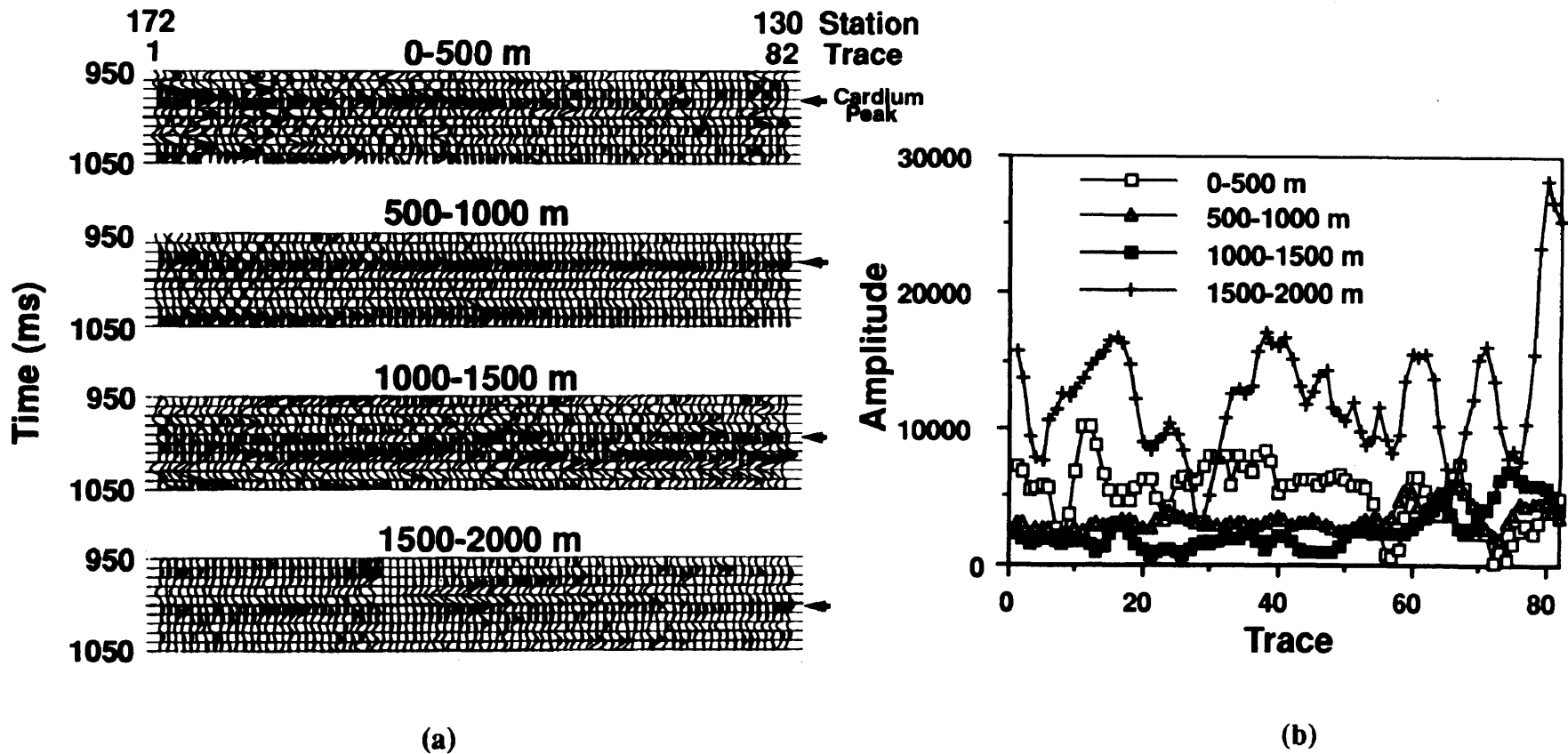
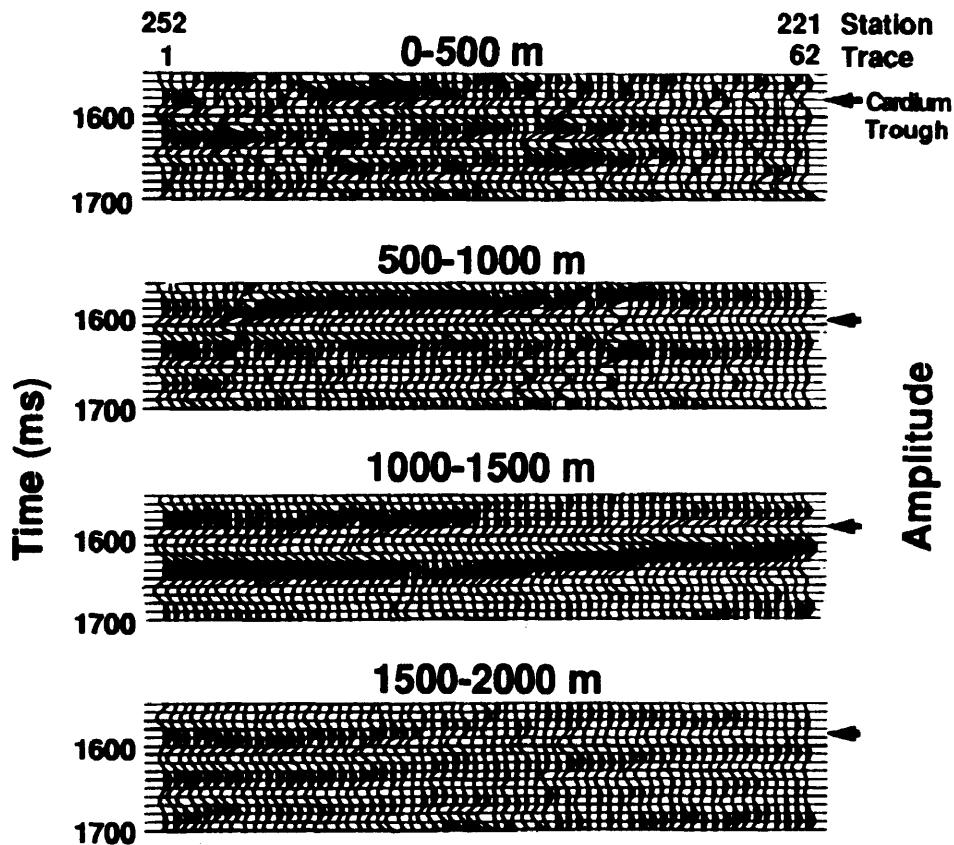
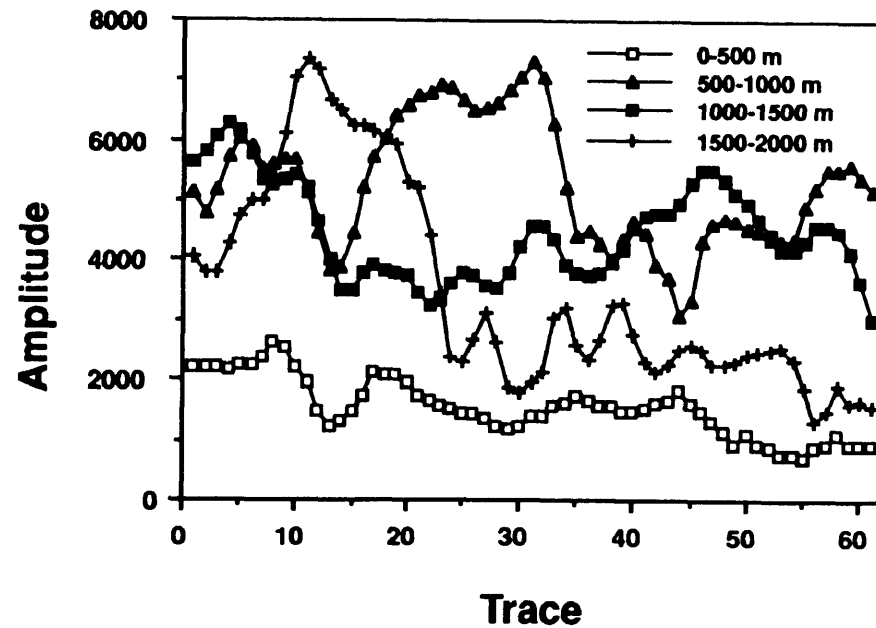


FIG. 5.18. (a) Offset-stacks of the P-P (vertical-component) data of line CCSW02 and the (b) amplitudes of the corresponding Cardium peaks. Note how the Cardium peak becomes delayed in panels of greater offset and exhibits an amplitude minimum at mid-offsets.



(a)



(b)

FIG. 5.19. (a) Offset-stacks of the P-SV (radial-component) data of line CCSW02 and the (b) amplitudes of the corresponding Cardium troughs. Note how the amplitude of the Cardium trough exhibits a maximum at mid-offsets.

generated air-waves in the 0-500 m offset-range. This results in a greater fluctuation in the Cardium amplitude which in turn causes a decrease in coherency after scaling of the data. The P-SV case, on the other hand, shows the greatest amplitude in the mid-offset ranges (500-1000 m, 1000-1500 m and 1500-2000 m). The 0-500 m offset-range exhibits significantly lower amplitudes due to less P-SV conversion occurring.

### 5.5 Lateral Changes in $V_p/V_s$

As demonstrated in Section 5.2,  $V_p/V_s$  information can be extracted from multicomponent seismic data using vertical- and radial-component isochron values. However, instead of using this technique to obtain  $V_p/V_s$  values at one location, as done in Section 5.2, values can be calculated along the entire seismic line, and using equation 1.3, Poisson's ratio profiles can be generated. These profiles, in turn, can be used to identify lateral variations in Poisson's ratio, which may be indicative of lithologic changes within a specific interval.

This Poisson's ratio interval analysis was found to be useful in identifying variation in the thickness of the Cardium conglomerate in the Carrot Creek field. This ability arises from the conglomerate having a high P-wave velocity and a low  $V_p/V_s$  value relative to the surrounding shales. Because of the higher velocity of the conglomerate, variation in conglomerate thickness will produce varying amounts of pull-up of underlying events. This pull-up will in turn decrease the isochron of any interval in which the conglomerate is contained. The thicker the conglomerate, the larger the pull-up of underlying events and therefore the greater the thinning of the isochron. Because of the low  $V_p/V_s$  of the conglomerate, a larger relative velocity contrast will occur between the conglomerate and the surrounding shales for S- than P-waves (i.e. the average difference between the conglomerate and the surrounding shales for the S- and P-wave velocities are 25% and 9% respectively). This difference in velocity contrasts will therefore result in a greater amount of isochron thinning for P-SV than P-P data as the conglomerate thickness increases. Using equations 5.1

and 1.3, this difference in isochron thinning will then result in  $V_p/V_s$  and therefore Poisson's ratio lows in areas of thick conglomerate.

In this thesis, the Poisson's ratio analysis was undertaken over three intervals; Lea Park - Blackstone, Lea Park - Marker A and Lea Park - Second White Specks. These intervals were chosen because they can be confidently correlated between the vertical- and radial-component seismic sections, in addition to containing the Cardium conglomerate. The close proximity of these events to the conglomerate is also important, because the smaller the isochron interval the greater the effect the conglomerate will have upon the interval  $V_p/V_s$  and therefore the Poisson's ratio deduced.

The results of this analysis for line CCSW01 are shown in Figure 5.20. Two Poisson's ratio lows are observed on these profiles, indicating that, as the seismic interval increases (i.e. Lea Park - Blackstone to Lea Park - Second White Specks), the lows in the Poisson's ratio become less apparent. The attenuation of these lows with increasing interval size arise because the conglomerate contributes less to the overall velocity of the interval.

Due to the lower signal-to-noise ratio on line CCSW02, the coherency of the events was not as strong as CCSW01 and therefore the same analysis could not be undertaken with any confidence.

## 5.6 Discussion

### 5.6.1 Event Amplitude

As indicated by Figure 5.8 most of the major P-P (vertical-component) reflections correlate well with P-SV (radial-component) reflections, with only differences in relative amplitude between events being present. The most significant differences in amplitude occurs with the Viking and Cardium events. Figures 5.9 and 5.10 show, for instance, that the Viking event exhibits anomalously high amplitudes relative to the other P-SV events, compared to the P-P data. These large Viking amplitudes are surprising since the angles of

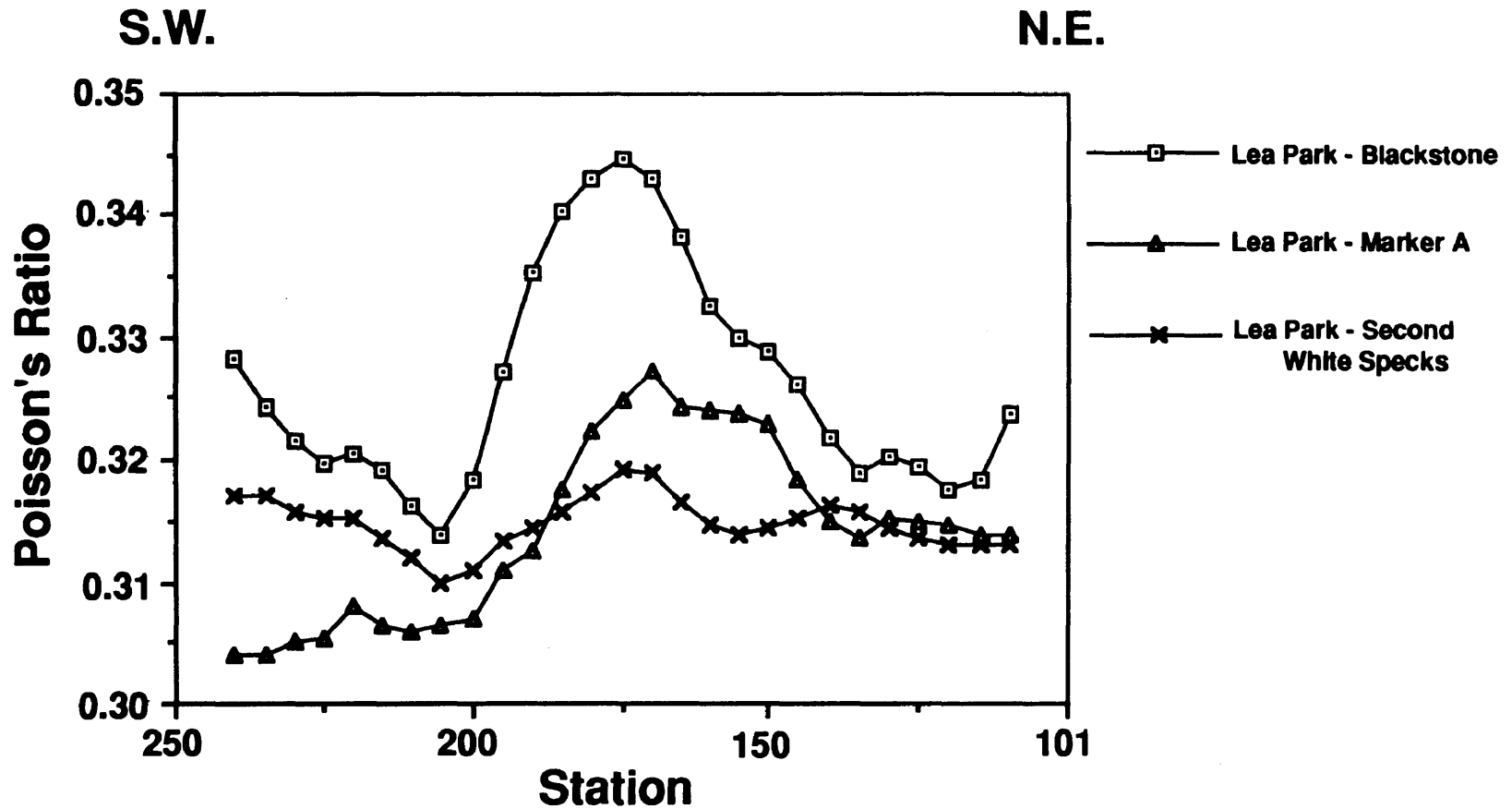


FIG. 5.20. Interval Poisson's ratios calculated from line CCSW01 using various isochrons (isochrons listed above). Note the lows in Poisson's ratio towards the ends of the line, due to the presence of thick conglomerates.

incidence on this interface are less than 10 degrees (i.e. little P-SV conversion should be occurring). These large amplitudes are in fact due to tuning of three events; the Viking, the Joli Fou and the Mannville. This tuning effect is shown in Figure 5.21 and matches well with the Viking event located at 1.8 s on the P-SV synthetic of Figure 5.8.

The Cardium event, on the other hand, exhibits two strong amplitude anomalies on both of the P-SV sections while only a very subtle amplitude increase can be observed on the P-P sections at these same locations (Figure 5.22). This significant difference in amplitude between the P-P and P-SV data can be attributed to the AVO effect modeled in Section 5.3. More specifically, the weaker P-P amplitudes arise because of a polarity reversal observed with increasing offset. Therefore, upon stacking, the Cardium P-P event will become attenuated due to destructive interference as the near- and far-offset are stacked together. The event of the radial component, on the other hand, does not exhibit a polarity reversal and therefore traces over all offsets stack constructively, producing a much stronger Cardium response.

Because the P-SV response is more sensitive to variation in conglomerate thickness than Poisson's ratio (as shown in Section 5.3), the P-SV amplitude anomalies are interpreted to be caused primarily by an increase in conglomerate thickness. This is supported by the fact that these anomalies occur at the location of presently producing, thick conglomerate bodies. This is also supported by Figure 5.23 which shows the correlation between the P-SV amplitude anomalies with increases in the isopach of Figure 2.4 and lows in the calculated Poisson's ratios (Lea Park - Blackstone interval); i.e. both indicating an increased conglomerate thickness.

### 5.6.2 Offset-range Stacking

From the modeling of Section 5.3, it can also be concluded that full-offset stacking can be detrimental for P-P reflections when large source-receiver offsets are acquired. Figure

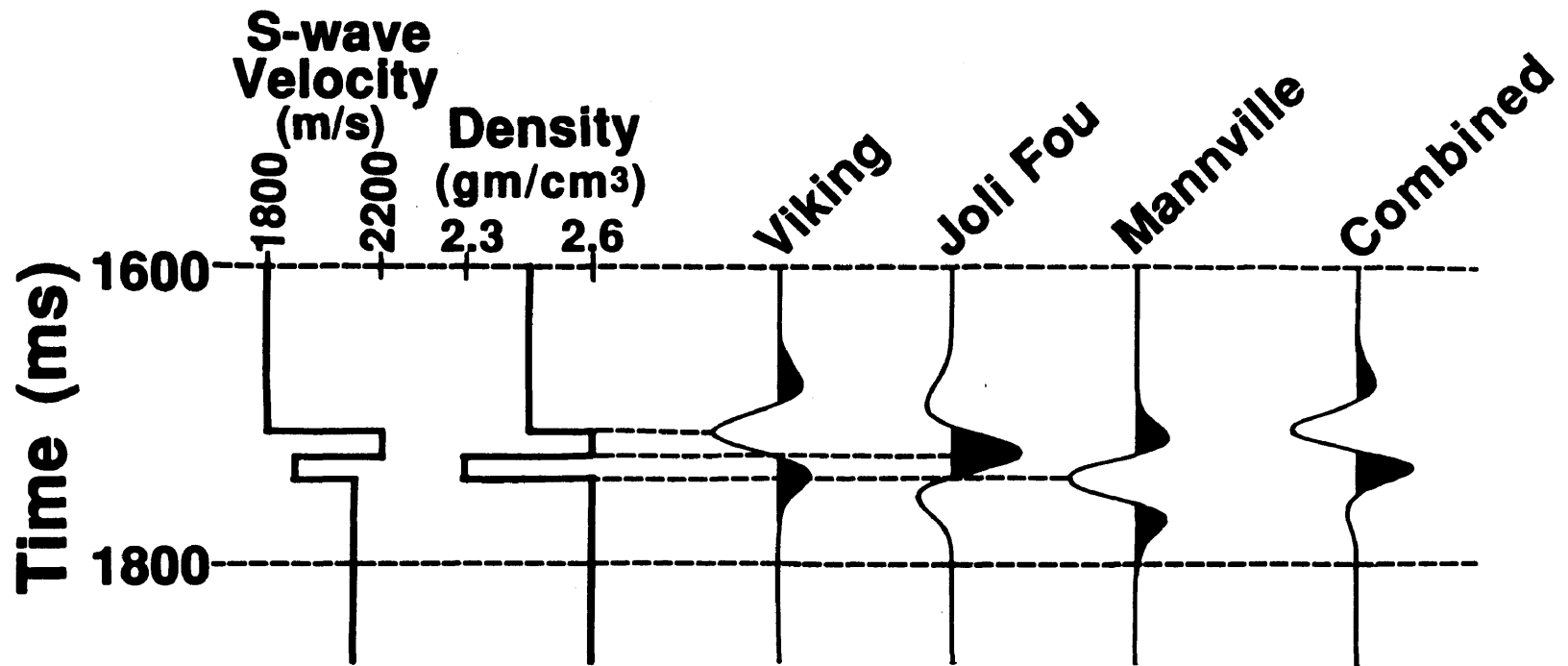


FIG. 5.21. P-SV tuning of the Viking, Joli Fou and Mannville events using velocities and densities listed in Table 5.1. Note all traces are scaled to equal amplitude.

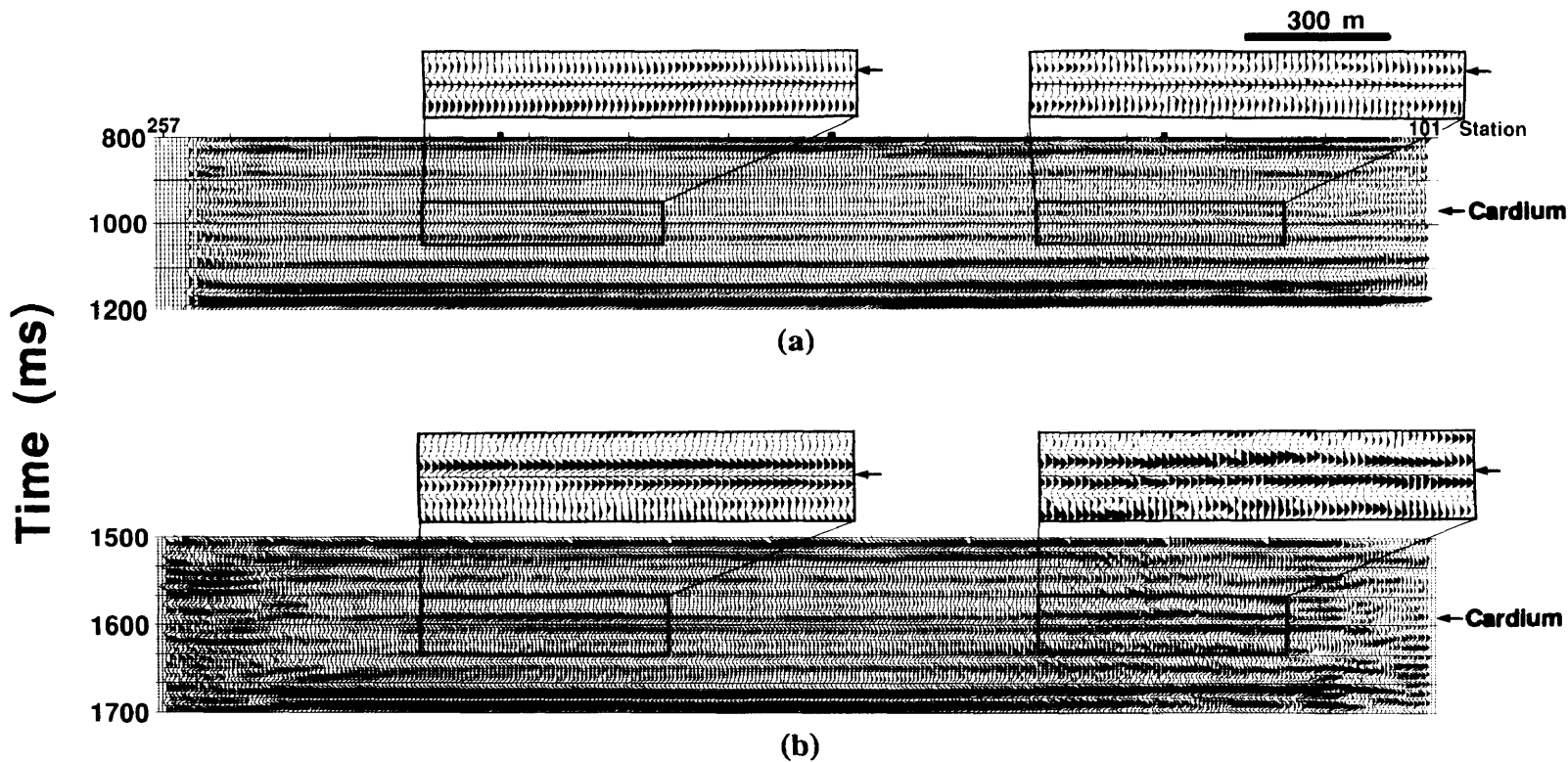
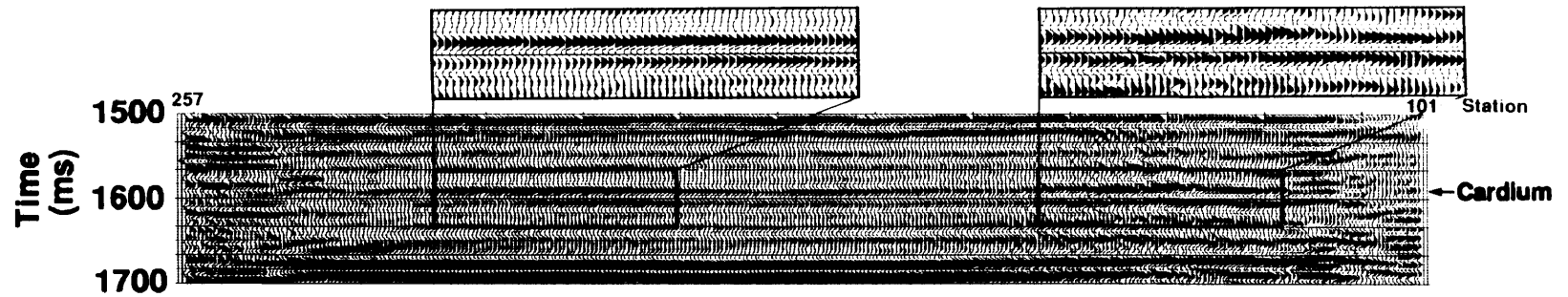
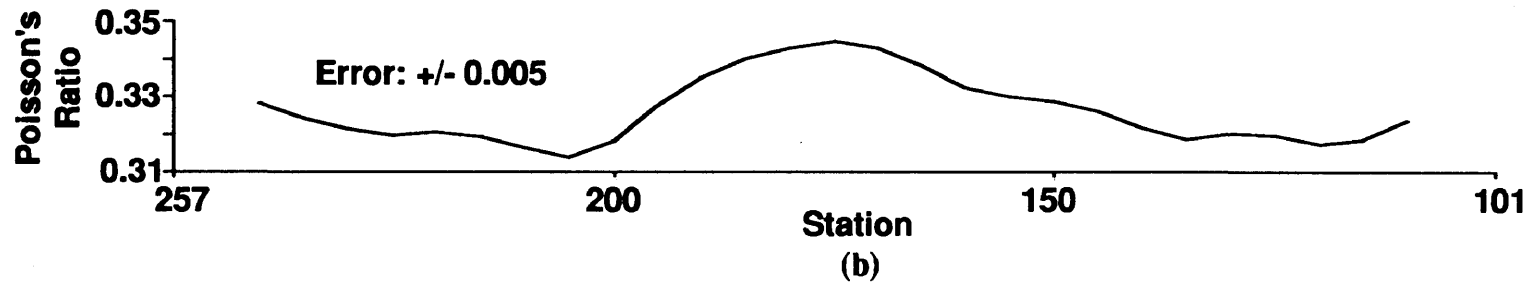


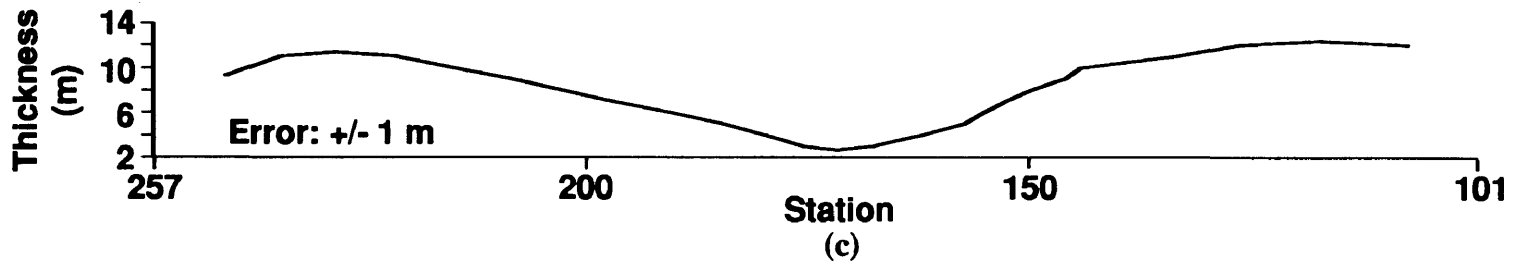
FIG. 5.22. Cardium event of the (a) vertical and (b) radial components of line CCSW01 with the amplitude anomalies highlighted. Note the P-SV anomalies exhibit a higher relative amplitude than the P-P anomalies.



(a)



(b)



(c)

FIG. 5.23. Comparison between (a) the P-SV Cardium amplitude anomaly, (b) the conglomerate interval isopach, and (c) the Poisson's ratio for the Lea Park - Blackstone interval of line CCSW01. Note the correlation between the Poisson's ratio lows, the isopach highs, and the location of the P-SV amplitude anomalies.

5.14 (Section 5.3) indicates that the vertical-component should in fact better resolve the conglomerate and variation in its thickness, using a near-offset stack. This figure shows that the P-P near-offsets should exhibit large amplitudes that should be sensitive to the thickness of the conglomerate (i.e. assuming the conglomerate has a low Poisson's ratio). This is contrary to the P-SV data which shows its greatest sensitivity to conglomerate thickness at mid-offsets (Figure 5.15). Figure 5.24 shows the P-P Cardium event of line CCSW01 from a 0-1000 m offset-stack, along with the corresponding P-SV Cardium event. As predicted, significantly stronger P-P amplitude anomalies than those observed in the full-offset stack of Figure 5.22 can now be seen at the same location as the P-SV anomalies. This, in turn, helps support the conclusion that the P-SV anomalies are indeed due to the presence of thicker conglomerates.

These results indicate that the conventional data (lines CR851, CR852 and CR853) should therefore be able to identify any variation in conglomerate thickness without the need to produce offset-range stacks. This is the case since the far-offsets of these seismic lines are not large enough for a polarity reversal to occur (i.e. far-offset 1200 m), and therefore the cancellation effect observed in the multicomponent P-P data should not occur. Figure 5.25 shows the Cardium event for a portion of these three seismic lines. In this figure, the Cardium event exhibits only subtle variations in amplitude along all three lines, and is relatively weak in amplitude. This lack of variation in amplitude can be interpreted only as a subtle variation in the conglomerate thickness. The low amplitude of the Cardium event itself indicates the conglomerate unit is either very thin in the area or contains a large amount of shale. An increased shale content would, in turn, result in a decrease in the velocity of the conglomerate interval, and would therefore result in a drop in acoustic impedance, thus causing a decrease in the amplitude of the Cardium event. Increasing shale content would also cause a drop in the Poisson's ratio of the conglomerate interval.

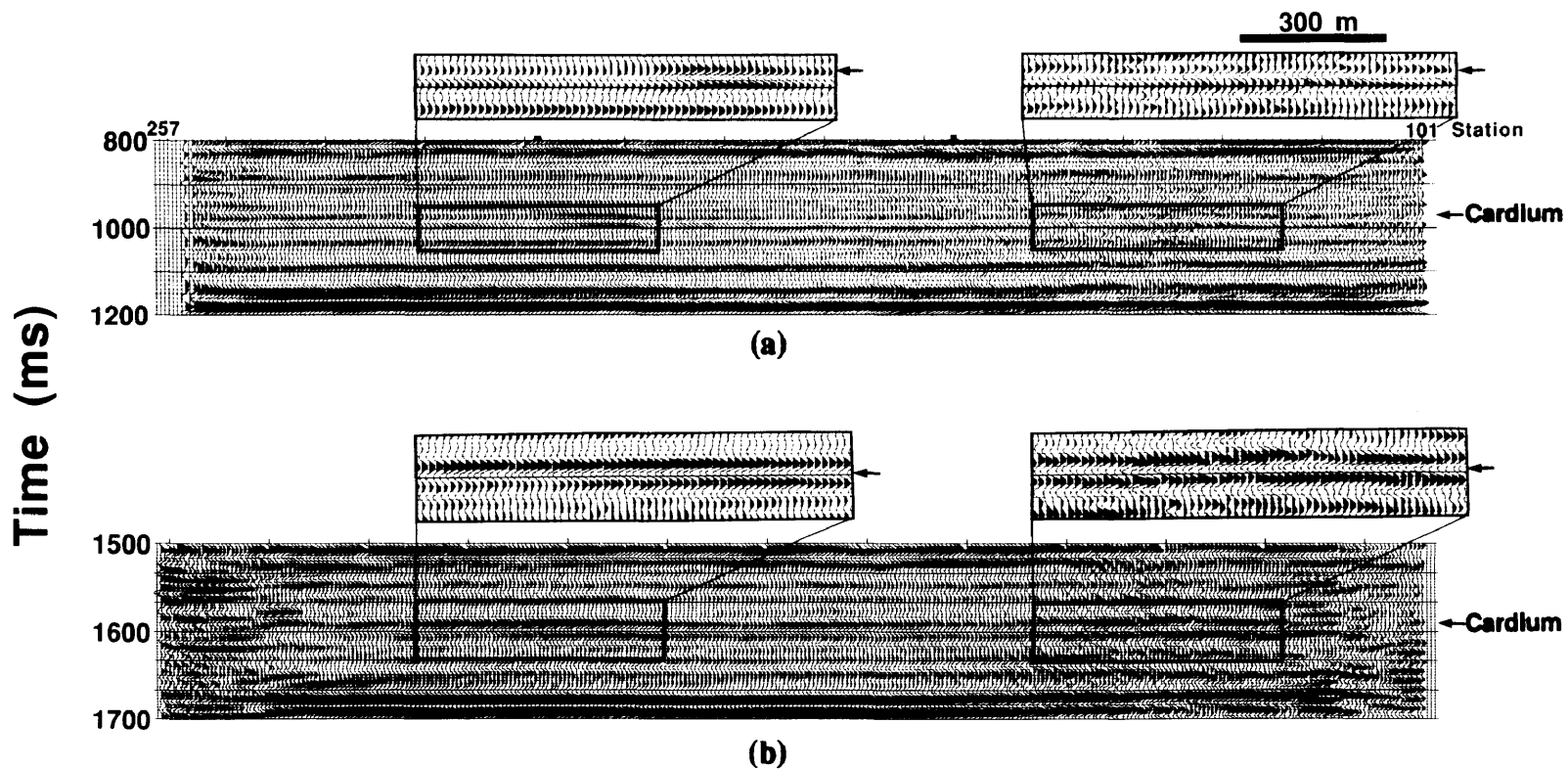


FIG. 5.24. Comparison of the Cardium event from (a) a 0-1000 m P-P offset-range stack and (b) the final radial-component stack of line CCSW01. A strong P-P Cardium amplitude anomaly occurs at the same location as the P-SV amplitude anomalies.

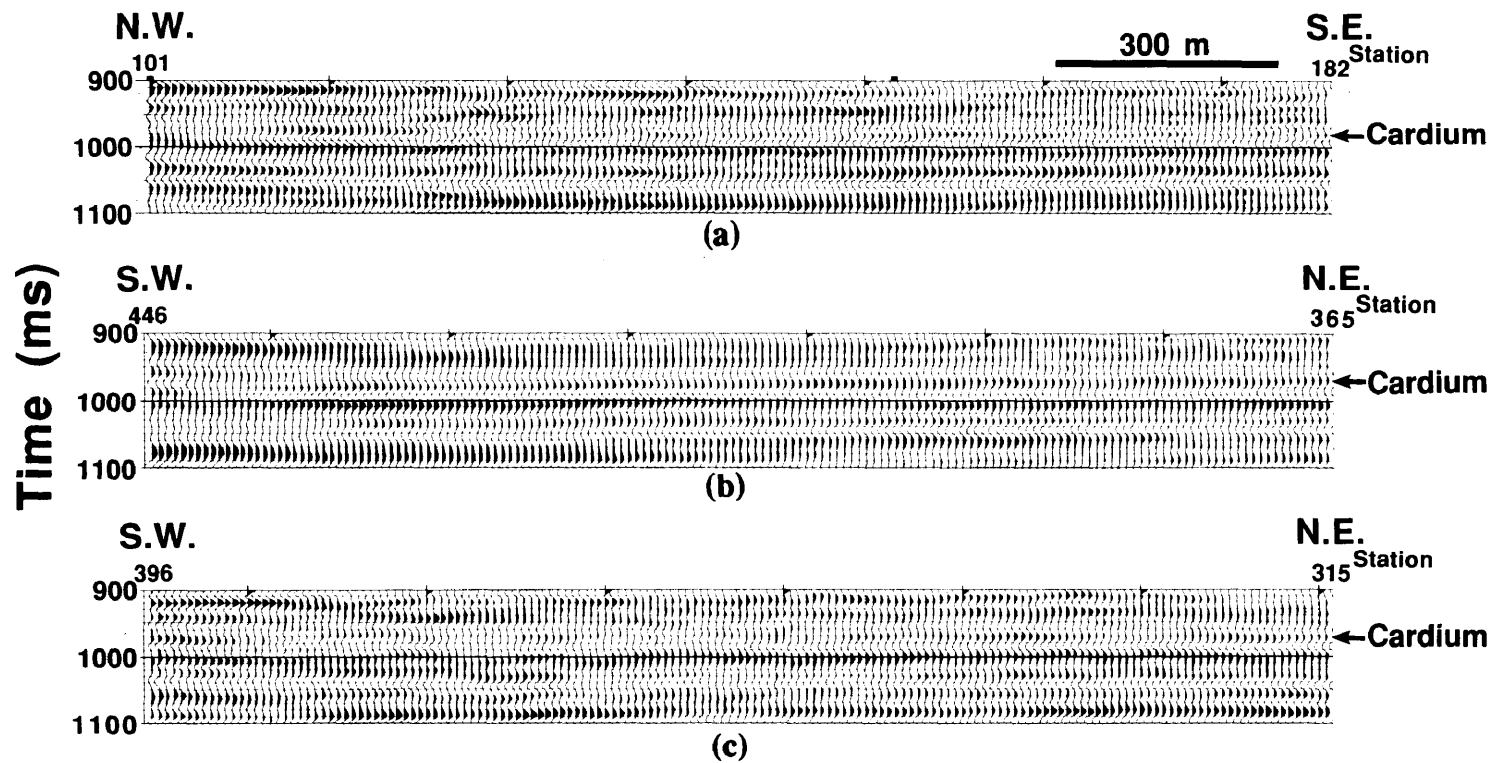


FIG. 5.25. The Cardium event from a portion of line (a) CR851, (b) CR852 and (c) CR853. Note the low coherency of the Cardium event.

### 5.6.3 Limiting the Far-offset

It has generally been believed that, when acquiring multicomponent seismic data, large source-receiver offsets are desirable. The results discussed above, however, indicate that in the Carrot Creek field this is not necessarily the case. The far-offsets of the Carrot Creek field, for example, can be detrimental to the imaging of the P-P Cardium event (discussed in Section 5.6.1) when generating full-offset stacks. In addition, as indicated by the AVO modeling results (Section 5.3) and the amplitude plots of Figures 5.11 and 5.12, it is the P-SV mid-offsets (500-2000 m) which exhibit the greatest amount of conversion, not the far-offsets (>2000 m). It can therefore be concluded that larger offsets are not necessarily always beneficial in the acquisition of multicomponent data. Better imaging can often be obtained by either limiting the offset-range during acquisition or by generating offset-range stacks.

As discussed in Chapter 1, the acquisition of multicomponent seismic data enables not only the recording of conventional P-wave data but also S-wave data. This S-wave data, in turn, can provide additional information concerning the geology of an area. This thesis showed that the interpretation of P-SV data can assist significantly in delineating geologic units, particularly the Cardium conglomerates of the Carrot Creek field.

The major conclusions from this thesis are:

- i) Radial (P-SV) data can be processed to produce a good-quality stack that can be directly correlated with vertical (P-P) component events.
- ii) At the location of conglomerate bodies the vertical component of the multicomponent data set exhibits only subtle amplitude variations, whereas at the same location strong amplitude anomalies can be observed on the radial (P-SV) component.
- iii) Differences in amplitude of the Cardium event between the P-P and P-SV final stacks is a result of the differences in their respective AVO responses. AVO forward modeling showed that a polarity reversal occurs with increasing offset for the P-P but not the P-SV case. It is this polarity reversal which causes the attenuation of the P-P Cardium event relative to the P-SV event. Upon stacking, the near- and far-offsets of the P-P data add destructively, whereas the radial-component offsets add constructively, producing a higher amplitude P-SV Cardium event.
- iv) Due to their respective AVO responses, the P-P and P-SV data are most sensitive

to the thickness of the conglomerate over different offset-ranges. The P-P data, for instance, exhibits the greatest sensitivity in the first 1000 m of offset (i.e. before the polarity reversal). The radial component, on the other hand, is most sensitive over the 500-2000 m offset range. The conventional seismic data having a far-offset of 1200 m, also acquired in the Carrot Creek area but in a different location than the multicomponent data, showed no indication of thick conglomerate deposits.

v) Using both P-P and P-SV data, estimates for Poisson's ratio for specific seismic intervals were calculated. Since the Cardium conglomerate possesses a low Poisson's ratio (0.18-0.22), relative to the surrounding shales (0.31), this interval analysis is believed to have identified variations in conglomerate thickness by the presence of lows in the calculated Poisson's ratio. Two such lows, identified on line CCSW01, correlate well with the location of known thick conglomerates.

vi) Better imaging of the Cardium conglomerate could be achieved by limiting the offset-range during acquisition or by generating offset-range stacks. Offset-range stacks produced the greatest improvement with the P-P data. For instance, by limiting the P-P data to the 0-1000 m offset-range the locations of thick Cardium conglomerate deposits could be identified (i.e. no destructive interference occurs as in the full-offset case). The P-SV data, on the other hand, should be limited to an offset range of 2000 m to best capitalize on the thickness sensitivity of these data.

In summary, the use of multicomponent seismic data appears to show much promise in hydrocarbon exploration. Not only does it give an independent estimate of the subsurface geologic structure, but also can give an indication of variations in lithologies.

**REFERENCES**

- AGAT Laboratories, 1987, Table of formations of Alberta, AGAT Laboratories, Calgary.
- Aki, K. and Richard, P.G., 1980, Quantitative Seismology: Theory and Methods, Volume 1: W.H. Freeman and Co..
- Baltenberger, P.A. and Bay, A.R., 1990, Case study: Defining the Morrow (Pennsylvanian) using multicomponent seismic data: 60th Ann. Internat. Mtg. Soc. Expl. Geophys.: Expanded Abstracts, 167-168.
- Bell, J.S. and Babcock, E.A., 1986, The stress regime of the Western Canadian Basin and implications for hydrocarbon production: Bulletin of Canadian Petroleum Geology, **34**, 364-378.
- Bergman, K.M. and Walker, F.G., 1987, The importance of sea-level fluctuations in the formation of linear conglomerate bodies: Carrot Creek Member of the Cardium Formation, Cretaceous Western Interior Seaway, Alberta, Canada: Journal of Sedimentary Petrology, **57**, 651-665.
- Chacko, S., 1989, Porosity identification using amplitude variations with offset: examples from South Samatra: Geophysics, **54**, 942-951.
- Claerbout, J.F. and Doherty, S.M., 1972, Downward continuation of moveout corrected seismograms: Geophysics, **37**, 741.
- Coulombe, C.A. and Stewart, R.R., Amplitude-versus-offset using the vertical seismic profile: CREWES Project Research Report, Volume 2, 464-476.
- Crampin, S., 1985, Evaluation of anisotropy by shear-wave splitting: Geophysics, **50**, 142-152.
- Crampin, S., Chesnokov, E.M. and Hipkin, R.A., 1984, Seismic anisotropy - the state of the art: Geophysical Journal of the Royal Astronomical Society, **76**, 1-16.

- Domenico, S.N., 1976, Effect of brine-gas mixture on velocity in an unconsolidated sand reservoir: *Geophysics*, **41**, 882-894.
- Domenico, S.N. and Danbom, S.H., 1986, Shear-wave technology in petroleum exploration- past, current, and future: in Danbom, S.H. and Domenico, S.N., Eds., *Shear-wave Exploration, Geophysical Development, No. 1, Society of Exploration Geophysicists*, 3-18.
- Eaton, D.W.S and Stewart, R.R., 1989, Aspects of seismic imaging using P-SV converted-waves: *The CREWES Project Research Report, Volume 1*, 68-92.
- Eaton, D.W.S., Slotboom, R.T., Stewart, R.R. and Lawton D.C., 1990, Depth-variant converted-wave stacking: *60th Ann. Internat. Mtg. Soc. Expl. Geophys., Expanded Abstracts*, 1107-1110.
- Eaton, D.W.S and Lawton, D.C., 1991, P-SV stacking charts and binning periodicity: *Geophysics*, in press.
- Edelmann, H.A.K., 1985, Shear-wave energy sources: in Dohr, G., Ed., *Seismic Shear Wave: Handbook of Geophysical Exploration, Volume 15a*, Geophysical Press.
- Ensley, R.A., 1984, Comparison of *P*- and *S*-wave seismic data: A new method for detecting gas reservoirs: *Geophysics*, **49**, 1420-1431.
- Frasier, C. and Winterstein, D., 1990, Analysis of conventional and converted mode reflections at Putah sink, California using three-component data: *Geophysics*, **55**, 646-659.
- Fromm, G., Krey, T. and Wiest, B., 1985, Static and dynamic corrections: in Dohr, G., Ed., *Seismic Shear Waves: Handbook of Geophysical Exploration, Volume 15a*, Geophysical Press, 191-225.
- Gregory, A.R., 1976, Fluid saturation effects on dynamic elastic properties of sedimentary rocks: *Geophysics*, **41**, 895-921.
- Harrison, M., 1989, Three-component seismic data processing: Carrot Creek Alberta:

CREWES Project Research Report, Volume 1, 6-26.

Harrison, M., 1991, Poststack migration of P-SV data: CREWES Project Research Report, Volume 3, 150-172.

Helbig, K., 1986, Shear-waves - what they are and how they can be used: in Danbom, S.H. and Domenico, S.N., Eds., Shear-wave Exploration, Geophysical Development, No. 1, Society of Exploration Geophysicists, 19-38.

Howell, C.E., Lawton, D.C., Krebs, E.S. and Thurston, J.B., 1991, P-SV and P-P synthetic stacks: CREWES Project Research Report, Volume 3, 191-204.

Iverson, W.P., Fahmy, B.A. and Smithson, S.B., 1989,  $V_pV_s$  from mode-converted P-SV reflections: *Geophysics*, **54**, 843-852.

Joiner, S., 1989, Sedimentology and ichnology of the Cardium Carrot Creek field, west central Alberta, Course work: Geology 701, The University of Calgary.

Keary, P. and Brooks, M., 1984, *An Introduction to Geophysical Exploration*: Blackwell Scientific Publications.

Koefoed, O., 1955, On the effect of Poisson's ratios of rock strata on the reflection coefficients of plane waves: *Geophysical Prospecting*, **3**, 381-387.

Koefoed, O., 1962, Reflection and transmission coefficients for plane longitudinal incident waves: *Geophysical Prospecting*, **10**, 304-351.

Krause, F.F. and Nelson, D.A., 1984, Storm event sedimentation: lithofacies formation in the Cardium Formation, Pembina area, west central Alberta, Canada: in Stoth, D.F. and Glass, D.J. Eds., *The Mesozoic of Middle North America*, C.S.P.G. Memoir 9, 485-511.

Krebs, E., 1988, *Geophysics 557*, course notes: The University of Calgary.

Lawton, D.C., 1990, A 9-component refraction seismic experiment: *Canadian Journal of Exploration Geophysics*, **26**, 7-16.

McCormack, M.D., Dunbar, J.A., and Sharp, W.W., 1984, A case history of stratigraphic

interpretation using shear and compressional seismic data: *Geophysics*, **49**, 509-520.

- McCormack, M.D. and Tatham, R.H., 1986, Shear-wave exploration seismology, course notes: SEG continuing education series.
- Muskat, M. and Meres, M.W., 1940, Reflection and transmission coefficients for plane waves in elastic media: *Geophysics*, **5**, 149-155.
- Newman, P., 1973, Divergence effects in a layered earth: *Geophysics*, **38**, 481-488.
- Ostrander, W.J., 1984, Plane-wave reflection coefficients for gas sands at non-normal angles of incidence: *Geophysics*, **49**, 1637-1648.
- Palmer, D., 1980, The generalised reciprocal method of seismic refraction interpretation: Society of Exploration Geophysicists.
- Pardus, Y.C., Conner, J., Schuler, N.R. and Tatham, R.H., 1990,  $V_p/V_s$  and lithology in carbonate rocks: a case study in the Scipio Trend in Southern Michigan: 60th Ann. Internat. Mtg. Soc. Expl. Geophys., Expanded Abstracts, 169-172.
- Pickett, G., 1963, Acoustic character logs and their application to formation evaluation: *Journal of Petroleum Technology*, **15**, 659-667.
- Plint, A.G., Walker, R.G. and Bergman, K., 1986, Cardium Formation 6: Stratigraphic framework of the Cardium in the subsurface: *Bulletin of Canadian Petroleum Geology*, **34**, 213-225.
- Robertson, J.D. and Pritchett, W.C., 1985, Direct hydrocarbon detection using comparative *P*-wave and *S*-wave seismic sections: *Geophysics*, **50**, 383-393.
- Rutherford, S.R. and Williams, R.H., 1989, Amplitude-versus-offset variations in gas-sands: *Geophysics*, **54**, 680-688.
- Sheriff, R.E., 1991, *Encyclopedic Dictionary of Exploration Geophysics*, third edition: Society of Exploration Geophysicists.
- Slotboom, R.T. and Lawton D.C., 1989, Depth-varient mapping and moveout correction of converted-wave data: The CREWES Project Research Report, Volume 1, 55-67.

- Slotboom, R.T., Eaton, D.W.S. and Lawton, D.C., 1990, Improving converted-wave (P-SV) moveout estimation: CREWES Project Research Report, Volume 2, 80-88.
- Tatham, R.H. and Stoffa, P.L., 1976,  $V_p/V_s$  - A potential hydrocarbon indicator: *Geophysics*, **41**, 837-849.
- Tatham, R.H., 1982,  $V_p/V_s$  and lithology: *Geophysics*, **47**, 336-344.
- Tessmer, G. and Behle, A., 1988, Common reflection point data-stacking technique for converted waves: *Geophysical Prospecting*, **36**, 671-688.
- Wang, Z., 1989, Carrot Creek core analysis: Core Laboratories, Calgary.
- Wiggins, R.A., Lerner, K.L. and Wisecup, R.D., 1976, Residual statics analysis as a general linear inverse problem: *Geophysics*, **41**, 922-938.
- Williams, G.D. and Burk, C.F. Jr., 1964, Upper Cretaceous: in McCrosson, R.G. and Glaister, R.P. Eds., *Geological History of Western Canada*, Calgary, Alberta Society of Petroleum Geologists, 169-189.
- Wren, E.A., 1984, Seismic techniques in Cardium exploration: *Journal of the Canadian Society of Exploration Geophysicists*, **20**, 55-59.
- Wyatt, K.D. and Wyatt, S.B., 1984, Determining subsurface structure using the vertical seismic profile: in Toksoz, M.N. and Stewart, R.R., Eds., *Vertical seismic profiling, part B: Advanced concepts: Handbook of Geophysical Exploration*, Volume 14b, Geophysical Press, 148-176.
- Yilmaz, O., 1987, *Seismic Data Processing*, Society of Exploration Geophysicists, pp. 69-70 and 429-453.

LINE	CR851				CR852				CR853			
	222		322		272		322		272		372	
CMP	Time (ms)	Velocity (m/s)										
	0	2050	0	2000	0	2000	0	1850	0	1900	0	1900
	150	2250	80	2100	130	2030	90	1860	75	2050	90	1910
	290	2480	210	2385	350	2525	270	2575	290	2380	210	2050
	390	2600	330	2610	530	2700	410	2685	390	2420	370	2510
	630	2900	450	2760	670	2925	610	2925	630	2520	510	2625
	890	3050	490	2795	890	2970	710	2925	730	2725	710	2820
	1050	3150	670	2950	1090	3005	810	2985	910	3020	910	2950
	1110	3190	810	3085	1170	3220	870	3030	1010	3035	1010	3030
	1190	3210	990	3260	1310	3355	990	3050	1190	3300	1190	3290
	1270	3300	1170	3310	1510	3430	1090	3130	1410	3375	1450	3390
	1430	3350	1210	3310	1590	3600	1170	3315	1770	3680	1770	3680
	1510	3400	1310	3320	1870	3790	1250	3350	3000	3706	3000	3700
	1810	3600	1570	3420	3000	3800	1530	3580				
	3000	3800	1810	3700			1810	3800				
			3000	3710			3000	3810				

Appendix A - Velocity function used in processing the conventional seismic data

LINE	CCSW01								CCSW02											
	Component		Vertical				Radial				Component		Vertical				Radial			
	CMP	222	372		272		422		222	422	222		322							
	Time (ms)	Velocity (m/s)																		
	0	2100	0	2250	0	1600	0	1700	0	2100	0	2200	0	1600	0	1750				
	150	2250	150	2210	200	2030	210	1860	190	2300	200	2350	220	1700	320	1790				
	290	2380	210	2300	450	2525	450	1950	320	2380	310	2390	440	1890	500	1966				
	390	2535	340	2480	560	2700	560	2010	490	2710	370	2510	510	1920	650	2080				
	640	2890	450	2690	800	2925	810	2260	630	2900	640	2880	690	2090	830	2265				
	910	2955	490	2720	1020	2970	1010	2270	890	3200	810	3120	890	2200	1010	2270				
	1060	3305	670	2900	1320	2005	1350	2380	1050	3300	910	3240	1050	2280	1370	2460				
	1150	3405	810	3200	1450	2220	1460	2450	1110	3390	1090	3380	1200	2350	1580	2555				
	1190	3390	990	3260	1700	2355	1730	2650	1210	3430	1200	3440	1350	2400	1730	2640				
	1300	3500	1160	3310	1910	2430	1890	2700	1270	3480	1310	3390	1470	2470	1880	2680				
	1440	3620	1210	3350	2060	2600	2060	2750	1430	3610	1450	3680	1810	2620	2060	2730				
	1510	3680	1310	3400	2340	2790	2320	2800	1710	3900	1530	3700	1960	2650	2330	2800				
	1810	3900	1570	3650	2540	2800	2530	2770	3000	4200	1800	3980	2430	2780	2540	2880				
	3000	4100	1820	3900	2900	2910	2920	2910			3000	4150	2970	2900	2850	2970				
			3000	4200	4000	3150	4000	3200					3250	3010	4000	3250				
													4000	3200						

Appendix B - Velocity function used in processing the multicomponent seismic data